

Gaia-ESO Survey: global properties of clusters Trumpler 14 and 16 in the Carina Nebula. [★]

F. Damiani¹, A. Klutsch², R. D. Jeffries³, S. Randich⁴, L. Prisinzano¹, J. Maíz Apellániz⁵, G. Micela¹, V. Kalari^{6,7}, A. Frasca², T. Zwitter⁸, R. Bonito^{1,9}, G. Gilmore¹⁰, E. Flaccomio¹, P. Francois¹¹, S. Kuposov^{10,12}, A. C. Lanzafame¹³, G. G. Sacco⁴, A. Bayo¹⁴, G. Carraro¹⁵, A. R. Casey¹⁰, E. J. Alfaro¹⁶, M. T. Costado¹⁶, P. Donati¹⁷, E. Franciosini⁴, A. Hourihane¹⁰, P. Jofré^{10,18}, C. Lardo¹⁹, J. Lewis¹⁰, L. Magrini⁴, L. Monaco²⁰, L. Morbidelli⁴, C. C. Worley¹⁰, J. Vink⁶, and S. Zaggia²¹

¹ INAF - Osservatorio Astronomico di Palermo G.S.Vaiana, Piazza del Parlamento 1, I-90134 Palermo, Italy
e-mail: damiani@astropa.inaf.it

² INAF - Osservatorio Astrofisico di Catania, via S. Sofia 78, 95123, Catania, Italy

³ Astrophysics Group, Keele University, Keele, Staffordshire ST5 5BG, United Kingdom

⁴ INAF - Osservatorio Astrofisico di Arcetri, Largo E. Fermi 5, 50125, Firenze, Italy

⁵ Centro de Astrobiología (CSIC-INTA), ESAC campus, Camino bajo del castillo s/n, 28 692 Villanueva de la Cañada, Madrid, Spain

⁶ Armagh Observatory, College Hill, Armagh BT61 9DG, UK

⁷ School of Mathematics & Physics, Queen's University Belfast, Belfast BT61 7NN, UK

⁸ Faculty of Mathematics and Physics, University of Ljubljana, Jadranska 19, 1000, Ljubljana, Slovenia

⁹ Dipartimento di Fisica e Chimica, Università di Palermo, Piazza del Parlamento 1, 90134, Palermo, Italy

¹⁰ Institute of Astronomy, University of Cambridge, Madingley Road, Cambridge CB3 0HA, UK

¹¹ GEPI, Observatoire de Paris, CNRS, Université Paris Diderot, 5 Place Jules Janssen, 92190 Meudon, France

¹² Moscow MV Lomonosov State University, Sternberg Astronomical Institute, Moscow 119992, Russia

¹³ Dipartimento di Fisica e Astronomia, Sezione Astrofisica, Università di Catania, via S. Sofia 78, 95123, Catania, Italy

¹⁴ Instituto de Física y Astronomía, Universidad de Valparaíso, Chile

¹⁵ European Southern Observatory, Alonso de Cordova 3107 Vitacura, Santiago de Chile, Chile

¹⁶ Instituto de Astrofísica de Andalucía-CSIC, Apdo. 3004, 18080, Granada, Spain

¹⁷ INAF - Osservatorio Astronomico di Bologna, via Ranzani 1, 40127, Bologna, Italy

¹⁸ Núcleo de Astronomía, Facultad de Ingeniería, Universidad Diego Portales, Av. Ejercito 441, Santiago, Chile

¹⁹ Astrophysics Research Institute, Liverpool John Moores University, 146 Brownlow Hill, Liverpool L3 5RF, United Kingdom

²⁰ Departamento de Ciencias Físicas, Universidad Andres Bello, Republica 220, Santiago, Chile

²¹ INAF - Osservatorio Astronomico di Padova, Vicolo dell'Osservatorio 5, I-35122, Padova, Italy

Received date / Accepted date

ABSTRACT

Aims. We present the first extensive spectroscopic study of the global population in star clusters Trumpler 16, Trumpler 14 and Collinder 232 in the Carina Nebula, using data from the Gaia-ESO Survey, down to solar-mass stars.

Methods. In addition to the standard homogeneous Survey data reduction, a special processing was applied here because of the bright nebulosity surrounding Carina stars.

Results. We find about four hundred good candidate members ranging from OB types down to slightly sub-solar masses. About one-hundred heavily-reddened early-type Carina members found here were previously unrecognized or poorly classified, including two candidate O stars and several candidate Herbig Ae/Be stars. Their large brightness makes them useful tracers of the obscured Carina population. The spectroscopically-derived temperatures for nearly 300 low-mass members allows the inference of individual extinction values, and the study of the relative placement of stars along the line of sight.

Conclusions. We find a complex spatial structure, with definite clustering of low-mass members around the most massive stars, and spatially-variable extinction. By combining the new data with existing X-ray data we obtain a more complete picture of the three-dimensional spatial structure of the Carina clusters, and of their connection to bright and dark nebulosity, and UV sources. The identification of tens of background giants enables us also to determine the total optical depth of the Carina nebula along many sight-lines. We are also able to put constraints on the star-formation history of the region, with Trumpler 14 stars found to be systematically younger than stars in other sub-clusters. We find a large percentage of fast-rotating stars among Carina solar-mass members, which provide new constraints on the rotational evolution of pre-main-sequence stars in this mass range.

Key words. Open clusters and associations: individual (Trumpler 14, Trumpler 16, Carina Nebula) – stars: pre-main-sequence

1. Introduction

The Carina Nebula is one of the most massive H_{II} regions known in the Galaxy. It contains a large population of massive OB stars

[★] Based on observations collected with the FLAMES spectrograph at VLT/UT2 telescope (Paranal Observatory, ESO, Chile), for the Gaia-ESO Large Public Survey (program 188.B-3002).

(the Car OB1 association), several Wolf-Rayet stars, and the well known LBV star η Carinae. Most of the stellar content of the Carina Nebula is found concentrated in a few clusters, notably Trumpler 16 (Tr 16, hosting η Car itself) and Trumpler 14 (Tr 14), about $10'$ NNW of η Car. Less conspicuous clusters associated with the Nebula include Trumpler 15, Collinder 228 and Collinder 232. The distance to η Car has been precisely determined to be 2.35 ± 0.05 kpc (Smith 2006). Car OB1 contains some of the most massive O stars known, including rare examples of O3, and even O2 stars. The properties of the region were reviewed by Smith and Brooks (2007, 2008). More recently, the whole Carina star-formation region (SFR) was thoroughly investigated by means of a mosaic of Chandra X-ray observations (CCCP: Chandra Carina Complex Project; Townsley et al. 2011, and all papers in the series), after earlier X-ray studies of the central clusters Trumpler 16 and 14 with both Chandra (Albacete-Colombo et al. 2008) and XMM-Newton (Antokhin et al. 2008). The X-ray data have been crucial to demonstrate the existence of a population (both clustered and diffuse) of ≥ 14000 stars, undoubtedly associated with the SFR, being most likely low-mass young stars formed in the Nebula several millions years ago. Detailed studies of the stellar population in Carina have been until now exclusively directed towards characterizing its rich massive-star members, while are still largely missing for its lower-mass population. For example, DeGioia-Eastwood et al. (2001) reported optical photometry for only ~ 850 stars in Trumpler 16 and 14. Only fairly recently deep optical photometry on more than 4500 stars in the same region was published by Hur et al. (2012), allowing optical counterparts of faint X-ray sources to be studied. Spectroscopic studies of the low-mass PMS stars in these clusters are almost entirely lacking; Vaidya et al. (2015) present low-resolution spectra of 11 PMS stars.

The study of low-mass PMS stars at the distance of Carina, and sometimes embedded within obscuring dust and/or bright nebular emission, is time-consuming and technically challenging. At the same time, it is important to test whether the early evolution of stars under such “extreme” ambient conditions, dominated by the presence of hundreds OB stars, do differ from that in “quieter” SFRs (e.g. Taurus-Auriga, or also Orion). Recent results from X-ray and IR surveys suggest that stars formed in rich clusters (e.g., Carina, Cygnus X, NGC3603, Westerlund 1 and 2) may be an important, if not dominant, component of all stars in the Galaxy, thus more representative of the “average Milky-Way star” than stars formed in less rich SFRs like e.g., Tau-Aur, Chamaleon, or IC348 (see e.g., Lada and Lada 2003). Therefore, the study of Carina stars across the whole mass spectrum is likely to be relevant for a better understanding of the general stellar population in the Galaxy.

It is not clear whether the various clusters in Carina are coeval, and if not, if this can be attributed to triggered or sequential star formation processes. Evidences for triggered formation in Carina have been discussed by Smith et al. (2010), but focusing on a different part of the nebula (the ‘southern pillars’) than that studied here, with some overlap only in the Tr 16 SE obscured region. In the central part of Carina studied here, evidence for recent or ongoing star formation is less frequent than in the southern parts (Povich et al. 2011b). Among the central Carina clusters, Tr 14 was suggested to be 1-2 Myr younger than Tr 16, because of its more compact structure and other characteristics (Walborn 1995, Smith 2006). It is however unclear if Tr 16 can still be considered as a single cluster with a rather sparse population, or rather as several physical clusters, as suggested by the X-ray results of Feigelson et al. (2011).

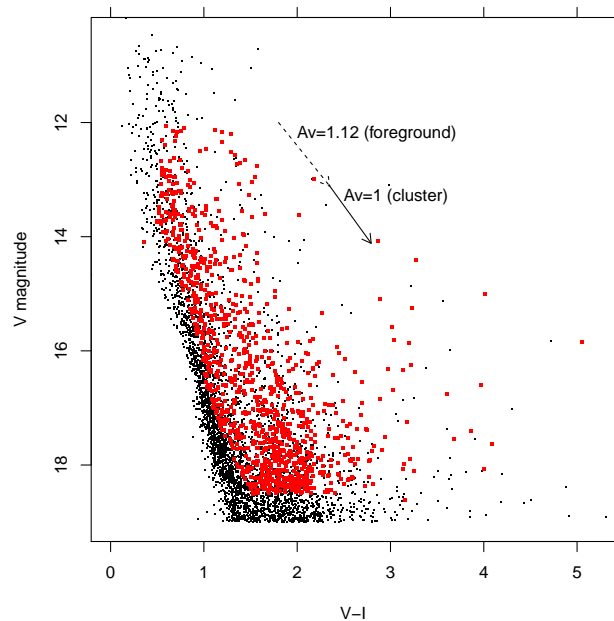


Fig. 1. $(V, V - I)$ diagram of all stars in the Hur et al. (2012) catalog. Big red dots indicate the spectroscopically observed stars studied here. The dashed arrow indicates the foreground reddening vector, while the solid arrow indicates a representative intra-cluster reddening vector corresponding to $A_V = 1$.

In order to complement the studies of massive stars in Carina, and obtain a more complete understanding of the star formation processes which have taken place in its recent past, we present here the first spectroscopic study of a sizable population of hundreds lower-mass stars (down to approximately one solar mass), using data from the Gaia-ESO Survey (Gilmore et al. 2012, Randich et al. 2013). The same observational dataset was used in a previous work (Damiani et al. 2016, Paper I) to study the dynamics of the ionized gas in the Carina H_{II} region from optical nebular emission lines.

This paper is structured as follows: in Section 2 we describe the composition of the observed sample; Section 3 discusses cluster membership for the observed stars; Section 4 discusses massive stars which happen to fall within our sample; Section 5 discusses the spatial clustering of stars; Section 6 is devoted to a discussion of reddening; Section 7 presents Color-magnitude diagrams; Section 8 compares results from the present data with those from X-ray data; Section 9 discusses the structure of the whole region; Section 10 discusses stellar ages, and Section 11 the rotational properties of Carina stars. Eventually, we summarize our results in Section 12.

2. Observations and data analysis

2.1. The observed sample

In this work we study a set of spectra of 1085 distinct stars in the Carina Nebula, obtained with the FLAMES/Giraffe multi-fibre spectrometer at the ESO VLT/UT2 telescope on April 6-9, 2014, and released as part of the iDR4 Gaia-ESO data release. The total number of individual spectra was 1465, but all spectra relative to the same star were coadded to improve signal-to-noise ratio (SNR). Simultaneously, spectra with the FLAMES/UVES high-resolution spectrograph were obtained, which will be presented separately (Spina et al. in prep.). All spectra considered here are

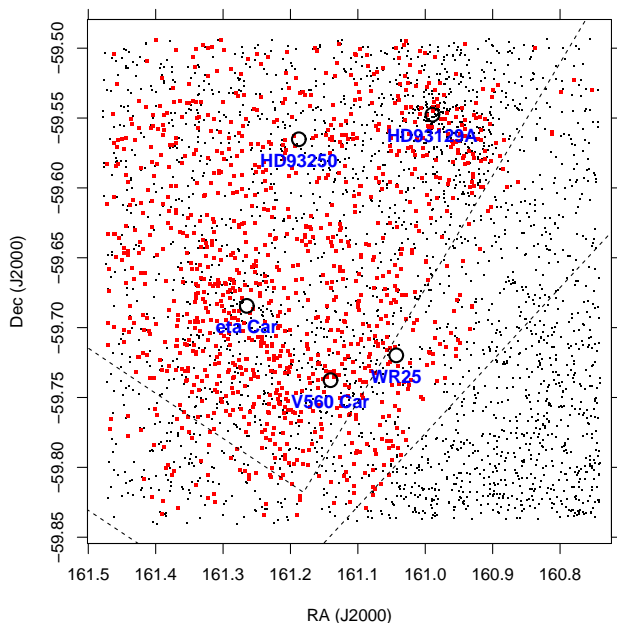


Fig. 2. Spatial distribution of Hur et al. (2012) stars brighter than $V = 18.5$, and of observed stars (red). The most massive stars in the region are indicated with big circles and names. The dashed lines indicate the approximate positions of the dark obscuring dust lanes bounding Tr 14 and 16.

taken using Giraffe setup HR15n ($R \sim 17000$, wavelength range 6444–6818Å), as in all Gaia-ESO observations of cool stars in open clusters; the (known) OB stars in Carina are instead being observed using different Giraffe setups, to obtain a more comprehensive set of diagnostics, better suited to hot stars (the massive star spectra are not part of the current data release and will be studied in a later work). As a consequence, we will be able to give only a rough classification for the early-type stars which happen to fall within the sample studied here. The approach for deriving stellar parameters for later spectral types was instead described in Damiani et al. (2014) and Lanzafame et al. (2015).

The basis for our FLAMES target selection was the optical photometry published by Hur et al. (2012). This study covered a field, approximately $25' \times 25'$ in size, comprising only the central portions of the entire Nebula, and thus limited to the large clusters Tr 16 and 14, and the less rich Collinder 232. Moreover, we have not observed with the HR15n setup stars brighter than $V = 12$ (massive stars, observed with different Giraffe setups), nor fainter than $V = 18.5$, in order to obtain an acceptable minimum SNR. Since low-mass stars in the Carina SFR have not yet arrived on the Zero-Age Main Sequence (ZAMS), we also excluded stars in that region of the color-magnitude diagram (CMD); also a spatial region near the edge of the photometric field-of-view, apparently dominated by field stars, was not observed; finally, random sampling of the remaining stars was made to avoid an exceedingly long target list. This procedure follows the general strategy for target selection in the Gaia-ESO Survey described in Bragaglia et al. (in preparation). The CMD of both the Hur et al. (2012) input catalog and our spectroscopically observed stars is shown in Fig. 1. Fig. 2 shows instead the spatial distribution of input and observed stars. The median SNR of our 1085 spectra is 36.2.

2.2. Data analysis

The Gaia-ESO Survey data analysis process is distributed among several Working Groups, whose task is to apply homogeneous procedures to all datasets to ensure a high degree of internal coherence. As explained in Paper I, however, the Carina Nebula presents a number of unanticipated features, which are not dealt with accurately using standard procedures/pipelines, like the spatially nonuniform sky continuum level due to reflection nebulosity and the wide $H\alpha$ wings due to both high-velocity ionized gas and reflection in the Nebula. This required to take a step back and redo part of the analysis, especially regarding a more appropriate subtraction of the sky spectrum, as described in the following. All derived parameters used here are released in the internal *GESiDR4* data release, database table *AstroAnalysis*. This reports the detailed results from each analysis “node”, and their merged values produced by the relevant Working Group (WG12 in our case); because of the mentioned difficulties, results obtained from individual nodes sometimes using non-standard, ad-hoc procedures were preferred to WG12 results in the case of stellar parameters (from node “OAPA”) and of lithium equivalent widths (EW; node “OACT”), while radial and rotational velocities were taken as those produced by WG12 (or node “OAPA” when these latter were missing).

The details of the special background-subtraction procedure employed by the OAPA node before evaluating stellar parameters are given in Appendix A. In short, after having separately corrected all atmospheric sky features, nebular lines are corrected using each of the nearest five sky spectra: the range of corrections obtained is an estimate of the uncertainty involved in the procedure, while the median of the five corrected spectra is taken as the best estimate stellar spectrum, for stellar parameter derivation. Lithium EWs were computed by different nodes, with results in good mutual agreement, using slightly different methods as explained in Lanzafame et al. (2015); the EW set from the OACT node was chosen because of its largest sample coverage. The WG12 radial and rotational velocities include contributions from both the OACT node, using methods detailed in Frasca et al. (2015), and OAPA node, using cross-correlation as briefly described in Damiani et al. (2014); a very good agreement is found for stars in common.

With the collection of five-fold nebular-subtracted stellar spectra obtained as explained in Appendix A, we proceeded with our estimates of stellar parameters (done five times per star), using the method explained in Damiani et al. (2014). This latter was purposely developed to deal with the spectral range and resolution of Giraffe HR15n data, and defines a set of spectral indices and their calibration to derive T_{eff} , $\log g$, and $[Fe/H]$ for stars later than $\sim A2$. The range spanned by each parameter in its own set of five determinations corresponds to the systematic error introduced by sky correction, often larger than the statistical error. Depending on the intensity ratio between the nebular $H\alpha$ wings and the stellar $H\alpha$ wings, these latter may in some cases be exceedingly affected by nebular emission, and cannot be used as a temperature diagnostic, e.g. in A to mid-G stars¹. For mid-A to lower-mass stars, fortunately, other indicators may be used to estimate temperatures (although the increased dependence on metallicity must be treated with caution). The problem is worst for early-A stars, where almost the only spectral line in HR15n range is $H\alpha$. Much weaker lines are found in the blue extreme of the HR15n range, where grating efficiency is however very low, and are therefore difficult to use in low-SNR spectra. In

¹ The most important features of stellar spectra in the HR15N wavelength range are described in Damiani et al. (2014).

practice, many faint early-A stars are recognized in the Tr 14/16 dataset as those having a nearly flat, featureless continuum spectrum, with indefinite properties in the $H\alpha$ region because of the predominant nebular emission. B-type stars are instead easily recognized because of their He I 6678Å line: the He I nebular line at the same wavelength has usually no wings (Paper I), and is much narrower than the stellar line, often broadened by fast rotation.

The wide nebular $H\alpha$ wings are also of great nuisance when trying to selecting stars with intrinsic wide $H\alpha$ emission because of accretion from a circumstellar disk (e.g. Classical T Tauri stars - CTTS - or Herbig Ae/Be stars - HAeBe). Here again, the five-fold nebular-subtracted star spectra are of invaluable help in separating cases where the apparent wide emission in the net spectrum arises from poorly subtracted nebular $H\alpha$ wings (as it will not be present in all five net spectra) from truly wide $H\alpha$ lines of CTTS/HAeBe stars.

2.3. Auxiliary data sets

The stellar population of the Carina nebula was the object of several recent studies. We have therefore cross-matched our spectroscopic targets with objects in several existing catalogues. A match with the CCCP X-ray source catalog (Broos et al. 2011a) yielded 352 matches among our 1085 sample stars. The match was made assuming a constant 1σ error on optical positions of 0.2 arcsec, individual catalogued X-ray position errors, and a 4σ maximum distance. The number of spurious matches was estimated as 13, by artificially shifting one of the two position lists by ± 1 arcmin. Then we considered the VPHAS+ DR2 Point Source Catalogue (Drew et al. 2014) with photometry in the bands *ugri* and $H\alpha$. Using a maximum matching distance of 5σ , and constant position errors of 0.2 arcsec for both optical and VPHAS+ catalogues, we obtain 1074 matches (of which ~ 140 estimated as spurious). However, the number of stars with a *clean=yes* photometric flag in all of *r*, *i*, and $H\alpha$ bands, matching our target list, is of only 171. Last, we matched similarly our targets to the Young Stellar Object (YSO) catalogue of Zeidler et al. (2016), obtained from both VISTA and Spitzer near/mid-IR data. The number of matches is 64 (~ 1 spurious), of which however only 7 have catalogued magnitudes in all four Spitzer IRAC bands ($3.6 - 8.0\mu$). All of these latter were already members by spectroscopic criteria, see below.

3. Cluster membership

Since the chosen sample-selection strategy for Gaia-ESO Giraffe observations is inclusive of most possible members, membership of observed stars to each cluster must be determined post-facto. The emphasis here being on young, low-mass stars (FGK stars), the most useful membership indicators are the lithium line EW and strong X-ray emission, in addition to radial velocity (RV) as usual. Wide $H\alpha$ emission wings, indicative of circumstellar accretion in pre-main-sequence (PMS) stars, is a strong evidence of extreme youth and probable membership to a SFR, even in the absence of a RV measurement (e.g., in cases of strong-emission stars without observable photospheric absorption lines). As described above, a star must show wide $H\alpha$ emission consistently across the multiple (five) sky-subtraction options, in order to be considered a reliable CTTS/HAeBe. This conservative approach undoubtedly misses some real emission-line members, but is a minor issue for building a reliable member list, since the other membership criteria may compensate for this. Narrow, chromo-

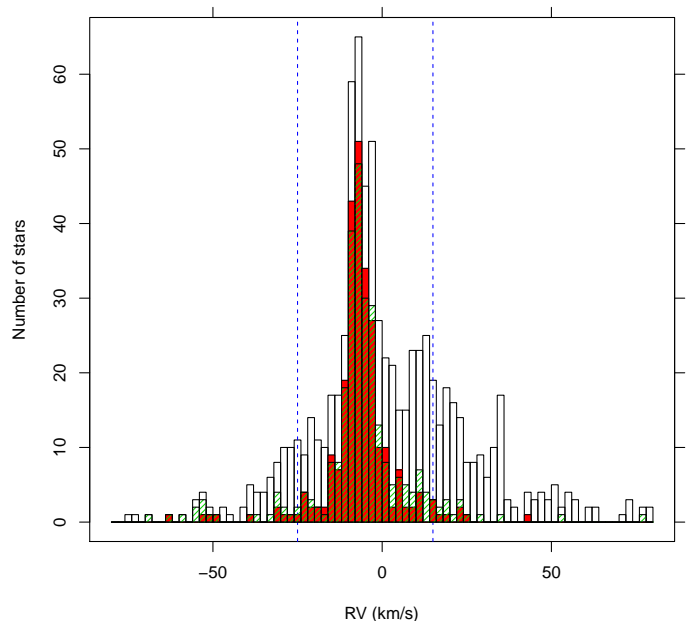


Fig. 3. Histogram of (heliocentric) RV for all stars with $T_{eff} < 8800$ K and $SNR > 15$ (white-colored bars). The red filled histogram represents stars with lithium $EW > 150$ mÅ; the dashed green histogram are stars detected in X-rays. The vertical dashed blue lines at $RV = (-25, +15)$ indicate our fiducial limits for RV membership.

spheric $H\alpha$ emission cannot be used here as a youth indicator, being swamped by the nebular emission lines whatever the sky-subtraction option chosen. In order to minimize the number of spurious members, a star is generally accepted as member only when it satisfies at least two criteria among: $|RV - RV_0| < \Delta RV$ (with RV_0 and ΔRV to be determined), lithium $EW > 150$ mÅ, X-ray detection, and CTTS/HAeBe status. However, since each of these criteria may include significant numbers of contaminants (e.g., G stars up to an age of about 1 Gyr would fall above our lithium EW threshold), some additional screening was applied, as described below.

To help determining RV_0 and ΔRV , Figure 3 shows a histogram of RV for stars with $T_{eff} < 8800$ K (and $SNR > 15$). Colored histograms refer to lithium- and X-ray-selected candidates: they select essentially the same population of low-mass Carina members. From this Figure, we find that good values for RV_0 and ΔRV are respectively -5 and 20 km/s, the latter being chosen to be rather inclusive since additional indicators are also used for final membership assessment². According to the above stated general rule, inside the dashed RV limits only one membership criterion (the RV criterion being fulfilled) is sufficient to consider a star as a member; outside of them, at least two indicators are needed. The number of stars shown in the total histogram is 755; scaled to this number, we expect 9 spurious optical-X-ray matches to be included in these histograms, distributed uniformly *per star* (not *per RV interval*): therefore, most of the spurious X-ray matches will lie inside the dashed lines, where most stars are found. This justifies in part the several bins containing X-ray detections in excess of lithium-rich stars. For the same reason, we expect 6-7 contaminants among candidate members found only from RV and X-ray criteria.

² The value of mean radial velocity RV_0 is in good agreement with that of the local molecular gas, see e.g. Rebollo et al. (2016, their Fig.5), with heliocentric $RV_0 = -5$ km/s corresponding to $V_{LSR} = -13.8$ km/s.

A handful of stars satisfying the “general” membership criteria above are found in the CMD very near the ZAMS at the cluster distance (or anyway at apparent ages > 20 Myr according to Siess et al. 2000 isochrones), even after accounting for reddening as in the following sections. Upon individual examination, only two³ of these 17 stars showed strong enough indications of membership to be retained in our list, while the others, mostly low-SNR spectra with poorly constrained parameters, were removed. Of these latter, six were simultaneously RV- and X-ray members, in very good agreement with their expected number.

Among our targets, additional candidate CTTS members were searched, but none found, using other catalogues: the VPHAS+ data, in particular using the $(r - i, r - H\alpha)$ diagram locus as in Kalari et al. (2015); the 2MASS data; and finally the Spitzer data from Broos et al. (2011a; table 6), considering disk-bearing stars with colors $[3.6 - 4.5] > 0.2$ and $[5.8 - 8.0] > 0.2$. To this stage, the number of low-mass candidate Carina members (colder than ~ 8000 K) found is 303, of which approximately 150 candidate CTTS.

We find also many stars with T_{eff} above 6500 K, which already at this young age have no traces of lithium, and are sometimes rotating so fast that an accurate derivation of RV might not be possible. Moreover, it is known that A-type stars are not strong coronal X-ray emitters (e.g., Schmitt 1997), so that our member list is least reliable for stars earlier than type F (approximately $T_{eff} \geq 7000$ K). Early-A and B-type stars, of which we find several tens, are instead rare in the field, so that most of them can be safely considered as Carina members (adding to the 303 low-mass candidates), even though their RVs might sometimes not be accurately determined because of fast rotation.

3.1. A young field-star population

A more detailed examination of candidate members is done from their cumulative RV distribution, as shown in Figure 4. The black curve is the RV cumulative distribution for all single member stars with $T_{eff} < 7000$ K, $v \sin i < 50$ km/s, and $SNR > 15$ (177 stars). A cumulative Gaussian distribution fitted to the median RV range between $(-20, 40)$ km/s is shown with the green curve (maximum-likelihood parameters $\langle RV \rangle = -5.9$ km/s, $\sigma(RV) = 4.66$ km/s). However, an obvious asymmetry is present between the two tails of the Gaussian distribution, with an excess of stars at $RV > 0$ km/s. Unrecognized binaries are only expected to produce symmetric tails. We inspected all spectra of stars with $RV > 0$ to check that no RV determination errors were present, to a level which might justify the observed discrepancy. The red curve shows therefore the cumulative distribution corresponding to two superimposed Gaussians, with maximum-likelihood parameters: $\langle RV_1 \rangle = -7.07$ km/s, $\sigma(RV)_1 = 3.48$ km/s; and $\langle RV_2 \rangle = 7.81$ km/s, $\sigma(RV)_2 = 6.37$ km/s. The main Gaussian distribution accounts for 77% of stars in the subsample considered here. The still mis-fit tail at $RV \sim -20$ km/s may be attributed to either binaries or an additional small population, of 6-7 stars, which was not examined further. The ~ 40 stars in the positive-velocity Gaussian are too many to be explained by spurious X-ray matches, whose number was quantified above: therefore, they are likely genuine X-ray bright and/or lithium rich stars, or young stars in general. Their discrepant RV distribution with respect to the main Carina population does not entitle us to consider them as Carina members. Based on their

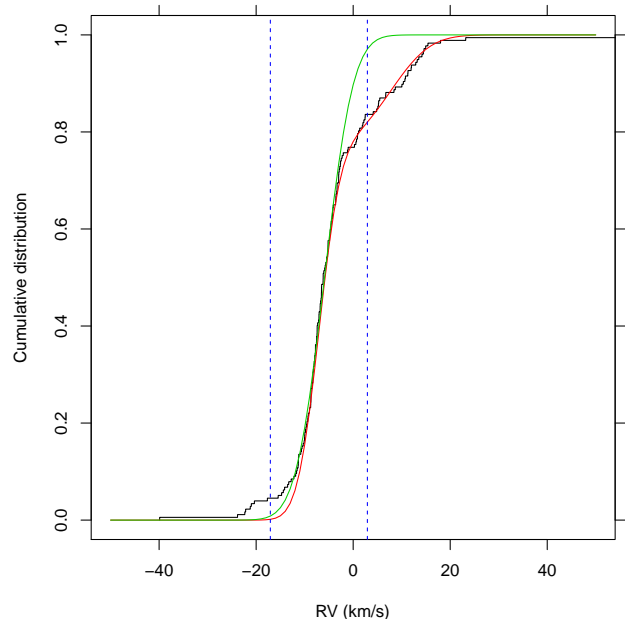


Fig. 4. Cumulative RV distribution for late-type members with $T_{eff} < 7000$ K and $v \sin i < 50$ km/s (solid line). Green: cumulative single-Gaussian distribution; red: two-Gaussian distribution. The blue vertical dashed lines indicate ± 7 km/s from median RV, as a reference.

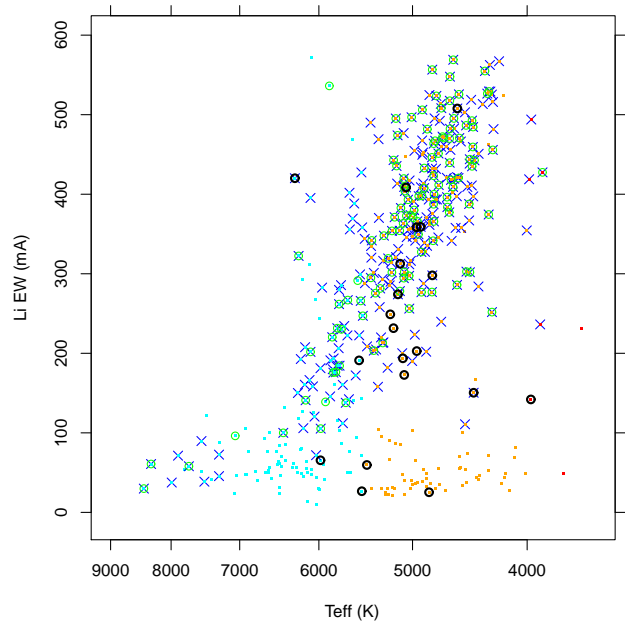


Fig. 5. Diagram of lithium EW vs. T_{eff} . Color-coding of small dots corresponds roughly to: solar-mass and earlier-type stars (cyan), late-G to mid-K stars (orange), and M-type stars (red). Probable members are indicated with blue crosses. Green circles indicate (CTTS or Herbig Ae/Be) stars with wide $H\alpha$ emission. The bigger black circles indicate RV10 stars.

approximate RV we will refer to these stars as “RV10 stars”. There are 29 RV10 stars with $RV > 3$ km/s, $T_{eff} < 7000$ K, $v \sin i < 50$ km/s, and $SNR > 15$.

We investigate the nature of the RV10 group by means of the T_{eff} -lithium EW diagram (Figure 5): the RV10 stars account for most of the low-lithium candidate members; however, more

³ These are the candidate HAeBe star [HSB2012] 2504, and the star [HSB2012] 2692, showing strong lithium, IR excess in the 2MASS bands, and association with a YSO.

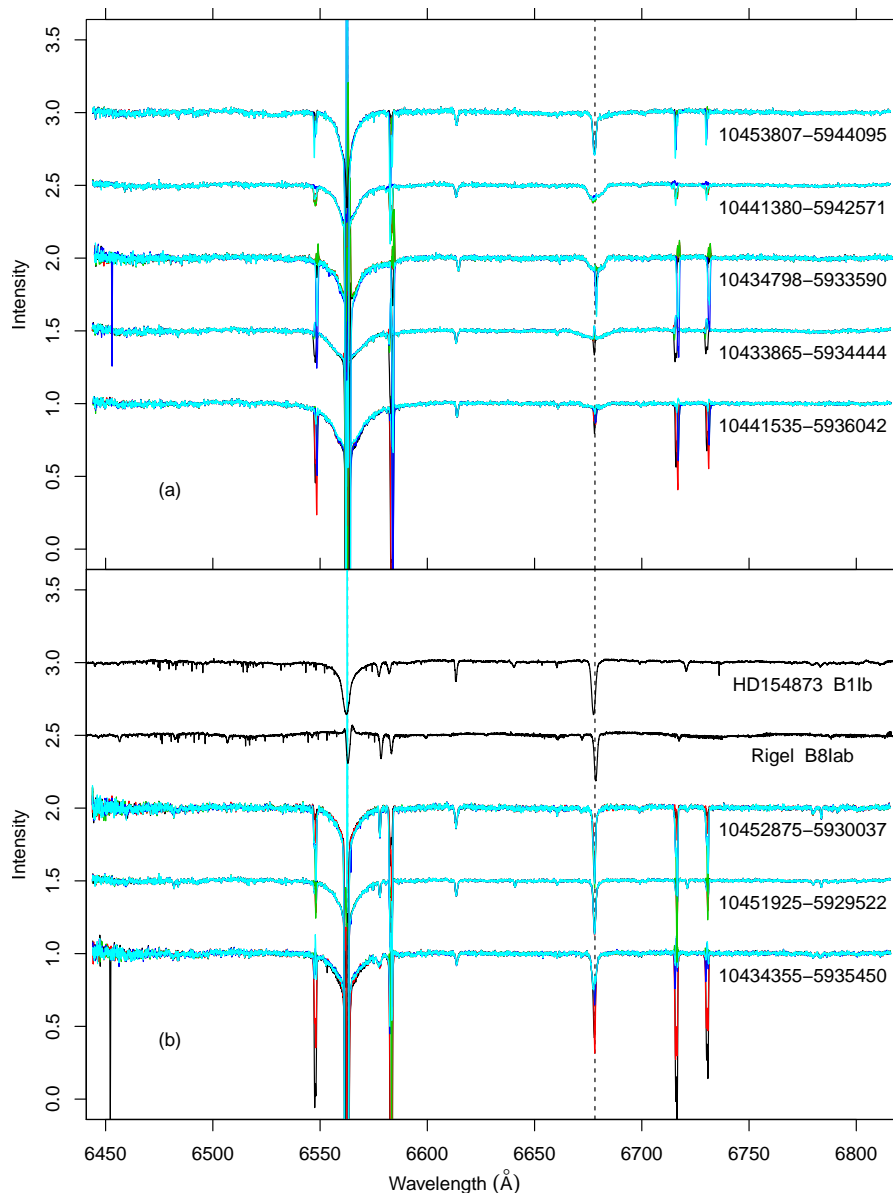


Fig. 6. (a), top: Example spectra of B stars found among our targets. For each star, five spectra are overplotted with different colors, corresponding to five distinct options regarding nebular subtraction. The vertical dashed black line indicates the He I 6678Å line, distinctive of B stars, but also coincident with a strong, narrow nebular line. Spectra of different stars are offset by 0.5 for clarity. The narrow absorption feature near 6613Å is a well-known DIB, while a weaker one is sometimes visible near 6660Å. (b), bottom: Spectra of sample B stars (lower three spectra) showing absorption in the C II doublet near 6580Å (the redder line in the doublet coincides with the nebular [N II] 6584Å line), which is typical of known B bright giants/supergiants (upper two spectra, from UVES/POP). The vertical dashed lines indicate H α and He I 6678Å.

than one-half of the RV10 stars have Li EW > 150 mÅ, and follow the same relation with T_{eff} as Carina members, to which are apparently coeval. All RV10 stars with Li EW > 250 mÅ have extinction (as determined in Section 6) higher than the foreground A_V^{fg} towards Carina (Hur et al. 2012). Nearly one-half of the RV10 stars have instead low extinction, suggesting that they are foreground stars; at the same time, many of these latter stars have significant Li EWs, indicating they are young stars (say < 100 Myr), in agreement with their frequent X-ray detection (18/29 stars). The spatial distribution of RV10 stars does not show clustering, and their location on the optical CMD often does not overlap the main cluster locus. We conclude that the RV10 are dominated by a group of (17) foreground young stars, unrelated to the Carina cluster, probably spanning a significant age range, and characterized by a common dynamics. Also their $v \sin i$ distribution is typical of young low-mass stars. We therefore speculate that they are a remnant from a now dissolved cluster, closer to us than the Carina nebula, in the same sky direction.

The 12 RV10 stars with $A_V > A_V^{fg}$ are instead probable Carina low-mass members, whose net number becomes 286.

Among them we find 8 SB2 binaries: this appears as a low percentage compared to other studies (e.g. Mathieu 1994); however, fast rotation, frequently found among Carina members (see Section 11) may render double-lined systems more difficult to detect, so we cannot draw firm conclusions on this subject for Carina stars. We do not consider these SB2 stars in the rest of the paper. The identifications and properties of Carina members are listed in Tables 1 and 2, while those of the RV10 group are in Tables 3 and 4.

Three stars with strong lithium lines but showing no other membership indicator turned out to be non-member lithium-rich giants, upon a detailed examination of their stellar parameters. Their identifications and properties are reported in Tables 5 and 6.

4. Massive stars

Our observed sample selection was made with the aim of studying low-mass stars in Carina, starting from A-type stars. However, a number of earlier-type stars are serendipitously found among the spectra studied here. Those O-type and B-type stars

Table 3. Identifications of RV10 stars. Columns as in Table 1.

HSB2012	CXOGNC	ADM2008	YSO	RA (J2000)	Dec (J2000)	<i>V</i>	<i>B</i> − <i>V</i>	<i>V</i> − <i>I</i>
394	104314.98-593341.3	10:43:14.99	-59:33:41.3	14.67	0.94	1.09
1262	104348.74-593430.4	10:43:48.59	-59:34:31.2	17.72	1.76	2.03
1788	104405.37-593043.5	10:44:05.42	-59:30:43.5	14.53	0.90	1.03
2169	10:44:18.67	-59:48:05.4	16.09	0.96	1.02
2270	10:44:22.78	-59:38:52.5	18.44	...	1.75
2296	104423.64-593941.8	146	...	10:44:23.56	-59:39:41.4	16.34	0.91	1.34
2561	10:44:32.97	-59:38:05.9	17.38	0.94	1.22
2797	10:44:42.77	-59:38:01.4	17.03	1.14	1.14
2959	104450.11-593429.3	10:44:49.99	-59:34:29.5	16.75	1.32	1.72
3030	104452.43-594130.1	469	...	10:44:52.40	-59:41:30.1	16.66	0.94	1.15
3167	104457.05-593826.5	534	...	10:44:57.06	-59:38:26.9	13.70	1.01	1.19
3229	10:44:58.90	-59:40:08.4	15.66	1.18	1.27
3290	104501.02-594515.5	600	...	10:45:01.03	-59:45:15.6	14.54	0.91	1.06
3688	10:45:15.44	-59:35:21.4	17.29	1.48	1.81
3844	104521.23-593258.2	10:45:21.20	-59:32:58.4	18.06	1.26	1.63
3926	104524.13-593131.1	10:45:24.14	-59:31:31.6	14.20	0.63	0.71
4310	104541.60-593820.2	1014	...	10:45:41.60	-59:38:20.2	14.46	0.87	1.00

Table 4. Parameters of RV10 stars. Columns as in Table 2.

HSB2012	SNR	RV (km/s)	<i>v</i> sin <i>i</i> (km/s)	<i>T</i> _{eff} (K)	<i>A</i> _{<i>V</i>}	Li EW (mÅ)	γ	log age (yr)	H α	SB2
394	31.1	10.3±1.1	24.0± 0.5	5189±105	0.39	231.6±7.2	0.984±0.009	...	N	N
1262	30.6	13.2±1.6	10.9± 2.5	3830± 17	0.42	...± ...	0.862±0.008	...	Y	N
1788	84.4	23.2±0.4	12.0± 0.5	5082± 38	0.20	172.8±3.1	0.984±0.003	...	N	N
2169	40.1	14.2±0.6	13.9± 1.6	5095± 76	0.19	193.7±5.2	0.985±0.007	...	N	N
2270	17.4	4.8±2.5	17.9±10.0	3816± 25	0.00	...± ...	0.847±0.015	...	Y	N
2296	59.0	15.4±2.2	18.7± 1.5	5548± 66	1.10	191.1±5.3	1.012±0.004	...	N	N
2561	31.7	14.6±0.9	12.0± 0.5	4731± 73	0.21	...± ...	0.974±0.008	...	Y	N
2797	42.1	14.9±1.1	12.3± 2.4	5115± 69	0.45	...± ...	0.988±0.006	...	Y	N
2959	41.4	92.5±2.7	27.0± 0.5	4295± 40	0.64	...± ...	0.984±0.006	...	Y	N
3030	42.5	10.8±1.3	24.0± 2.7	5465± 84	0.67	59.6±5.4	1.001±0.006	...	N	N
3167	112.9	10.7±0.7	15.0± 0.5	4842± 26	0.29	25.3±1.6	0.992±0.002	...	N	N
3229	68.3	4.1±0.7	12.0± 0.5	5519± 50	0.94	26.6±2.7	0.994±0.004	...	Y	N
3290	65.5	8.7±2.0	45.0± 0.5	4959± 44	0.16	202.8±4.4	0.98±0.004	...	N	N
3688	30.9	11.3±1.2	10.4± 1.7	4124± 41	0.51	...± ...	0.85±0.008	...	Y	N
3844	16.7	6.7±1.4	12.0± 0.5	3971± 54	0.00	142.0±9.3	0.92±0.016	...	Y	N
3926	28.6	8.4±1.0	9.6± 2.6	5981±137	0.00	65.5±6.1	0.978±0.009	...	N	N
4310	59.3	10.0±1.0	21.0± 0.5	5221± 56	0.22	249.0±4.0	0.986±0.004	...	N	N

Table 5. Identifications of lithium-rich field giants. Columns as in Table 1.

HSB2012	CXOGNC	ADM2008	YSO	RA (J2000)	Dec (J2000)	<i>V</i>	<i>B</i> − <i>V</i>	<i>V</i> − <i>I</i>
3579	10:45:11.09	-59:40:07.8	15.85	1.96	5.05
2595	10:44:34.42	-59:42:57.8	15.87	2.49	3.20
3504	10:45:08.53	-59:43:30.2	18.10	...	3.25

are intrinsically more luminous than the rest of the sample, but some were included here because of their higher extinctions or, in some cases, because they are located at significantly longer distances (the Carina Nebula is close to the tangent of a spiral arm). Although HR15n spectra are not ideal for a detailed classification of hot stars, we attempt here to assign a qualitative classification of these stars, whose importance in the study of the Carina SFR cannot be neglected. The spectroscopic information is complemented with a study using archival photometry.

4.1. Spectroscopic analysis

As mentioned in Sect. 2, the HR15n wavelength range contains the He I 6678.15Å line, which is a very useful diagnostics to select B-type stars. Of course, care must be used since at nearly the same wavelength a Fe I line is found in cooler stars, so that establishing a B-type spectrum also requires absence of metallic lines, and especially the group of lines between 6490-6500Å (Damiani et al. 2014), strong enough to remain recognizable even in fast rotators. As explained in Sect. 2 above (and see Paper I for details), H α and He I lines, which are the most intense lines in

Table 6. Parameters of lithium-rich field giants. Columns as in Table 2.

HSB2012	SNR	RV (km/s)	$v \sin i$ (km/s)	T_{eff} (K)	A_V	Li EW (mÅ)	γ	log age (yr)	H α	SB2
3579	133.3	22.1 \pm 2.3	24.7 \pm 4.6	2819 \pm 24	...	487.5 \pm 2.1	1.019 \pm 0.002	...	N	N
2595	96.9	17.7 \pm 1.4	18.9 \pm 1.6	3598 \pm 150	2.20	231.3 \pm 2.1	1.061 \pm 0.003	...	N	N
3504	32.0	43.1 \pm 0.7	7.5 \pm 1.7	4424 \pm 69	4.24	167.5 \pm 5.9	1.051 \pm 0.008	...	N	N

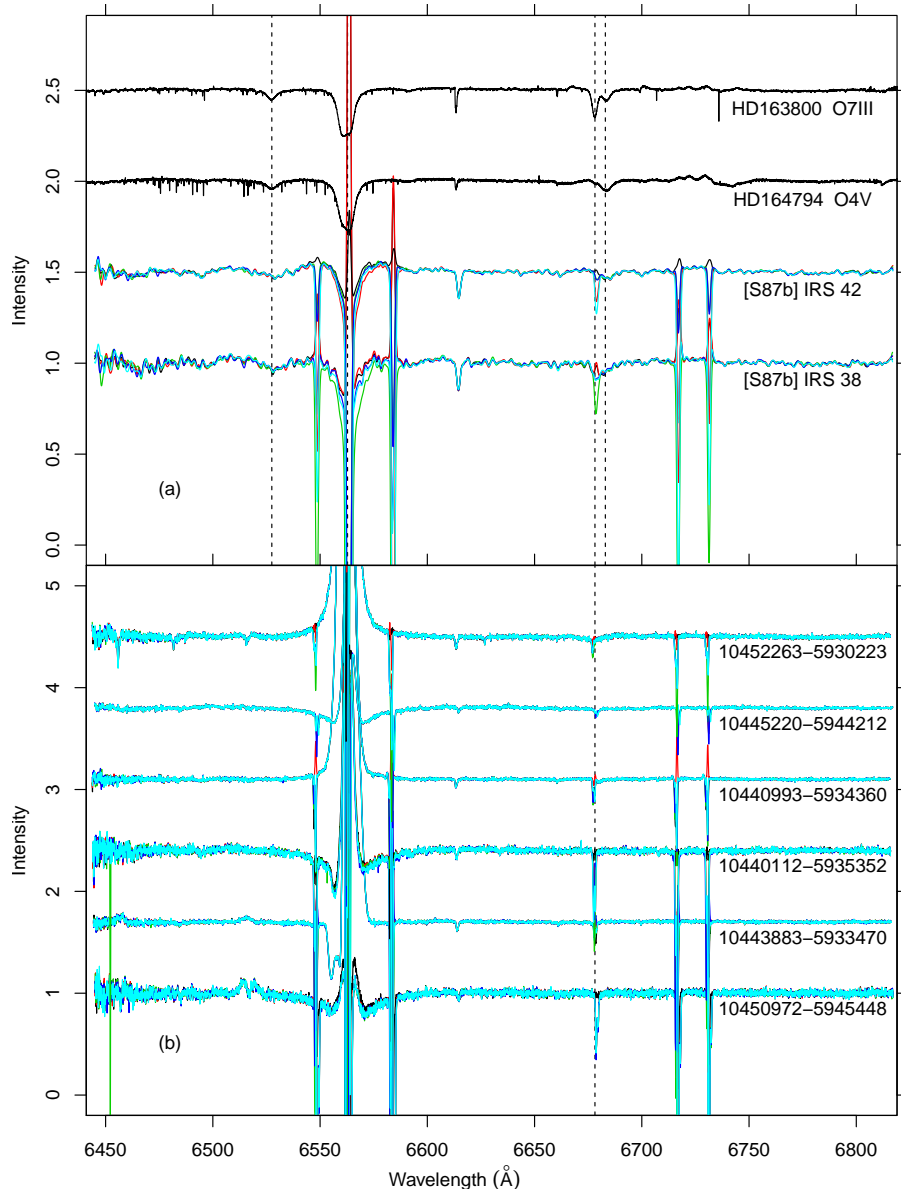


Fig. 7. (a), top: Spectra of a possible O star (SIMBAD identifier [S87b] IRS 38), a probable O star ([S87b] IRS 42), and two UVES/POP spectra of known O stars. The lower two spectra were slightly smoothed to improve their visibility. Dashed vertical lines indicate H α and He I 6678Å, as above, plus the He II lines at 6527 and 6684Å, typical of O stars. (b), bottom: Example spectra of new candidate Herbig Ae/Be stars discovered in this work. Note the consistently wide H α emission, regardless of the option chosen for nebular subtraction (color of plotted spectrum). Some of the stars show also absorption/emission in the Fe II lines at 6456.38, 6516.08Å.

the HR15n range for late-B stars, and the only detectable at low SNR, are both coincident with nebular sky lines, whose contribution is often impossible to subtract accurately. Therefore, classification of late-B stars on the basis of the present data may only be approximate. In practice it is often impossible to confirm or exclude the presence of a weak He I line in the spectrum of a fast-rotating star without metallic lines, to discriminate between a late-B and an early-A type, and therefore we will assign to these stars a generic "late-B/early-A" type. In tens of other cases, He I is safely detected, but again nebular lines make the determination of the stellar He I EW unreliable: these stars were thus classified as "B-type" without better detail. Examples of B-type stars in our dataset are shown in Fig. 6-a. In this Figure,

differences in the adopted sky correction are evident only in the cores of nebular lines H α , [N II] 6548,6584Å, He I, and [S II] 6717,6731Å.

Some of the B stars show a characteristic C II doublet at 6578-6583Å, which is typical of mid-B stars, but is enhanced in bright giants or supergiants (Grigsby et al. 1992, Sigut 1996, McErlean et al. 1999). We therefore consider these stars as candidate B supergiants, although some of them may be main-sequence B stars as well. We show some of these spectra in Figure 6-b, together with spectra of two known B supergiants (top two spectra) from the UVES/POP dataset (Bagnulo et al. 2003).

The Gaia-ESO spectra of two of our stars show features suggesting an O stellar type: these are the He II lines at 6527 Å and

6683 Å. Their spectra are shown in Figure 7-a (bottom two spectra), compared with known O stars from UVES/POP. The intensity ratio between He I 6678 Å and the neighboring He II 6683 Å line would be a sensitive measure of spectral type; however, the nebular contamination at 6678 Å is strong for both stars, since they are highly reddened and faint, which prevents accurate derivation of their spectral types. Furthermore, a large fraction of OB stars are spectroscopic binaries (Sota et al. 2014) and an examination of these lines in the sample covered by spectroscopic surveys such as OWN (Barbá et al. 2010), IACOB (Simón-Díaz et al. 2011), or CAFÉ-BEANS (Negueruela et al. 2015) reveal a number of cases where a B+B SB2 (each star with a He I 6678 Å line) masquerades as a single object with both He I and He II lines. Finally, He II 6527 Å is close to a broad DIB. Therefore, their identification as O stars based on their spectra is tentative at this stage. Both stars have already appeared in the literature on Carina stars, first as bright IR sources in Smith (1987 - the corresponding designation is reported in Fig. 7-a), then as candidate massive stars from both X-ray and IR observations (Sanchawala et al. 2007, Povich et al. 2011a); no optical spectra were however published for these stars before.

Finally, 17 stars are good or possible candidates as Herbig Ae/Be stars, having an A/B type and definite (regardless of sky-subtraction option chosen) wide emission at H α . We show some examples of these stars' spectra in Figure 7-b. Some of the spectra show also absorption or emission in the Fe II lines at 6456.38, 6516.08 Å, indicative of hot gas. While many of these stars' spectra show clearly wide H α absorption wings, underlying the circumstellar H α emission, in some cases the absorption component is overwhelmed by the wide emission component: in these cases the HAeBe nature is suggested by either a He I line, by the Fe II lines, or by the optical photometry, better consistent with an A-B type than with a lower-mass CTTS.

All massive stars found in our spectral dataset are listed in Table 7. The 'SIMBAD Id' column shows that all of these stars have also appeared in the SIMBAD database; however, for only 12 of them a B spectral type was already determined: therefore, the large majority of our early-type stars are new entries in the massive-star population of Carina, including all HAeBe stars. Incidentally, our complete spectral sample also includes two stars for which SIMBAD lists a B spectral type (with no reference given), while our spectra show definitely later (F and K) spectral types, as shown in Figure 8.

We have also matched our stellar sample with the lists of candidate massive stars from Sanchawala et al. (2007) and Povich et al. (2011a). Of the seven matches with the Sanchawala et al. (2007) candidates, we confirm a type earlier than early-A for 4 (at most 5) stars; only four of our stars match the Povich et al. (2011a) candidates, and all of them are confirmed as early-type stars. The combined list contains 11 massive star candidates, of which only 2-3 are not confirmed. Again, these are small numbers with respect to the number of new early-type stars found for the first time in our Gaia-ESO spectra (110 stars in Table 7), in a spatial region much smaller than the whole Carina region covered by the Povich et al. (2011a) study.

4.2. Photometric analysis with CHORIZOS

Some of the massive stars identified in this section are potentially interesting because their colors suggest large extinctions ($A_V \sim 5$ or higher) which are rarely found for objects immersed in H II regions. For that reason we selected 10 stars from Table 7 that are potential candidates for being highly extinguished. For seven

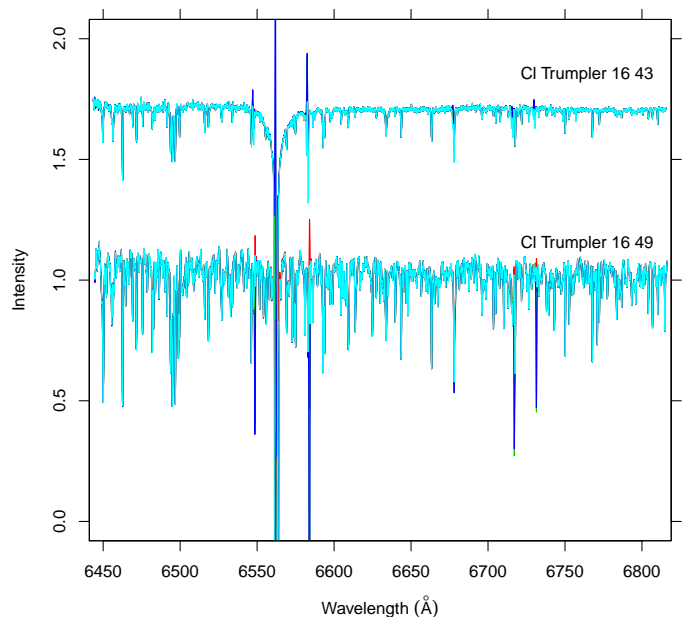


Fig. 8. Spectra of two stars mis-classified in the SIMBAD database as B stars, while they are respectively a K giant (lower spectrum), and a late-A or F star (upper spectrum). Spectra are labeled with their SIMBAD identifier. Color coding as in Figure 6.

of the stars *UBVIJHK* photometry is available from Hur et al. (2012) and 2MASS (Table 8) while for the remaining three only *BVIJHK* photometry exists (Table 9).

We processed the photometry described above using the CHORIZOS code (Maíz Apellániz 2014) in order to measure the extinction experienced by the stars and, to the degree in which it is possible, their effective temperature T_{eff} and logarithmic distance $\log d$. The procedure followed is similar to the one used in other papers such as Maíz Apellániz et al. (2015). With the purpose of obtaining independent assessments of these stars' properties, the results from the spectroscopic analysis above were not used as inputs here. We start by detailing the *UBVIJHK* photometry case:

- We used the Milky Way grid of Maíz Apellániz (2013a), grid parameters are effective temperature (T_{eff}) and photometric luminosity class (LC). The latter quantity is defined in an analogous way to the spectroscopic equivalent, but maps discrete classes I-V to a continuous variable in the range [0-5.5]. For objects with $T_{\text{eff}} > 15$ kK the spectral energy distributions (SEDs) are TLUSTY (Lanz and Hubeny 2003).
- The extinction laws were those of Maíz Apellániz et al. (2014), which are a single-family parameter with the type of extinction defined by R_{5495} (monochromatic analogous of R_V , see Maíz Apellániz 2013b). The amount of reddening is parameterized by $E(4405 - 5495)$.
- LC was fixed to 5.0 ("main sequence") in all cases except for [HSB2012] 3994, for which it was fixed to 1.0 ("supergiant"). T_{eff} , R_{5495} , $E(4405 - 5495)$, and $\log d$ were left as free parameters.

The *BVIJHK* photometry case was similar but it required an additional step. The problem with lacking *U*-band photometry is that T_{eff} and $\log d$ become quasi-degenerate (even if LC is known). R_{5495} and $E(4405 - 5495)$, however, are strongly constrained, as the different combinations of valid T_{eff} and $\log d$

yield almost identical values of the two extinction parameters. Therefore, the procedure we followed was to select a reasonable fixed value of $\log d$ and leave T_{eff} , R_{5495} , and $E(4405 - 5495)$ as free parameters.

The results of the CHORIZOS analysis are presented in Tables 8 and 9.

- We find values of R_{5495} between ≈ 3.6 and ≈ 4.9 , higher than the Galactic average but typical for an H II region.
- $E(4405 - 5495)$ ranges between ≈ 1.3 and ≈ 2.8 , reflecting the known strong differential extinction. The three stars with no U -band photometry have the three highest values of $E(4405 - 5495)$, as expected.
- Typically, A_V is determined with better precision than either R_{5495} or $E(4405 - 5495)$ even though, to a first approximation, $A_V \approx R_{5495} \cdot E(4405 - 5495)$. This is not incorrect because the likelihood in the R_{5495} - $E(4405 - 5495)$ plane is an elongated quasi-ellipsoid with negative slope i.e. R_{5495} and $E(4405 - 5495)$ are anticorrelated. This effect is commonly seen in fits to extinguished hot stars with CHORIZOS or similar codes.
- The most important result regarding the extinction is the location of four stars ([S87b] IRS 41, [S87b] IRS 42, [HSB2012] 1920, and [S87b] IRS 38) in the $E(4405 - 5495)$ - R_{5495} plane. A comparison with Figure 2 of Maíz Apellániz (2015) reveals that they are in a region where no other known Galactic OB stars are located. That is because for low values of $E(4405 - 5495)$ it is possible to find a large range of R_{5495} values but for large reddenings R_{5495} tends to be close to the average ~ 3.1 value. In other words, those four stars are exceptional in having large values of both $E(4405 - 5495)$ and R_{5495} , and their extinctions laws deserve a more detailed study.
- We plot in Fig. 9 the dependence of χ_{red}^2 of the CHORIZOS fit with reddening. For $R_{5495} < 4.0$, the fits are reasonably good even for values of $E(4405 - 5495) \sim 2.0$, indicating the validity of the extinction laws of Maíz Apellániz et al. (2014) for low R_{5495} . For $R_{5495} > 4.0$, there are good fits for low values of the reddening but χ_{red}^2 grows increasingly large as $E(4405 - 5495)$ increases, indicating that the extinction laws of Maíz Apellániz et al. (2014) need to be modified for large values of R_{5495} . This is not surprising, given that those laws were derived using stars with lower reddenings and here we are extrapolating to much larger values.
- For two of the B-type stars (as determined from the spectroscopy) with $UBVIJHK$ photometry ([HSB2012] 3017 and [HSB2012] 3994) the CHORIZOS-derived T_{eff} is consistent with them being mid-B stars. For the other five objects with $UBVIJHK$ photometry (from the spectroscopy, three B types, one B SG and one O type), the uncertainties in T_{eff} are larger and the values lean towards them being O stars. However, we should be cautious of that result, especially for the cases with high χ_{red}^2 . They could be late-O stars (with weak He II 6683 Å) or the fitted values for T_{eff} could be biased by the extinction law (Maíz Apellániz et al. 2014).
- [HSB2012] 3994 has an exceptionally large fitted distance (beyond the expected extent of the Galactic disk). One possible solution is that it is not a supergiant but instead a lower luminosity star. Even then, it is likely to lie beyond the Carina Nebula.
- Three other stars ([HSB2012] 230, [HSB2012] 1395, and [HSB2012] 2913) are also likely to lie beyond the Carina Nebula. On the other hand, the fitted $\log d$ for [HSB2012] 3017, [S87b] IRS 41, and [S87b] IRS 42 are compatible with

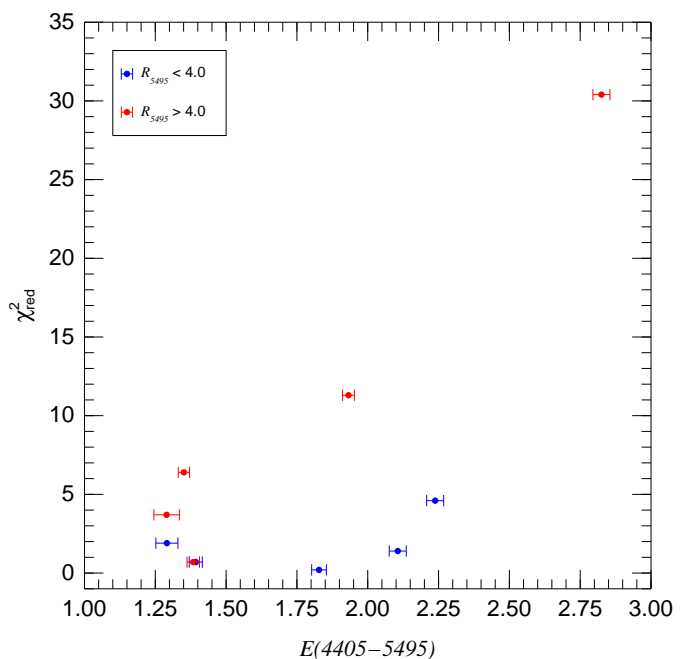


Fig. 9. χ_{red}^2 vs. $E(4405 - 5495)$ for the ten highly extinguished stars analyzed with CHORIZOS.

them belonging to the Carina Nebula Association. It should be pointed out that the latter list includes the two stars with the highest values of R_{5495} . That is an expected effect because for stars beyond the Carina Nebula one expects a larger contribution to extinction from the diffuse ISM and, hence, a lower R_{5495} .

We should note that the uncertainties derived by CHORIZOS are relatively small but not unrealistic because for over a decade we have worked to eliminate the systematic errors that have plagued other works. That includes recalculating the zero points for different photometric systems (Maíz Apellániz 2005, 2006, 2007), complementing and testing different atmosphere grids (Maíz Apellániz 2013a), deriving a new family of extinction laws that provides significant better fits to photometric data than pre-existing ones (Maíz Apellániz 2013b, Maíz Apellániz et al. 2014a), obtaining a library of data on reference stars to serve as a test bed for all of the above (Maíz Apellániz et al. 2004, (Maíz Apellániz and Sota 2008, Maíz Apellániz et al. 2011), and integrating everything into the code.

5. Spatial groups

The Carina Nebula is known to host a morphologically complex stellar population, distributed among approximately 20 sub-clusters and a sparse population according to Feigelson et al. (2011), of which Tr 14 and Tr 16 are only the most massive. Therefore, we define here several spatial groupings into which we conveniently split our sample stars. Among clusters defined in Feigelson et al. (2011), numbers 1, 3-6, 9-12, 14 fall in the region studied here. This is however a too detailed subdivision considering the number of optical spectra available here, so we prefer a simpler categorization. In Figure 10 we show the spatial distribution of all stars observed in Gaia-ESO, and known massive stars as a reference. The most massive stars are also coincident with the brightest X-ray sources (see Fig.1 in Antokhin et al. 2008), and are those exerting the strongest influence on their

Table 8. Results of the CHORIZOS fits for the seven highly extinguished stars with *UBVIJHK* photometry.

Star	T_{eff} kK	LC	R_{5495}	$E(4405 - 5495)$ mag	$\log d$ pc	A_V mag	χ^2_{red}
[HSB2012] 3017	22.2±2.5	5.0	3.62±0.08	1.291±0.039	3.50±0.07	4.688±0.077	1.9
[HSB2012] 230	41.8±5.3	5.0	3.95±0.07	1.393±0.023	3.88±0.11	5.531±0.036	0.8
[HSB2012] 1395	42.3±5.2	5.0	4.20±0.08	1.384±0.022	4.11±0.11	5.831±0.040	0.7
[HSB2012] 2913	40.8±6.0	5.0	3.69±0.05	1.828±0.026	3.85±0.12	6.756±0.040	0.2
[HSB2012] 3994	18.5±3.2	1.0	4.57±0.10	1.290±0.045	4.51±0.05	5.902±0.114	3.7
[S87b] IRS 41	42.4±4.4	5.0	4.92±0.09	1.351±0.020	3.37±0.09	6.669±0.034	6.4
[S87b] IRS 42	42.0±4.2	5.0	4.60±0.06	1.932±0.021	3.22±0.09	8.860±0.033	11.3

Table 9. Results of the CHORIZOS fits for the three highly extinguished stars with *BVIJHK* photometry.

Star	R_{5495}	$E(4405 - 5495)$ mag	A_V mag	χ^2_{red}
[HSB2012] 3880	3.64±0.06	2.106±0.030	7.636±0.040	1.4
[HSB2012] 1920	3.93±0.06	2.238±0.030	8.757±0.026	4.6
[S87b] IRS 38	4.07±0.05	2.825±0.030	11.394±0.034	30.4

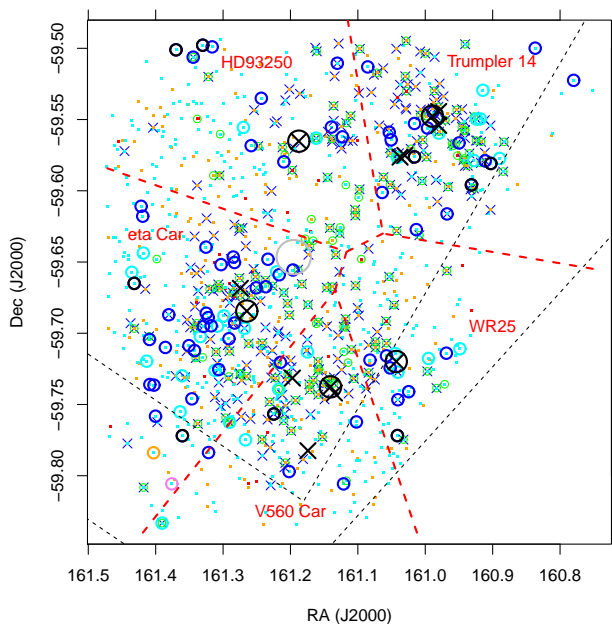


Fig. 10. Spatial map of observed stars. The lower right region is empty because of our sample selection choice. Symbols as in Figure 5, with the addition of big circles to indicate: B stars (blue), late-B to early-A stars (cyan), candidate B supergiants (black), and probable (orange) or possible (violet) O stars. We also plot here O stars from Walborn (1973) as black crosses. The most massive of them (surrounded by big black circles) are taken as centers of the respective sub-regions, bounded by red dashed lines and labeled in red after the central star names (except for Trumpler 14, whose central star is the O2If*+O3.5 binary HD93129A). Dashed black segments delimit the dark V-shaped dust lanes in front of the Nebula. The solid grey circle to the NW of η Car indicates approximate location and size of the Keyhole nebula (Smith and Brooks 2008).

neighborhood. Accordingly, we define five spatial regions, delimited by red dashed segments in the Figure, centered on stars HD93129A (O2If*+O3.5, central star of Tr 14), V560 Car (= HD93205, O3.5V((f+))+O8V), HD93250 (O4IIIcf:, central star of Collinder 232), WR25 (= HD93162, O2.5If*/WN6), and η Car.

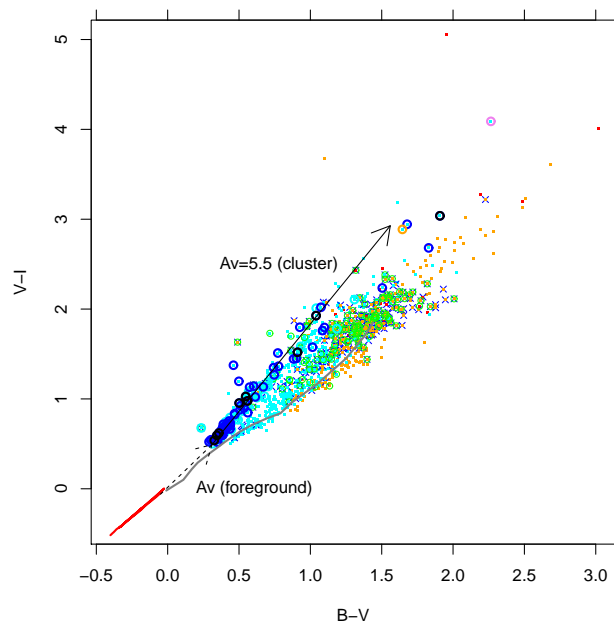


Fig. 11. A $(B - V, V - I)$ color-color diagram of the observed sample. Symbols as in Figs. 5 and 10. The thick red line is the unreddened locus of stars earlier than A0, while the thick grey line is the same for later-type stars. The reddening law appropriate for cluster stars is illustrated by the solid arrow, on top of the dashed arrow describing foreground absorption (and reddening law). The length of the solid arrow indicates the reddening of the new candidate O star 2MASS10453674-5947020 (star [S87b] IRS 42 in SIMBAD).

6. Reddening

Determination of optical extinction towards individual stars is very important to establish how they are distributed along the line of sight. A number of studies (e.g., Smith 1987, Hur et al. 2012) have determined that the foreground extinction towards Carina is relatively low ($E(B - V) \sim 0.36 \pm 0.04$, or $A_V^{fg} \sim 1.1$), while higher-reddening stars in the same region show an anomalous reddening law with $R = 4.4 - 4.8$. In the central part of Carina being studied here, highly obscured member stars have been found by means of X-ray observations (Albacete-Colombo

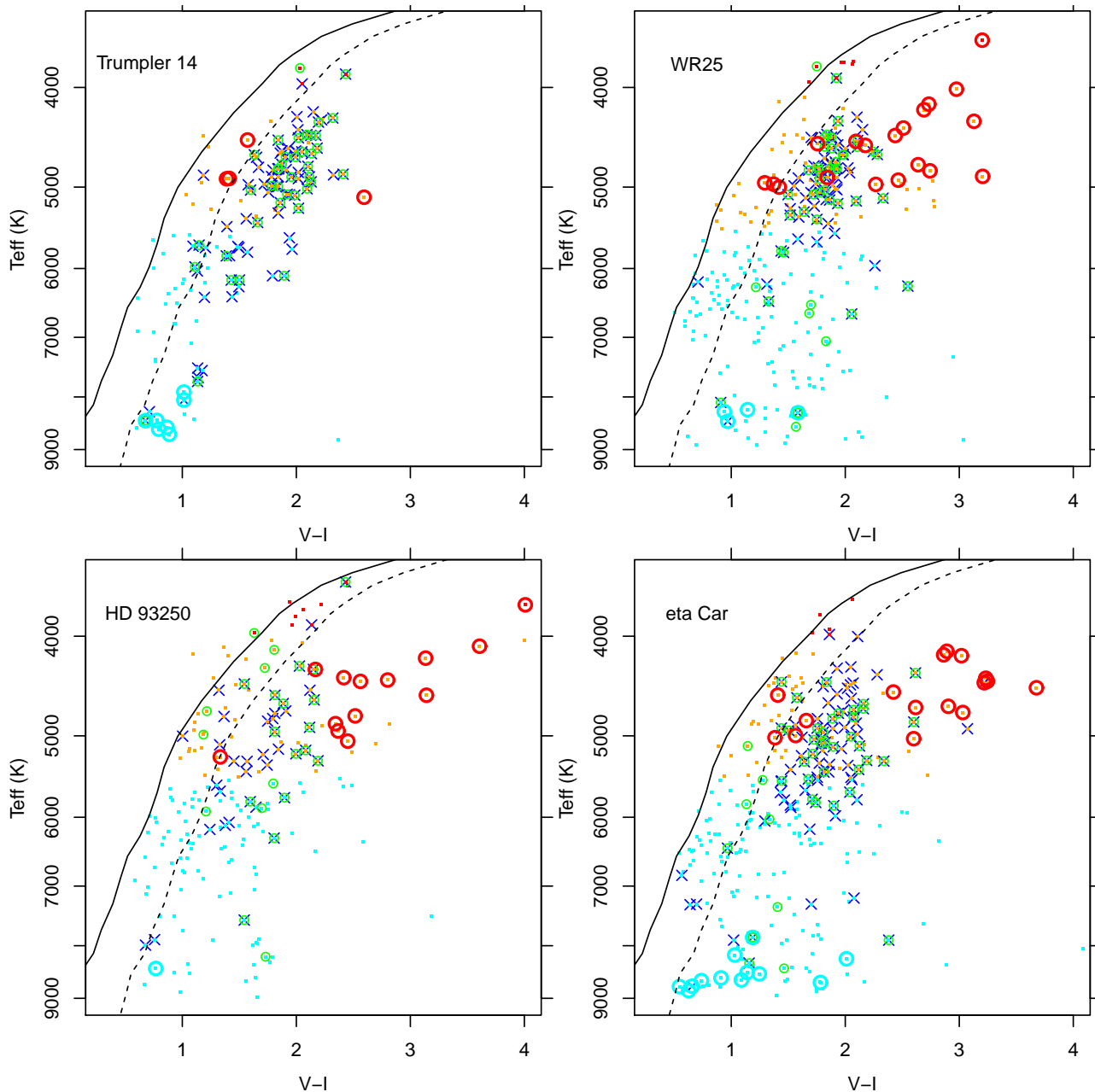


Fig. 12. Diagrams of T_{eff} vs. color $V-I$, for four spatial subregions as indicated. The KH95 T_{eff} -color relation is shown for zero reddening (solid) and for the cluster foreground reddening (dashed). Symbols as in Figs. 5 and 10. Big red circles indicate luminous low-gravity giants, probably located behind the Nebula.

et al. 2008; CCCP). Therefore, even considering only Tr 14/16 (and not the embedded clusters of Feigelson et al. 2011), cluster members are found over a large range of extinction values. The spatially highly non-uniform distribution of extinction is also made obvious by the two prominent SE and SW dark dust lanes.

Figure 11 shows a $(B-V, V-I)$ color-color diagram (using photometry from Hur et al. 2012), where in particular the colors of the early-type stars (large circles) found from our spectroscopy are useful to study the intra-cluster reddening law. The intrinsic colors of massive stars (down to A0) are described by the red line (3-Myr non-rotating solar-metallicity isochrone from Ekström et al. 2012, henceforth Geneva⁴), while those of lower-mass stars by the grey line (ZAMS from Kenyon and Hartmann

1995, henceforth KH95). Despite the lack of a detailed classification for the massive stars (Sect. 4), it is expected that most of them will be late-B/early-A stars, with colors $B-V \sim V-I \sim 0$. On this basis, the slope of the dashed arrow in Fig. 11 suggests that the foreground reddening law is $E(V-I)/E(B-V) = 1.53$ (slightly larger than the value 1.32 in Bessell et al. 1998), while inside Carina this ratio becomes 1.95 (slope of the black solid arrow), slightly larger than the value found by Hur et al. (2012) of 1.8 ± 0.1 from photometry alone. Figure 11 also shows that some of the B-type stars redder than $B-V \sim 1$ appear to have a lower $E(V-I)/E(B-V)$ ratio, more like a normal reddening law, although their spatial distribution shows no obvious pattern. Moreover, the two candidate O stars found in Sect. 4 are both found at very large reddenings (orange and violet circles), corresponding to intra-cluster extinction $A_V > 5.5$. Among stars with

⁴ <http://obswww.unige.ch/Recherche/evoldb/index/Isochrone/>

$B - V \geq 2$, the mentioned O star is the only candidate cluster member: the handful of other stars found in that color range are therefore obscured background giants, whose detection permits us to estimate the total optical extinction of the Nebula, and its spatial variation, as we will discuss below and in Section 9.

We have determined individual extinction values for our stars from their photometric $V - I$ colors, T_{eff} derived from our spectroscopy, and the T_{eff} -color relation from KH95 for ZAMS stars⁵; the $E(V - I)$ colors were converted to A_V using the above reddening laws as appropriate, i.e. differently for foreground extinction only ($A_V < 1.1$) and foreground+intra-cluster extinction, each with its reddening law. Because of our inability to assign a detailed spectral type and photometric color to the early-type stars, their extinction was computed by de-reddening their photometry to match the 3-Myr isochrone from Ekström et al. (2012). Figure 12 shows, separately for the different spatial groups (defined in Section 5), T_{eff} vs. $V - I$ diagrams for all of our stars. The solid line is the KH95 calibration at zero reddening, while the dashed line is the same curve at $A_V = A_V^{fg} = 1.1$; it is clear that most low-mass cluster members fall a little to the right of the latter curve. In this Figure we also show the placement of giant stars (defined from the γ index in Damiani et al. 2014) as red circles: as anticipated above, most of these giants lie at large reddening values⁶, and likely beyond the Carina Nebula. In the Trumpler 14 region virtually no background stars are seen: this might be related to a relatively higher extinction compared to other sightlines, and also to our incomplete target sampling combined with a locally enhanced member-to-field star density ratio.

7. Color-magnitude diagram

We show in Figure 13 the dereddened CMD of our sample stars. We find probable cluster members of masses down to one solar mass (or slightly below). The nonuniform reddening however prevents from establishing a mass completeness limit: in places where reddening is largest we cannot be sure of detecting even O stars (our candidate O star [S87b] IRS 38 has $V = 17.64$). Nonuniform reddening causes bright stars to be over-represented among optically selected samples such as this one, hence the relatively large number of B stars relative to solar-mass stars we find in our sample. This dataset is therefore unsuitable for studies (e.g. of the IMF) requiring statistically representative samples. From the Figure it is also apparent the scarcity of cluster members in the $(V - I)_0$ range 0.2-0.5, corresponding to late-A and F stars. The same lack of members can be observed in Fig. 12 at T_{eff} near 7000 K. Since lower-mass stars are found in larger numbers, this cannot be due to excessive reddening towards the F stars. One possible explanation for the small number of F-type members is the relatively fast traversal time across their radiative tracks in the CMD. In addition, we might lack the ability to assess their membership, as mentioned already in Sect. 3 for the A-type stars. Since F-type stars are generally found to be as strong X-ray emitters as G-type stars, we will consider again them in the context of the Carina X-ray data below.

Ages for the low-mass stars estimated from the isochrones in Fig. 13 are distributed mostly in the range 1-5 Myr, in agreement

⁵ Although the KH95 relation may be superseded by more recent calibrations, its usage here for deriving A_V is appropriate for best consistency with the T_{eff} calibration in Damiani et al. (2014).

⁶ The employed KH95 calibration is appropriate to ZAMS stars, and therefore the reddening values derived by applying it to giants are only approximate, but sufficient for our classification as background stars.

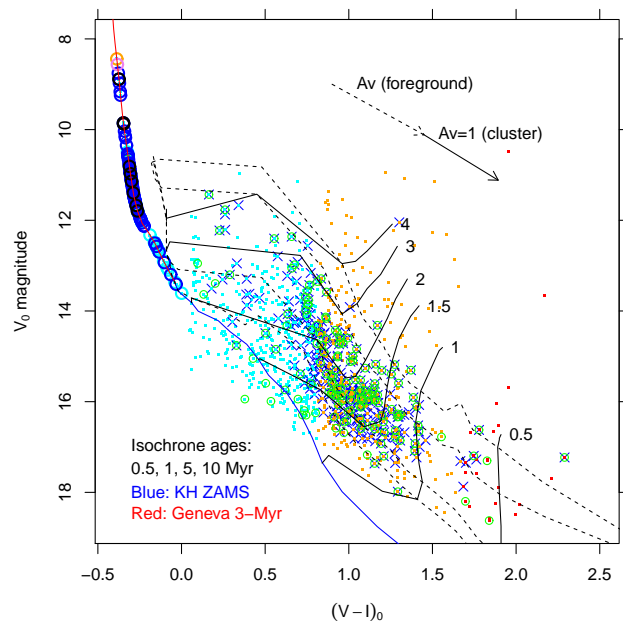


Fig. 13. Dereddened $(V, V - I)$ color-magnitude diagram. Symbols as in Figs. 5 and 10. Also shown are the ZAMS for lower MS stars (blue), a Geneva 3-Myr isochrone for massive stars (red), and selected isochrones (dashed black) and evolutionary tracks (solid black) for lower-mass stars from Siess et al. (2000); these latter are labeled with stellar mass in solar units. A0 and earlier-type stars have been projected to the MS (along the combined foreground+cluster reddening vector, as shown), since they lack a detailed classification.

with previous studies (e.g., Tapia et al. 2003, Carraro et al. 2004, Hur et al. 2012). As noted by e.g. Smith and Brooks (2008) or Wolk et al. (2011), not all clusters in Carina have the same age (Tr 14, in particular, is more compact and probably younger than Tr 16). The problem of establishing their age relationship will be discussed in Section 10.

8. X-ray data

In the subregion comprising Tr 16 and WR25 we find approximately 180 low-mass candidate Carina members. Considering that our target selection involved a $\sim 50\%$ down-sampling of all candidate members from optical photometry down to $V = 18.5$, we can extrapolate to ~ 360 members down to that magnitude limit: this is much smaller than the number of X-ray sources (1035) found in the same region by Albacete-Colombo et al. (2008). An even larger number was found in the CCCP X-ray survey, although based on the same Chandra observation in the field of Tr 16, because of the less conservative choices adopted in detecting point sources. Spurious detections in Albacete-Colombo et al. (2008) are predicted not to exceed ~ 10 sources, and the number of unrelated field X-ray sources is ~ 100 , so that the number of X-ray members in this subregion remains > 900 . Therefore, a significant excess of ≥ 500 X-ray sources remain, above the number of members inferred from our spectroscopic data. These must be stars fainter than our $V = 18.5$ selection limit, either because of their low mass, or because of large extinction (or both). Since their number is not small with respect to the spectroscopically studied sample, we cannot overlook them for a proper understanding of the properties of the SFR. Here we try to investigate their nature.

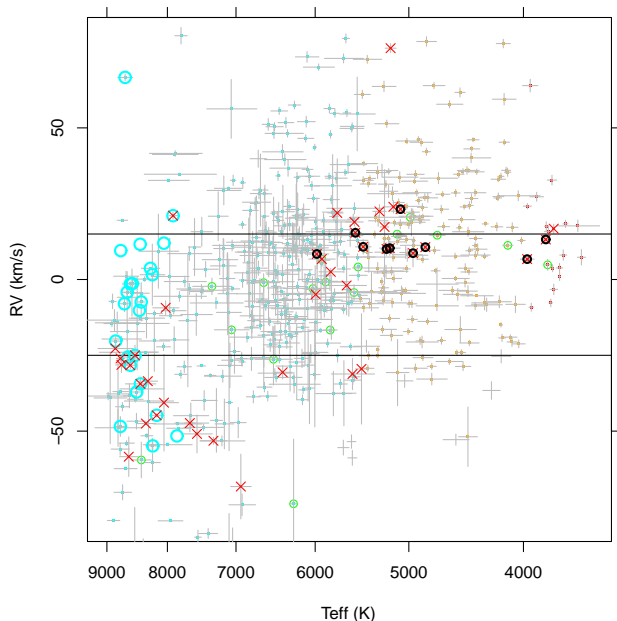


Fig. 14. RV vs. T_{eff} for stars not classified as members. Symbols as in Figure 5, with the addition of red crosses representing X-ray detected stars, unconfirmed by other membership indicators. Bars indicate statistical errors only. The RV10 stars are indicated with black circles. The horizontal lines indicate the cluster RV range.

Forty X-ray detected late-type stars (21 from Albacete-Colombo et al. 2008) were observed spectroscopically, but not classified here as members; of them, 11 are RV10 stars, and 6 are near-ZAMS rejected members discussed in Section 3. We first examine whether this can reveal a failure of our membership criteria. These stars do not cluster at any particular place in the CMD diagram, and there is no reason to conclude that as a group they should be included among members. The same conclusion is reached from Figure 14, showing RV vs. T_{eff} exclusively for non-member stars: the X-ray emitting non-members are randomly scattered, and in particular their membership status would not change by any small adjustment of the nominal RV range for members (horizontal lines). We recall that, if these X-ray sources had lithium EW above 150 mÅ, they would have been accepted as members even in the presence of discrepant RV (in order not to lose binaries)⁷. Thus, the red crosses in Fig. 14 have not only discrepant RV but also no lithium. As discussed above, in the T_{eff} range 9000-7000 K our membership criteria may be weakest; yet, even in this range the number of potential candidates from X-rays is very small, and they appear to have all significantly discrepant RV. Therefore, these X-ray detected stars with no lithium and discrepant RV are unlikely members, and will not be considered further⁸. We also conclude that the lack of member stars in the temperature range 9000-7000 K is real, and not a byproduct of our membership criteria. This is probably related to the R-C gap found in the photometric CMD

⁷ The few red crosses inside the nominal RV range were rejected as members because of their proximity to the ZAMS, as explained above.

⁸ Of these 40 stars, 37 are classified by Broos et al. (2011b) within the CCCP project, on the basis of X-ray properties and optical/NIR photometry alone: all but four (unclassified) objects were assigned to the “Carina young star” group, including thus the majority of near-ZAMS and RV10 stars, which we instead excluded on the basis of the Hur et al. (2012) photometry, and our RVs, respectively.

of several clusters by Mayne et al. (2007); the same effect is not recognizable in the CMD of Carina clusters because of strong differential extinction.

Next, we examine the X-ray properties of X-ray detected sources which have not been observed spectroscopically. We take the list of sources and their properties from Albacete-Colombo et al. (2008). Figure 15-a compares cumulative distributions of extinction A_V (as derived from the near-IR colors, for X-ray sources with a 2MASS counterpart), for the X-ray sources in the spectroscopic sample and in the no-spectroscopy sample. A Kolmogorov-Smirnov (KS) statistical test gives a probability P that the two distributions are drawn from the same parent sample of only $P = 4.9 \cdot 10^{-5}$, confirming the significance of their visually apparent difference. Similar results are obtained from consideration of the absorbing column density N_H , as derived from model best fits to the Chandra ACIS X-ray spectra (Albacete-Colombo et al. 2008), whose distributions for the spectroscopically observed and unobserved samples of X-ray sources are also shown in Figure 15-a: here a KS test gives a probability of $P = 1.83 \cdot 10^{-6}$ that the two distributions are drawn from the same parent sample. The two tests just made do not refer exactly to the same subsamples of X-ray sources, since only 2/3 of the X-ray sources in Albacete-Colombo et al. (2008) have a 2MASS counterpart, and only those detected with more than 20 X-ray counts had a spectral fit performed. Nevertheless, there is definite evidence that the optically missed, X-ray detected members are more obscured than the stars in our spectroscopic sample.

This finding does not rule out that the X-ray detected sample may contain also a number of low-extinction members at fainter optical magnitudes than our limit. To test this, we consider the distributions of X-ray luminosities L_X , derived from X-ray spectral fits and therefore corrected for absorption, for the spectroscopic and no-spectroscopy samples, as shown in Figure 15-b: the KS test gives a probability of no difference of $P = 2.2 \cdot 10^{-16}$. Young PMS low-mass stars are known to be in an X-ray saturated regime, where the X-ray luminosity L_X is on average proportional to stellar bolometric luminosity, $L_X \sim 10^{-3} L_{\text{bol}}$ (Flaccomio et al. 2003, Preibisch et al. 2005, Damiani et al. 2006a); therefore, the lower (unabsorbed) X-ray luminosities of stars without spectroscopy implies that these stars have on average lower luminosities (and mass) than our spectroscopic sample. The X-ray detected member sample is therefore more complete than the spectroscopic sample both towards lower masses and towards more obscured stars.

9. Cluster structure

We attempt here to combine all data discussed above in a single coherent picture of the structure of central Carina. We first test the meaningfulness of the derived extinction values A_V , by comparing them with a spectroscopic gravity index γ , defined in Damiani et al. (2014). The prediction being tested here is that all main-sequence stars later than mid-G, being only observable in the foreground of the Nebula, must have $A_V \leq A_V^{fg}$, while most giants will appear in the background, having a much lower space density but higher luminosity. Figure 16 shows that this is exactly the case: high-gravity, main-sequence GKM stars have $\gamma < 0.97$, and the vast majority of them is found at $A_V \leq A_V^{fg}$, while giants (having $\gamma > 1.02$) are almost all found in the A_V range between 2-5 mag, typically larger than the extinction towards cluster members.

Having better established our confidence in the determined extinction values, we next consider the spatial distributions of

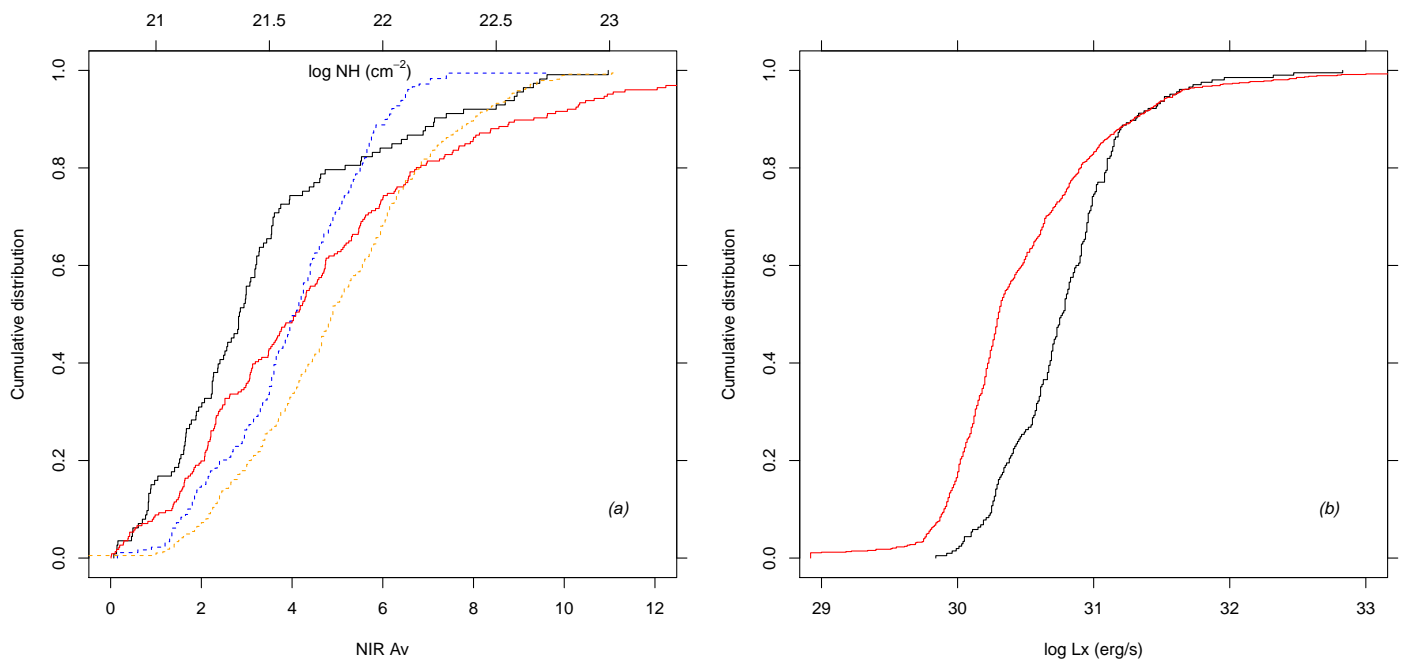


Fig. 15. (a): Solid: Cumulative distributions of A_V (derived from NIR colors), for Tr 16 X-ray sources observed here spectroscopically (black) and unobserved (red). Dashed: Cumulative distributions of gas column density N_H (scale on top axis), for the same subsamples (blue and orange respectively). (b): As in panel (a), for the X-ray luminosity L_X .

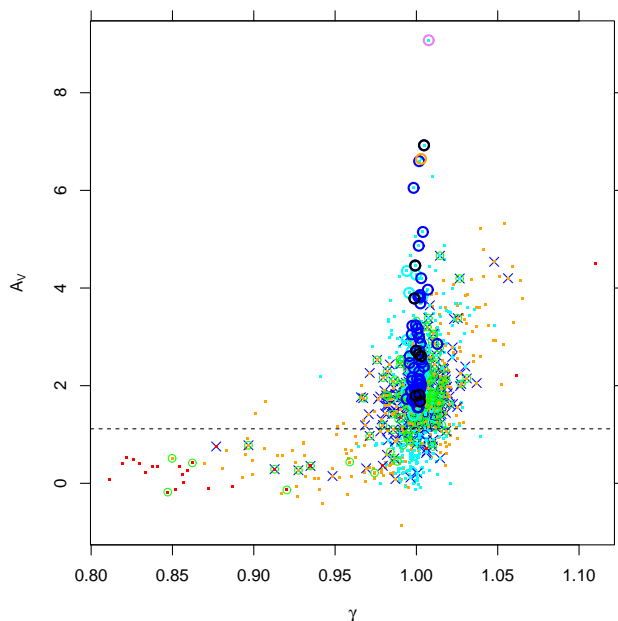


Fig. 16. Optical extinction A_V vs. spectral index γ . Symbols as in Figs. 5 and 10. For GKM stars, γ is an effective gravity diagnostics, with high-gravity stars having $\gamma < 0.97$ and giants having $\gamma > 1.02$. The horizontal dashed line indicates the foreground extinction value.

stars in several ranges of A_V , as shown in Figure 17. The upper left panel shows all stars with $A_V < 0.8$: no clustering is detectable, in agreement with these being foreground stars, unrelated to Carina and its obscuring material. Tens of stars are found projected against the dark V-shaped dust lanes. The number of low-gravity stars (red circles) is here very low. In the upper right panel, the low-extinction cluster members appear, in dense groups with close spatial association to the most massive

stars; the dust lanes are here almost devoid of stars, except for a dozen (probably background) stars near WR25, where the total absorption is lower than elsewhere in the lane (see e.g. Fig. 1 in Albacete-Colombo et al. 2008). Most of the B-type stars have not yet made their appearance in this A_V range: this makes the number ratio between the early-type and the solar-type stars here probably more representative of its real value. In the next extinction range, shown in the lower left panel, the stellar distribution has changed considerably: low-mass members are more widely dispersed away from the most massive stars, while their density generally increases towards places of higher obscuration. This is seen in the vicinity of η Car, which has now many more neighbors towards SE (where they eventually meet the dark lane) than towards NW, and also in the Trumpler 14 region, where again member stars are found exclusively on the side of the cluster nearest to the dark lane. Taking the dashed black lines in the Figure as a reference, we may observe that the number of stars in their immediate vicinity, in both the Tr 14 and η Car subregions, increases dramatically from the low-extinction layer to the higher-extinction one. This is also true for the B/early-A stars, most of which found on the high-extinction sides of Tr 14 and η Car, respectively. The South-West and North-East regions, around WR25 and HD93250/Collinder 232 respectively, show several low-gravity background giants, indicating that the total Nebula extinction in those regions does not exceed $A_V \sim 2 - 3$. No background giants are instead found on the high-extinction sides of Tr 14 and η Car, nor in the dark lanes (except for the vicinity of WR25 as already remarked). Finally, the lower right panel shows the most reddened stars found in our dataset: only early-type cluster members are found here, including the two candidate O stars (both under the SE obscuring lane) and three candidate B supergiants; at these extinction values, background giants make their appearance even close to the SE dark lane, but not in the region surrounding Tr 14. This extinction pattern agrees qualitatively with that in Smith and Brook (2007; their Fig. 5a).

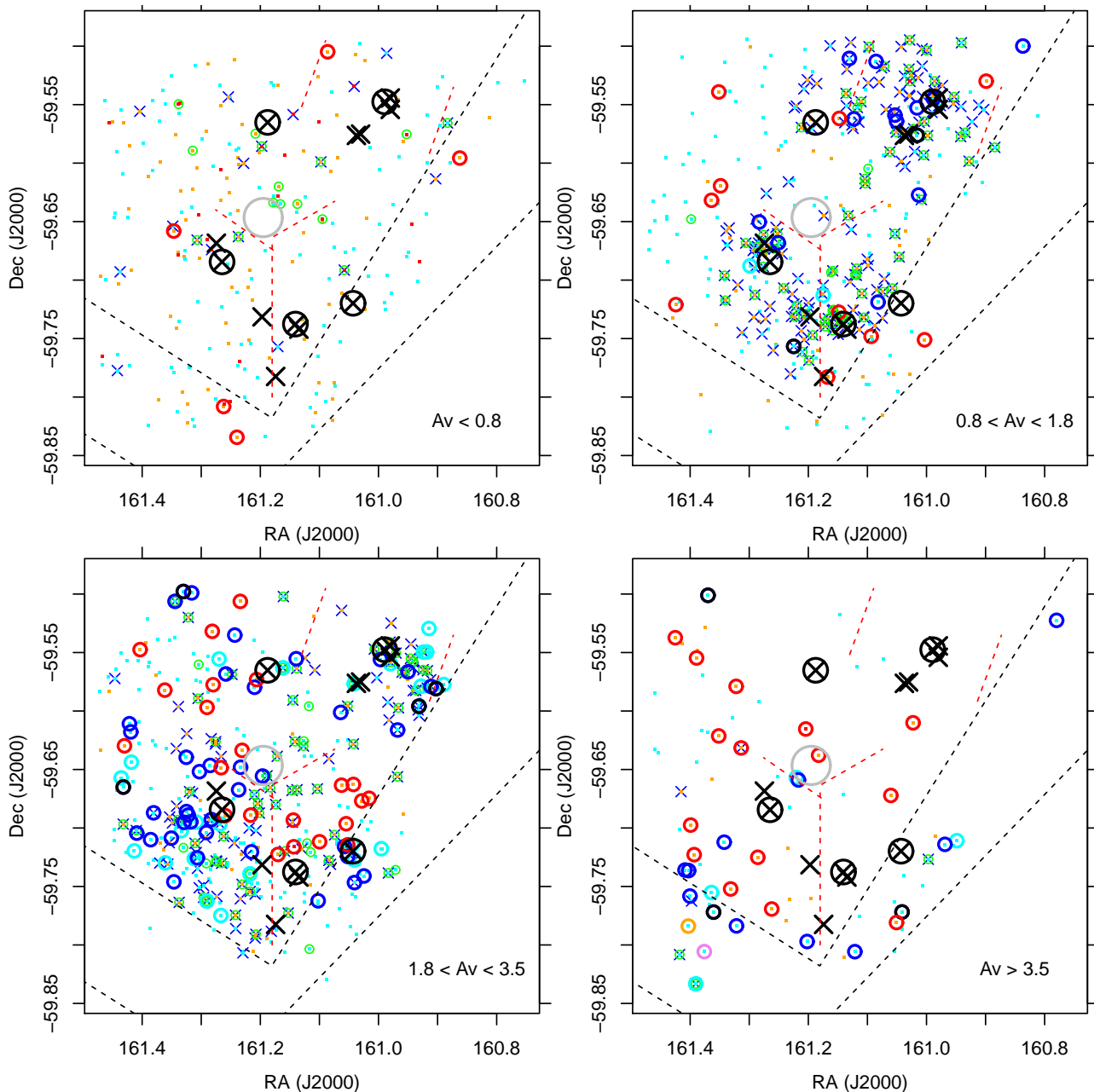


Fig. 17. Spatial maps of observed stars, split in four ranges of A_V as labeled. Star symbols as in Fig. 10, with the addition of red circles indicating low-gravity giants as in Fig. 12. Dashed black lines indicate the dark dust lanes as in Fig. 10. Dashed red segments indicate the boundaries of large gas shells studied in Paper I. The big grey circle indicate position and approximate size of the Keyhole nebula.

Figure 18 shows all stars with $A_V > 1.8$ together with X-ray detected sources in Tr 16 (most of which members as discussed above) with X-ray hardness index $HS > 0.5^9$, and therefore moderate to large absorption, and not observed spectroscopically. Most moderately-obscured X-ray sources (orange triangles) lie South of η Car and between it and WR25, while the heavily-obscured X-ray sources (brown triangles) lie behind the southern dark lane, with the largest source density found between the two new candidate O stars. This subcluster of highly absorbed X-ray sources is named CCCP-C1 14 in Feigelson et al. (2011), and Tr 16 SE in Sanchawala et al. (2007). Its dominant star, according to Feigelson et al. (2011), is the O eclipsing bi-

⁹ HS is defined as the count ratio between bands [2-8] keV and [0.5-2] keV.

nary FO 15 (= V662 Car, O5.5Vz + O9.5 V,v), which however we did not observe spectroscopically. The optical extinction of this star is $A_V \sim 5$ (Niemela et al. 2006), thus lower than that we find for our candidate O stars [S87b] IRS 42 and IRS 38 ($A_V = 6.6$ and 9.1 , respectively) in the same region. At the same location, an obscured cluster of massive stars was found from Spitzer images by Smith et al. (2010 - called 'cluster G' in their Table 4), who argued that this is not an embedded, extremely young cluster, but more likely a cluster of age 1-2 Myr, behind and not inside the foreground dark lane.

Figure 18 shows no clear separation between subclusters, in proceeding from η Car to its SE, but only a gradually increasing proportion of highly absorbed Carina members, both massive and of low-mass (the latter only from X-rays). Instead, the low-extinction members (in Figure 17, upper right panel) are much

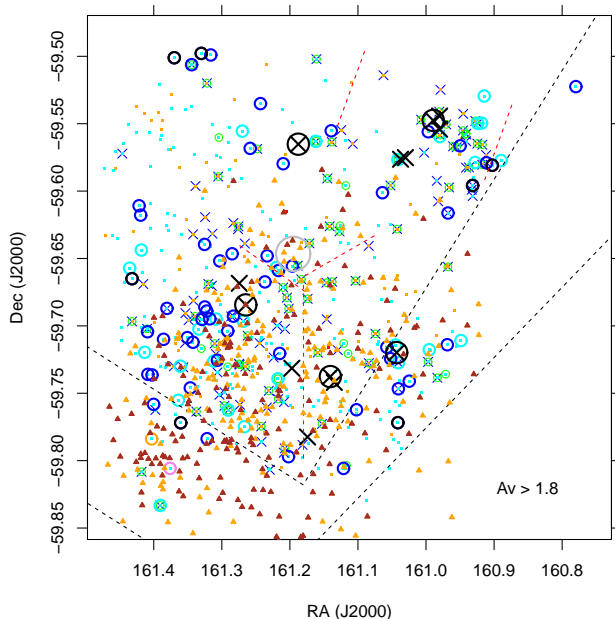


Fig. 18. Spatial map of reddened sample stars with $A_V > 1.8$ (shown by same symbols as in Fig. 17), and of obscured X-ray sources (orange triangles: $0.5 < HS < 1.0$; brown triangles: $HS > 1$).

more clustered in tight groups centered on the respective massive stars. It is interesting to compare the distribution of stars with that of the ionized gas from Paper I, consisting of several large shells, almost devoid of dust, centered on η Car, WR25, and Tr 14. The observed gradual increase in extinction towards SE, if most stars are enclosed in such dust-free shells, implies that the obscuring material must lie in front of the star clusters (and gas), and not generally mixed with them. At its SE border, the η Car gas shell does not seem to interact with matter in the dark lane, but instead fades behind it: this agrees with the conclusion by Smith et al. (2010) that the obscured SE subcluster (their 'cluster G') lies behind the lane and does not interact with it. This is probably true also of the newly found massive OB stars in the direction of the dark lanes, so that their UV radiation would illuminate most cluster stars with little attenuation, despite the very large extinction found towards us. Of course, circumstellar dust may still exist around individual stars, which contributes to the A_V scatter in Fig. 17 and shields the massive-star UV flux; however, since we do observe a regular spatial extinction pattern in Fig. 17, local extinction is probably a minor contributor to the total observed A_V .

Behind the high-reddening members of Tr 14, with $A_V \leq 3$, we do not find virtually any background star. Except for the Tr 14 region and the dark lanes, we have instead found background giants throughout most of the surveyed part of Carina, and therefore we have been observing the brightest members through the entire thickness of the nebula until its far side.

10. Stellar ages

We investigate here if there are measurable age differences between the Carina subclusters. A useful age diagnostics for young low-mass stars is the lithium resonance line at 6707\AA , whose EW as a function of T_{eff} was shown in Fig. 5. In the temperature range of the Carina members studied here, however, lithium EW is insensitive to age if a cluster is younger than sev-

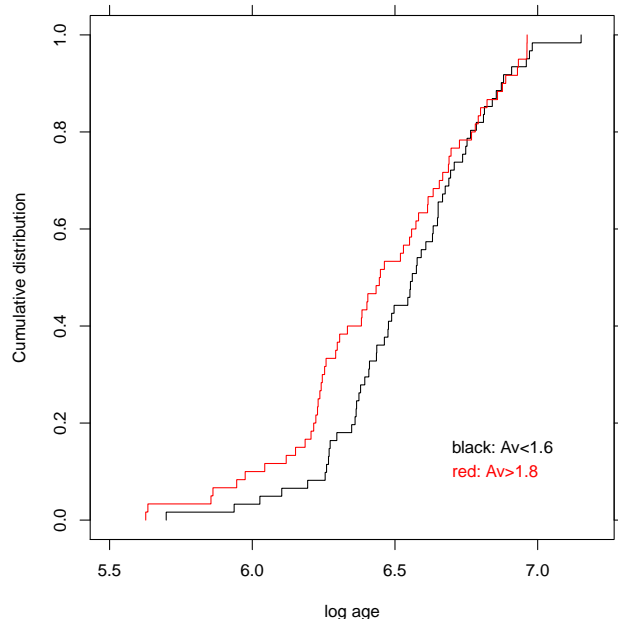


Fig. 19. Cumulative distributions of photometric ages, for all members in the T_{eff} range 4300-6500 K. Black lines: $A_V < 1.6$; red lines: $A_V > 1.8$.

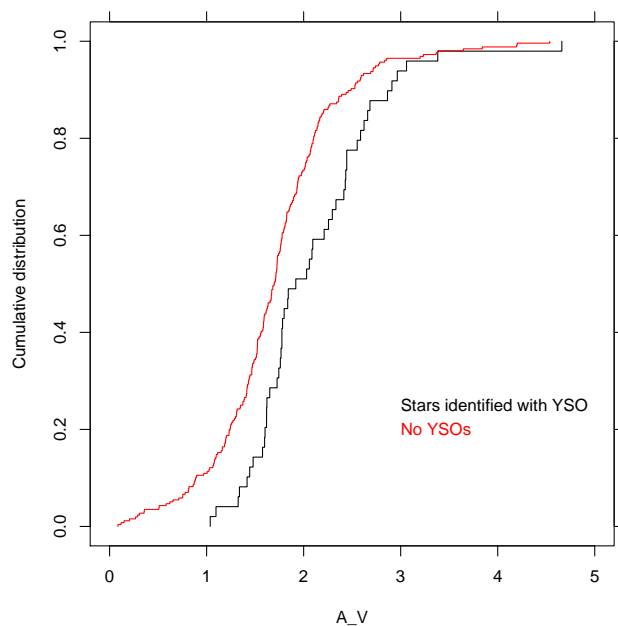


Fig. 20. Cumulative A_V distribution for members identified with a YSO from Zeidler et al. (2016) (black line), and for those without a YSO counterpart (red).

eral tens Myr (Jeffries 2014), as is the case for Carina clusters. Accordingly, the scatter of datapoints in the above figure may be entirely accounted for by errors on T_{eff} ($\sim 5\%$) and lithium EW, and is not related to real age differences among the observed Carina members.

We examine the relative ages of the different Carina subgroups as derived from the star location in the CMD, compared to Siess et al. (2000) isochrones. This method still benefits from our spectroscopic data since apparent star colors and magnitudes are individually de-reddened using the extinction values A_V de-

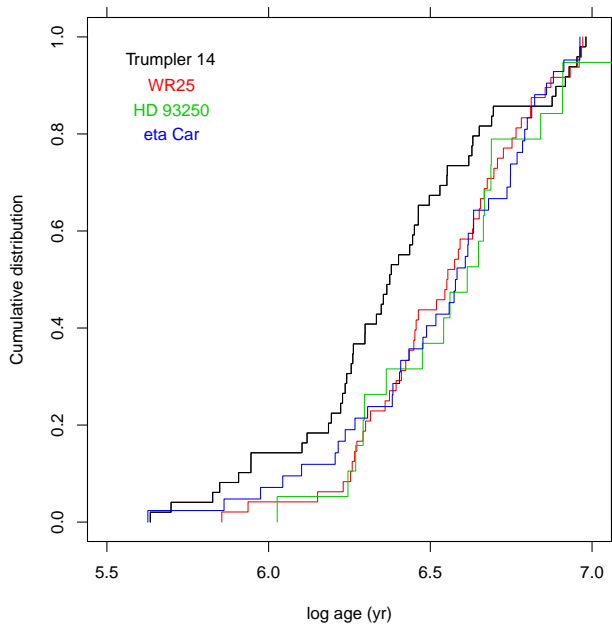


Fig. 21. Cumulative distributions of stellar ages as derived from photometry and isochrones, as in Fig. 13, for cluster members from different subgroups.

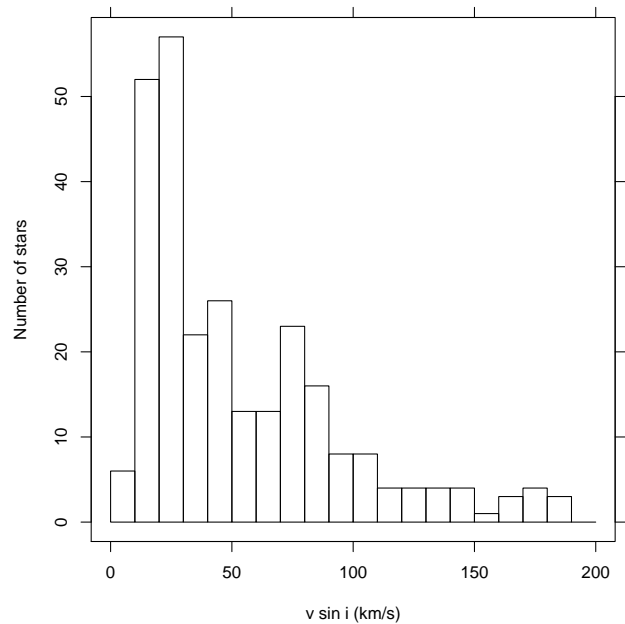


Fig. 22. $v \sin i$ distribution for Carina members with $4500 < T_{eff} < 6500$ K.

rived above. Besides that, there remain a series of caveats related to non-photospheric contributions such as veiling in accreting PMS members, uncertainties in the reddening law, or unrecognized binaries.

The distributions of photometric ages for low- and high-extinction subsamples are shown in Figure 19: both distributions are rather wide, over more than one dex in ages. This agrees with the earlier result of DeGioia-Eastwood et al. (2001) that star formation in these clusters was active over the last 10 Myr, which should be taken as an upper limit to the true age spread considering e.g. uncertainties in extinction and reddening law, binarity, or variability. The difference between the two distributions in the Figure points to the obscured Carina population being slightly younger than the unobscured one, however with a modest statistical significance of 93.9%.

To corroborate this result, we show in Figure 20 the cumulative distributions of A_V for Carina members with and without a YSO counterpart in the Zeidler et al. (2016) catalog: (younger) members associated with a YSO have a larger extinction than (older) members with no YSO association, with a confidence level of 99.6%.

The cumulative distributions of photometric ages of Carina member stars in the subclusters are shown in Figure 21: stars in Tr 14 are significantly younger (at 99.1% level) than those of all other subgroup (cumulatively), while the age distributions of η Car, HD93250 and WR25 subgroups are indistinguishable from one another. This agrees with the already mentioned suggestion that Tr 14 is younger than Tr 16.

11. Rotation

The HR15n spectra of Carina members show that a large fraction of these stars, including lower-mass ones, are fast rotators, with a median $v \sin i \sim 40$ km/s for $4500 < T_{eff} < 6500$ K (Figure 22). To our knowledge, these are the first measurements of rotation rates for Carina PMS stars. Since average stellar rotation

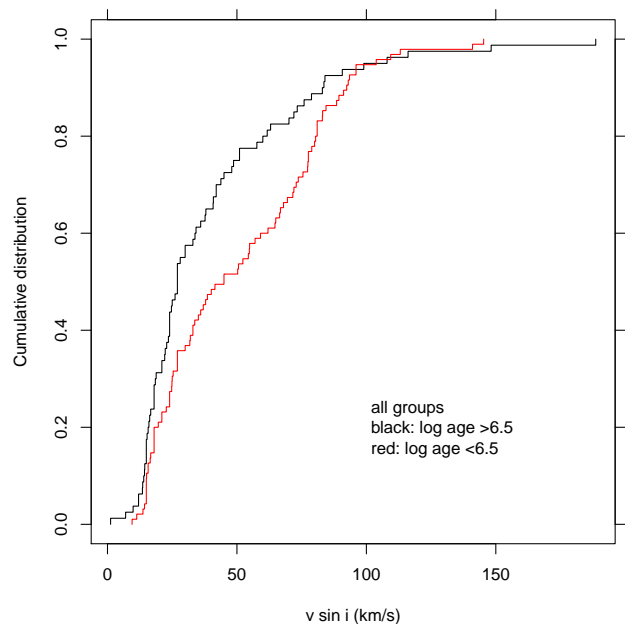


Fig. 23. Cumulative $v \sin i$ distributions for low-mass member stars from all groups, split by photometric age. Black: log age > 6.5 ; red: log age < 6.5 (yr).

rates are strongly mass-dependent, we have chosen for the above Figure a restricted T_{eff} range. Moreover, the Figure suggests a bimodal distribution, with a higher peak near $v \sin i \sim 22$ km/s, and a secondary one at $v \sin i \sim 75$ km/s, qualitatively similar to that in the ONC (Stassun et al. 1999, Herbst et al. 2002) for masses larger than $0.25M_{\odot}$. Assuming a typical radius for our Carina PMS stars of $2R_{\odot}$, the $v \sin i$ peaks would transform into rotational-period peaks around 1.1 and 3.6 days, respectively, not significantly different from those found in the ONC. We do not find a significant difference between the rotational velocity dis-

tributions of CTTS and WTTS, neither globally nor considering each subgroup separately; however, as we have discussed in section 3, an accurate assessment of CTTS status is difficult using our spectra. We have therefore examined the $v \sin i$ distributions for stars with and without NIR excesses, as measured using the 2MASS ($H-K$, $J-H$) color-color diagram (as e.g. in Damiani et al. 2006b), or the Spitzer IRAC ($[3.6-4.5]$, $[5.8-8.0]$) diagram (as in Povich et al. 2011b). In our Carina sample only very few stars are found with significant excesses in these NIR/MIR colors, and their rotational-velocity distribution is not significantly different from that of stars with no excesses. Last we have considered our Carina members with a counterpart in the YSO catalogue of Zeidler et al. (2016): the $v \sin i$ distributions for stars associated and unassociated with a YSO are different at the 92.5% significance level. This is marginal, probably because of the limited member sample size. The sense of the difference, nevertheless, seems to indicate that stars surrounded by a massive dust disk spin slower than stars with no disk, giving some support to the disk-locking paradigm (e.g., Mathieu 2004, Rebull et al. 2006).

We find a more significant difference (at 98.55% level) between sample stars respectively younger and older than 3 Myr (Figure 23). The older stars rotate more slowly than younger ones. This result is similar to that found by Littlefair et al. (2011) for several other young clusters. This is surprising for mostly diskless PMS stars, which should spin up as their moment of inertia decreases during contraction. However, stars in this Carina PMS sample belong mostly to the mass range $1-4M_{\odot}$, and nearly half of them lie along radiative tracks, where contraction is much slower than along the Hayashi track (according to the Siess et al. 2000 models, radius even increases along part of the radiative track for some masses in this range). The richness of Carina, coupled to our limiting magnitude, makes that the stellar mass composition of our sample is very much complementary to that of most existing studies of rotation in young clusters: we are unable to study the rotation of stars below $\sim 1M_{\odot}$, but have a sample of PMS stars in the $\sim 1-4M_{\odot}$ range of a size hardly found in any other studied cluster. Therefore, the Carina rotation data can be very important to study the rotational evolution of PMS stars along their radiative track. Similar datasets are still lacking for SFRs in the same richness class as Carina, like those mentioned in Sect. 1.

Besides the difference between younger and older Carina members, Fig. 23 shows that the bimodal $v \sin i$ distribution is only found in the younger subsample: the older one does not show two bumps in the cumulative distribution (the histogram peaks correspond to the steepest derivatives in the cumulative distribution). This may be related to the development of the radiative stellar core, which has a profound influence on the observed surface rotation (see e.g. Spada et al. 2011). Again, the Carina rotation data may be crucial for testing theoretical models of rotational evolution along the radiative track.

12. Discussion and conclusions

Our study of the Gaia-ESO dataset on Tr 14/16, the richest clusters in the Carina complex, is to our knowledge the first extensive spectroscopic exploration of a sizable sample of stars in a giant SFR, with a mass in excess of $10^4 M_{\odot}$, of which Carina is a rare example. Out of 1085 stars observed, more than 100 turned out to be early-type stars, mostly lacking a spectroscopic classification; among them are two new candidate O stars at high extinction, already known as bright IR sources, 17 candidate Herbig Ae/Be stars, and 9 candidate B supergiants, although the limited

wavelength range of the studied data prevented a more detailed classification. Based on RV, lithium, and X-ray data, we find 286 Carina low-mass members. Their number ratio with respect to the massive stars is not representative, because the wide range in extinction encountered favors observation of bright member stars at high reddening.

We have confirmed the anomalous reddening law already reported, and placed new constraints on the three-dimensional space distributions of Carina members. In central Carina, there is a relatively small percentage of embedded YSOs (Povich et al. 2011); this and other constraints posed by our previous study of the ionized gas distribution (Paper I) suggest a picture where the extinction towards Carina young stars in the η Car/Tr 16 region is mostly caused by dust at some distance from the stars themselves, not mixed with them. This has impact on the amount of UV flux they receive from the most massive cluster stars, and on the consequences that this is likely to have on the evolution of the circumstellar disks (photoevaporation). It is worth noting that some information on the local level of UV irradiation may also come from a detailed analysis of some of the DIBs found in the red spectra of these stars (Kos and Zwitter 2013).

The geometry of the studied region in Carina is not simple. We observed background giants through several sightlines across the studied region, behind a few magnitudes of optical extinction. The dust lane to SE, close to η Car, produces enough obscuration to drive a candidate O star near to our limiting magnitude: of course still more deeply obscured massive stars may exist in the same direction. If a blister geometry applies to this part of the cloud, this must be seen sideways from our sightline. In the Tr 14 region close to the western dark lane, instead, the foreground obscuration is a little more uniform, but rises more sharply towards the dust lane. The two dust lanes have therefore a different placement in space with respect to their nearest cluster.

The data suggest a complex history of star formation, with a significantly younger age for Trumpler 14 with respect to all other Carina subgroups. The high-extinction stars are only slightly younger than the low-extinction ones, and more frequently associated with a YSO.

Because of its richness, Carina also provides us with a sample of PMS stars in the $1-4M_{\odot}$ range, of a size hardly found in other young clusters. We have presented $v \sin i$ distributions for this unique sample of stars (significantly larger than e.g. in the study of intermediate-mass star rotation by Wolff et al. 2004, in the ONC). About one-half of these stars are evolving along radiative tracks. We find evidence of a bimodal $v \sin i$ distribution, analogous to that found in the ONC for lower-mass stars. Stars older than 3 Myr, and mostly on their radiative PMS track, are found to rotate slower than younger stars, which puts constraints on the rotational evolution of intermediate-mass PMS stars.

Acknowledgements. We wish to thank an anonymous referee for his/her helpful suggestions. Based on data products from observations made with ESO Telescopes at the La Silla Paranal Observatory under programme ID 188.B-3002. These data products have been processed by the Cambridge Astronomy Survey Unit (CASU) at the Institute of Astronomy, University of Cambridge, and by the FLAMES/UVES reduction team at INAF/Osservatorio Astrofisico di Arcetri. These data have been obtained from the Gaia-ESO Survey Data Archive, prepared and hosted by the Wide Field Astronomy Unit, Institute for Astronomy, University of Edinburgh, which is funded by the UK Science and Technology Facilities Council. This work was partly supported by the European Union FP7 programme through ERC grant number 320360 and by the Leverhulme Trust through grant RPG-2012-541. We acknowledge the support from INAF and Ministero dell'Istruzione, dell'Università e della Ricerca (MIUR) in the form of the grant "Premiale VLT 2012". The results presented here benefit from discussions held during the Gaia-ESO workshops and conferences supported by the ESF (European Science Foundation) through the GREAT Research Network

Programme. R. B. acknowledges financial support from INAF under PRIN2013 Programme 'Disks, jets and the dawn of planets'. This research has made use of the SIMBAD database, operated at CDS, Strasbourg, France. This work was also using data products from observations made with ESO Telescopes at the La Silla Paranal Observatory under programme ID 177.D-3023, as part of the VST Photometric $H\alpha$ Survey of the Southern Galactic Plane and Bulge (VPHAS+, www.vphas.eu).

References

- Albacete-Colombo, J. F., Damiani, F., Micela, G., Sciortino, S., & Harnden, F. R., Jr. 2008, *A&A*, 490, 1055
- Antokhin, I. I., Rauw, G., Vreux, J.-M., van der Hucht, K. A., & Brown, J. C. 2008, *A&A*, 477, 593
- Bagnulo, S., Jehin, E., Ledoux, C., Cabanac, R., Melo, C., Gilmozzi, R., & ESO Paranal Science Operations Team 2003, *The Messenger*, 114, 10
- Barbá, R. H., Gamen, R. C., Arias, J. I., et al. 2010, in *RMxAC*, Vol. 38, 30–32
- Bell, C. P. M., Naylor, T., Mayne, N. J., Jeffries, R. D., & Littlefair, S. P. 2013, *MNRAS*, 434, 806
- Bessell, M. S., Castelli, F., & Plez, B. 1998, *A&A*, 333, 231
- Broos, P. S., Townsley, L. K., Feigelson, E. D., et al. 2011a, *ApJS*, 194, 2
- Broos, P. S., Getman, K. V., Povich, M. S., et al. 2011b, *ApJS*, 194, 4
- Carraro, G., Romaniello, M., Ventura, P., & Patat, F. 2004, *A&A*, 418, 525
- Damiani, F., Micela, G., Sciortino, S., et al. 2006a, *A&A*, 460, 133
- Damiani, F., Prisinzano, L., Micela, G., & Sciortino, S. 2006b, *A&A*, 459, 477
- Damiani, F., Prisinzano, L., Micela, G., et al. 2014, *A&A*, 566, A50
- Damiani, F., Bonito, R., Magrini, L., et al. 2016, arXiv:1604.01208
- DeGioia-Eastwood, K., Throop, H., Walker, G., & Cudworth, K. M. 2001, *ApJ*, 549, 578
- Drew, J. E., Gonzalez-Solares, E., Greimel, R., et al. 2014, *MNRAS*, 440, 2036
- Ekström, S., Georgy, C., Eggenberger, P., et al. 2012, *A&A*, 537, A146
- Feigelson, E. D., Getman, K. V., Townsley, L. K., et al. 2011, *ApJS*, 194, 9
- Flaccomio, E., Damiani, F., Micela, G., et al. 2003, *ApJ*, 582, 398
- Frasca, A., Biazzo, K., Lanzafame, A. C., et al. 2015, *A&A*, 575, A4
- Gilmore, G., Randich, S., Asplund, M., et al. 2012, *The Messenger*, 147, 25
- Grigsby, J. A., Morrison, N. D., & Anderson, L. S. 1992, *ApJS*, 78, 205
- Herbst, W., Bailer-Jones, C. A. L., Mundt, R., Meisenheimer, K., & Wacker-mann, R. 2002, *A&A*, 396, 513
- Hur, H., Sung, H., & Bessell, M. S. 2012, *AJ*, 143, 41
- Kalari, V. M., Vink, J. S., Drew, J. E., et al. 2015, *MNRAS*, 453, 1026
- Kenyon, S. J., & Hartmann, L. 1995, *ApJS*, 101, 117
- Kos, J., & Zwitter, T. 2013, *ApJ*, 774, 72
- Jeffries, R. D. 2014, *EAS Publications Series*, 65, 289
- Lada, C. J., & Lada, E. A. 2003, *ARA&A*, 41, 57
- Lanz, T. & Hubeny, I. 2003, *ApJS*, 146, 417
- Lanzafame, A. C., Frasca, A., Damiani, F., et al. 2015, *A&A*, 576, A80
- Littlefair, S. P., Naylor, T., Mayne, N. J., Saunders, E., & Jeffries, R. D. 2011, *MNRAS*, 413, L56
- Maíz Apellániz, J. 2004, *PASP*, 116, 859
- Maíz Apellániz, J. 2005, *PASP*, 117, 615
- Maíz Apellániz, J. 2006, *AJ*, 131, 1184
- Maíz Apellániz, J. 2007, in *ASP Conf. Series*, Vol. 364, *The Future of Photometric, Spectrophotometric and Polarimetric Standardization*, ed. C. Sterken, 227
- Maíz Apellániz, J., Walborn, N. R., Galué, H. Á., & Wei, L. H. 2004, *ApJS*, 151, 103
- Maíz Apellániz, J., & Sota, A. 2008, in *Rev. Mex. Astron. Astrofís. (conference series)*, Vol. 33, 44–46
- Maíz Apellániz, J., Sota, A., Walborn, N. R., et al. 2011, in *Highlights of Spanish Astrophysics VI*, ed. M. R. Zapatero Osorio, J. Gorgas, J. Maíz Apellániz, J. R. Pardo, & A. Gil de Paz, 467–472
- Maíz Apellániz, J. 2013a, in *Highlights of Spanish Astrophysics VII*, 657–657
- Maíz Apellániz, J. 2013b, in *Highlights of Spanish Astrophysics VII*, 583–589
- Maíz Apellániz, J. 2015, *MmSAI*, 86, 553
- Maíz Apellániz, J., Evans, C. J., Barbá, R. H., et al. 2014, *A&A*, 564, A63
- Maíz Apellániz, J., Negueruela, I., Barbá, R. H., et al. 2015, *A&A*, 579, A108
- Mathieu, R. D. 1994, *ARA&A*, 32, 465
- Mathieu, R. D. 2004, *Stellar Rotation*, 215, 113
- Mayne, N. J., Naylor, T., Littlefair, S. P., Saunders, E. S., & Jeffries, R. D. 2007, *MNRAS*, 375, 1220
- McErlean, N. D., Lennon, D. J., & Dufton, P. L. 1999, *A&A*, 349, 553
- Morse, J. A., Davidson, K., Bally, J., et al. 1998, *AJ*, 116, 2443
- Negueruela, I., Maíz Apellániz, J., Simón-Díaz, S., et al. 2015, in *Highlights of Spanish Astrophysics VIII*, 524–529
- Niemela, V. S., Morrell, N. I., Fernández Lajús, E., et al. 2006, *MNRAS*, 367, 1450
- Povich, M. S., et al. 2011a, *ApJS*, 194, 6
- Povich, M. S., et al. 2011b, *ApJS*, 194, 14
- Preibisch, T., Kim, Y.-C., Favata, F., et al. 2005, *ApJS*, 160, 401
- Preibisch, T., Ratzka, T., Kuderna, B., et al. 2011, *A&A*, 530, A34
- Randich, S., Gilmore, G., & Gaia-ESO Consortium 2013, *The Messenger*, 154, 47
- Rebolledo, D., Burton, M., Green, A., et al. 2016, *MNRAS*, 456, 2406
- Rebull, L. M., Stauffer, J. R., Megeath, S. T., Hora, J. L., & Hartmann, L. 2006, *ApJ*, 646, 297
- Sanchawala, K., Chen, W.-P., Lee, H.-T., et al. 2007, *ApJ*, 656, 462
- Schmitt, J. H. M. M. 1997, *A&A*, 318, 215
- Siess, L., Dufour, E., & Forestini, M. 2000, *A&A*, 358, 593
- Sigut, T. A. A. 1996, *ApJ*, 473, 452
- Simón-Díaz, S., Castro, N., García, M., & Herrero, A. 2011, in *IAUS*, Vol. 272, 310–312
- Smith, R. G. 1987, *MNRAS*, 227, 943
- Smith, N. 2006, *ApJ*, 644, 1151
- Smith, N., Stassun, K. G., & Bally, J. 2005, *AJ*, 129, 888
- Smith, N., & Brooks, K. J. 2007, *MNRAS*, 379, 1279
- Smith, N., & Brooks, K. J. 2008, *Handbook of Star Forming Regions*, Volume II, 138
- Smith, N., Povich, M. S., Whitney, B. A., et al. 2010, *MNRAS*, 406, 952
- Sota, A., Maíz Apellániz, J., Morrell, N. I., et al. 2014, *ApJS*, 211, 10
- Spada, F., Lanzafame, A. C., Lanza, A. F., Messina, S., & Collier Cameron, A. 2011, *MNRAS*, 416, 447
- Stassun, K. G., Mathieu, R. D., Mazeh, T., & Vrba, F. J. 1999, *AJ*, 117, 2941
- Tapia, M., Roth, M., Vázquez, R. A., & Feinstein, A. 2003, *MNRAS*, 339, 44
- Townsley, L. K., Broos, P. S., Corcoran, M. F., et al. 2011, *ApJS*, 194, 1
- Vaidya, K., Chen, W.-P., & Lee, H.-T. 2015, *AJ*, 150, 195
- Walborn, N. R. 1973, *ApJ*, 179, 517
- Walborn, N. R. 1995, *Revista Mexicana de Astronomía y Astrofísica Conference Series*, 2, 51
- Wolff, S. C., Strom, S. E., & Hillenbrand, L. A. 2004, *ApJ*, 601, 979
- Wolk, S. J., Broos, P. S., Getman, K. V., et al. 2011, *ApJS*, 194, 12
- Wright, N. J., Drake, J. J., Guarcello, M. G., et al. 2014, arXiv:1408.6579
- Zeidler, P., Preibisch, T., Ratzka, T., Roccatagliata, V., & Petr-Gotzens, M. G. 2016, *A&A*, 585, A49

Table 1. Identifications for late-type Carina members. Column HSB2012 reports the identifier in Hur et al. (2012); column CXOGNC is the identifier in Broos et al. (2011a); column ADM2008 is the identifier in Albacete-Colombo et al. (2008); column YSO is the identifier in Zeidler et al. (2016). V magnitudes, $B - V$ and $V - I$ colors are from Hur et al. (2012).

HSB2012	CXOGNC	ADM2008	YSO	RA (J2000)	Dec (J2000)	V	$B - V$	$V - I$
796	10:43:31.96	-59:33:56.4	16.36	0.93	1.15
800	104332.23-593511.3	10:43:32.25	-59:35:11.5	16.20	0.80	1.11
908	104336.77-593315.2	10:43:36.77	-59:33:15.2	14.72	0.68	1.17
907	10:43:36.77	-59:36:48.2	17.12	1.10	1.19
954	104338.76-593301.9	10:43:38.80	-59:33:01.8	16.21	1.08	1.50
953	104338.81-593423.7	10:43:38.80	-59:34:23.8	18.19	...	2.33
995	104340.13-593356.0	...	104340.14-593356.3	10:43:40.13	-59:33:56.1	18.32	...	2.09
998	104340.19-593449.5	10:43:40.18	-59:34:49.6	17.04	1.55	2.13
1035	104341.45-593352.7	10:43:41.45	-59:33:52.8	13.33	0.73	1.14
1051	104341.97-593352.6	10:43:41.90	-59:33:53.0	17.86	...	1.86
1069	10:43:42.60	-59:32:52.6	18.20	...	2.17
1072	104342.69-593554.0	10:43:42.69	-59:35:54.1	18.32	...	1.99
1095	104343.50-593612.8	10:43:43.52	-59:36:13.2	17.59	1.22	1.79
1102	104343.88-593556.6	10:43:43.89	-59:35:56.4	18.30	...	1.94
1114	104344.33-593425.6	10:43:44.29	-59:34:25.7	13.97	0.97	1.43
1135	104344.84-593456.6	10:43:44.85	-59:34:56.7	17.24	1.51	2.13
1157	104345.81-592949.7	10:43:45.81	-59:29:49.7	15.31	0.99	1.39
1158	104345.85-593327.1	10:43:45.81	-59:33:26.8	17.07	1.52	1.96
1159	104345.86-593346.6	10:43:45.88	-59:33:46.7	15.97	1.05	1.44
1160	104345.91-593457.2	10:43:45.90	-59:34:57.3	17.63	1.46	1.84
1168	104346.01-593328.8	...	104346.01-593328.7	10:43:46.01	-59:33:28.7	15.60	1.45	1.89
1167	104346.05-593305.7	10:43:46.02	-59:33:05.5	16.00	0.79	1.14
1170	104346.16-593438.4	10:43:46.10	-59:34:38.4	18.33	0.49	1.63
1183	104346.44-593442.3	10:43:46.43	-59:34:42.4	12.47	0.56	1.02
1199	104346.87-593233.6	10:43:46.88	-59:32:33.8	17.93	1.72	2.02
1204	104346.97-593318.2	...	104346.98-593318.3	10:43:46.98	-59:33:18.2	16.73	1.48	1.99
1268	104348.78-593235.7	10:43:48.78	-59:32:35.7	17.74	1.56	1.85
1282	104349.07-593256.7	10:43:49.12	-59:32:56.8	17.54	1.40	1.91
1286	104349.17-593402.8	...	104349.20-593403.0	10:43:49.20	-59:34:02.9	18.48	...	2.41
1316	104350.07-593626.1	10:43:50.07	-59:36:26.2	17.55	1.42	2.15
1325	104350.42-593400.2	10:43:50.43	-59:34:00.5	17.81	1.53	1.92
1370	104351.81-593550.1	...	104351.86-593550.4	10:43:51.87	-59:35:50.3	18.24	...	2.02
1389	104352.31-593922.2	...	104352.30-593922.3	10:43:52.30	-59:39:22.3	17.48	1.52	2.33
1405	104352.88-593301.7	10:43:52.87	-59:33:01.8	16.17	...	2.05
1429	10:43:53.50	-59:32:01.2	17.40	1.52	1.78
1455	104354.36-593303.0	10:43:54.37	-59:33:02.9	14.28	...	1.57
1470	104354.87-593129.3	10:43:54.89	-59:31:29.4	16.49	1.50	1.82
1477	104355.13-593330.3	10:43:55.10	-59:33:30.5	16.56	1.15	1.84
1483	104355.19-593228.2	10:43:55.33	-59:32:27.9	18.16	...	2.10
1493	104355.71-593627.1	10:43:55.71	-59:36:27.4	17.95	1.28	2.02
1501	10:43:55.94	-59:32:10.0	17.28	1.27	1.80
1503	104355.99-594418.5	10:43:55.99	-59:44:18.6	17.87	1.38	2.06
1511	104356.20-593532.6	10:43:56.20	-59:35:32.6	18.10	...	1.96
1528	104356.67-593021.9	10:43:56.68	-59:30:21.8	13.81	1.01	1.09
1531	104356.68-593147.3	10:43:56.74	-59:31:47.5	16.74	1.60	2.02
1539	104356.94-593217.7	10:43:56.90	-59:32:17.6	17.97	1.43	1.87
1553	104357.43-593232.2	10:43:57.40	-59:32:32.3	17.04	...	1.58
1569	104357.72-593324.1	10:43:57.76	-59:33:23.9	14.06	0.84	1.19
1580	104358.04-593717.4	...	104358.04-593717.9	10:43:58.04	-59:37:18.0	17.60	1.57	2.08
1620	10:43:59.27	-59:43:36.3	18.26	...	2.55
1627	104359.52-593435.0	10:43:59.53	-59:34:35.0	17.36	1.33	1.84
1646	104359.99-593012.9	...	104400.01-593013.0	10:44:00.01	-59:30:13.0	17.37	1.28	1.87
1661	10:44:00.67	-59:34:17.4	15.05	1.10	1.50
1665	104400.81-593439.1	...	104400.81-593439.1	10:44:00.82	-59:34:39.1	16.63	1.52	1.98
1668	104400.91-593351.1	10:44:00.91	-59:33:51.3	17.61	1.63	2.19
1676	104401.10-593535.1	...	104401.12-593535.3	10:44:01.12	-59:35:35.3	14.98	0.66	1.13
1686	104401.59-593235.0	10:44:01.59	-59:32:34.9	16.34	1.42	1.76
1690	104401.71-593249.4	...	104401.73-593249.5	10:44:01.70	-59:32:49.4	17.33	2.01	2.11

Table 1. continued.

HSB2012	CXOGNC	ADM2008	YSO	RA (J2000)	Dec (J2000)	V	B - V	V - I
1689	104401.69-593101.6	10:44:01.74	-59:31:01.6	15.55	1.18	1.49
1693	104401.73-593008.1	...	104401.79-593008.0	10:44:01.80	-59:30:08.0	17.03	1.21	1.65
1699	104402.09-593751.2	41	104402.09-593752.3	10:44:02.09	-59:37:52.3	14.84	1.07	1.50
1725	104403.00-593354.6	10:44:03.01	-59:33:54.5	15.73	1.23	1.56
1734	104403.37-593137.2	10:44:03.40	-59:31:37.2	16.01	1.44	1.72
1772	104404.77-593524.7	10:44:04.83	-59:35:24.4	16.59	0.90	1.20
1783	104405.18-593232.1	10:44:05.19	-59:32:32.1	17.28	1.44	1.92
1784	104405.19-593413.8	10:44:05.21	-59:34:14.0	16.89	1.23	1.66
1805	104406.22-593131.0	10:44:06.24	-59:31:30.9	17.77	1.65	1.93
1816	104406.70-593148.3	10:44:06.71	-59:31:48.2	17.97	...	2.43
1822	104406.77-593234.6	10:44:06.77	-59:32:34.7	17.88	1.93	2.22
1828	104406.83-592941.0	10:44:06.85	-59:29:41.0	17.26	1.77	2.09
1832	10:44:07.01	-59:32:31.0	17.71	1.88	2.01
1834	104407.08-593110.8	...	104407.11-593110.8	10:44:07.11	-59:31:10.8	18.03	1.35	2.13
1848	10:44:07.77	-59:46:28.7	16.99	0.76	1.29
1859	104408.18-593246.6	10:44:08.18	-59:32:46.5	16.66	1.42	1.71
1874	104408.71-593610.2	63	...	10:44:08.71	-59:36:10.5	15.58	1.09	1.41
1885	104408.95-593132.2	10:44:08.97	-59:31:32.2	13.81	0.84	1.13
1904	104409.43-593425.1	10:44:09.40	-59:34:25.3	15.69	...	1.39
1916	104409.85-593204.1	10:44:09.87	-59:32:04.2	18.06	1.53	2.05
1933	104410.20-593741.3	10:44:10.19	-59:37:41.5	18.41	...	2.18
1935	104410.19-593554.6	10:44:10.20	-59:35:54.5	18.33	...	1.84
1938	104410.28-593000.9	10:44:10.31	-59:30:01.1	17.70	1.24	1.67
1954	104410.83-593221.4	10:44:10.87	-59:32:21.3	18.05	1.76	1.99
1962	104411.10-594048.6	10:44:11.10	-59:40:48.7	17.75	1.26	1.93
1992	104412.27-593424.6	...	104412.28-593424.8	10:44:12.26	-59:34:24.6	17.34	1.25	1.84
1999	104412.44-593544.5	...	104412.52-593544.9	10:44:12.52	-59:35:45.0	18.44	...	2.32
2002	104412.59-593412.6	10:44:12.55	-59:34:12.4	14.59	0.52	0.71
2007	10:44:12.84	-59:39:37.2	14.03	1.00	1.33
2016	104413.03-593321.9	10:44:13.05	-59:33:21.9	18.18	1.65	2.00
2036	104413.83-594224.5	92	...	10:44:13.86	-59:42:24.9	17.73	1.21	1.82
2037	104413.91-594129.0	93	...	10:44:13.90	-59:41:29.3	17.55	1.39	1.92
2057	104414.86-593525.6	10:44:14.88	-59:35:25.4	18.16	1.31	1.78
2062	104414.96-593050.6	10:44:14.99	-59:30:50.5	18.43	...	1.94
2105	104416.31-593314.6	...	104416.36-593314.9	10:44:16.37	-59:33:14.9	17.76	1.37	1.86
2124	104417.10-593101.8	...	104417.12-593102.0	10:44:17.11	-59:31:01.9	17.05	1.17	1.60
2123	104417.12-594156.7	105	...	10:44:17.12	-59:41:56.8	17.49	1.95	2.10
2142	104417.69-594236.0	110	...	10:44:17.71	-59:42:36.0	18.27	...	1.87
2145	104417.80-594220.7	10:44:17.84	-59:42:21.2	18.17	...	2.10
2148	104417.84-594356.3	111	...	10:44:17.95	-59:43:57.0	18.41	0.89	1.87
2157	10:44:18.27	-59:31:06.7	18.41	1.58	2.01
2184	104419.19-593151.2	10:44:19.21	-59:31:51.0	18.28	...	2.15
2195	104419.52-594351.6	115	...	10:44:19.51	-59:43:51.9	18.37	1.46	2.02
2207	104420.13-594339.6	119	...	10:44:20.14	-59:43:39.6	18.36	0.99	1.86
2208	104420.17-594229.7	121	...	10:44:20.16	-59:42:29.7	17.45	1.35	1.85
2210	104420.00-593825.6	120	...	10:44:20.19	-59:38:26.5	18.35	...	1.89
2230	104421.05-594419.9	126	...	10:44:21.05	-59:44:19.9	17.74	1.10	1.65
2288	104423.32-593001.4	...	104423.32-593001.6	10:44:23.31	-59:30:01.5	17.39	1.46	1.91
2290	10:44:23.40	-59:35:56.2	18.50	1.16	1.54
2300	104423.67-594114.6	147	...	10:44:23.62	-59:41:15.1	16.94	1.35	1.73
2299	104423.63-593153.5	10:44:23.65	-59:31:53.4	15.85	1.27	1.56
2305	104424.04-594055.8	151	...	10:44:24.05	-59:40:55.9	16.54	1.18	1.52
2331	104424.79-593959.2	155	...	10:44:24.83	-59:39:59.6	18.35	...	2.11
2335	104424.90-593702.6	156	...	10:44:24.89	-59:37:02.6	17.48	1.55	1.88
2337	104424.96-593647.8	157	...	10:44:24.98	-59:36:47.8	17.91	1.60	1.81
2348	104425.38-594354.9	160	...	10:44:25.40	-59:43:54.9	17.94	1.15	1.76
2359	104425.71-594353.3	164	...	10:44:25.65	-59:43:53.5	17.80	1.38	1.92
2363	104425.77-593354.6	10:44:25.82	-59:33:54.1	18.37	1.40	1.84
2371	104426.28-594241.1	170	...	10:44:26.29	-59:42:41.2	17.43	1.25	1.77
2381	104426.57-593250.9	10:44:26.61	-59:32:50.7	17.90	1.84	2.03

Table 1. continued.

HSB2012	CXOGNC	ADM2008	YSO	RA (J2000)	Dec (J2000)	V	B - V	V - I
2399	10:44:27.30	-59:44:32.3	18.18	1.64	1.82
2405	104427.50-593353.9	10:44:27.46	-59:33:53.9	17.88	1.30	1.75
2421	104428.09-593308.6	10:44:28.10	-59:33:08.7	15.33	1.34	1.60
2433	104428.34-594123.7	182	...	10:44:28.35	-59:41:23.8	16.28	1.18	1.52
2439	104428.49-594145.0	184	104428.48-594145.1	10:44:28.47	-59:41:45.1	17.01	1.34	1.64
2460	104429.08-594143.1	191	...	10:44:29.08	-59:41:43.2	15.27	1.09	1.44
2477	104429.75-594332.7	200	...	10:44:29.77	-59:43:32.7	17.50	1.51	1.84
2479	104429.78-593413.4	10:44:29.80	-59:34:13.3	17.06	1.43	1.71
2482	104429.89-593317.0	...	104429.90-593317.2	10:44:29.90	-59:33:17.0	18.08	1.70	2.12
2495	104430.30-593402.6	10:44:30.30	-59:34:02.5	15.77	1.11	1.41
2504	10:44:30.50	-59:37:47.7	17.38	0.86	1.54
2506	104430.56-593924.9	209	...	10:44:30.55	-59:39:24.7	13.46	0.66	1.02
2513	104430.84-592948.4	10:44:30.84	-59:29:48.1	17.59	1.40	1.81
2517	104431.01-594205.2	213	...	10:44:31.01	-59:42:05.2	18.27	...	1.92
2519	104431.13-594305.0	215	...	10:44:31.10	-59:43:04.9	18.21	...	1.93
2531	104431.86-593841.0	223	...	10:44:31.86	-59:38:41.6	17.93	...	1.84
2540	104432.25-593110.8	10:44:32.27	-59:31:10.8	16.14	1.24	1.57
2551	104432.54-594351.6	231	...	10:44:32.54	-59:43:51.7	16.81	1.20	1.55
2553	104432.56-594406.6	230	...	10:44:32.56	-59:44:06.7	13.64	0.60	0.91
2554	104432.58-593303.5	10:44:32.57	-59:33:03.3	14.18	0.40	0.68
2555	104432.63-593225.9	10:44:32.67	-59:32:25.5	18.15	1.33	1.81
2565	104433.12-594002.0	237	...	10:44:33.10	-59:40:02.2	18.04	...	2.07
2569	104433.15-593356.2	10:44:33.19	-59:33:55.6	17.93	...	1.91
2568	10:44:33.20	-59:36:43.0	17.99	1.50	2.18
2570	104433.23-593348.4	...	104433.21-593349.0	10:44:33.21	-59:33:49.0	17.48	1.72	2.19
2584	104433.97-593733.9	245	...	10:44:33.96	-59:37:34.0	17.79	1.64	2.00
2585	104434.01-594354.8	249	104434.02-594355.1	10:44:34.03	-59:43:55.3	16.50	1.14	1.78
2597	10:44:34.69	-59:33:30.7	18.03	1.79	2.13
2598	104434.80-593526.6	...	104434.80-593526.3	10:44:34.80	-59:35:26.3	15.86	1.49	1.90
2602	104434.94-594405.8	251	104434.93-594405.8	10:44:34.92	-59:44:06.0	17.43	...	1.84
2606	104434.99-594142.4	252	...	10:44:35.00	-59:41:42.4	18.48	...	2.04
2609	10:44:35.11	-59:40:04.6	18.22	...	2.60
2618	104435.54-594350.9	260	...	10:44:35.53	-59:43:51.0	17.40	1.60	1.87
2624	104435.87-594446.9	266	...	10:44:35.86	-59:44:47.0	17.28	1.26	1.59
2636	104436.33-594411.0	271	...	10:44:36.33	-59:44:11.1	17.34	1.35	1.74
2635	104436.39-593944.4	272	...	10:44:36.35	-59:39:44.3	18.19	0.82	2.02
2643	104436.68-594622.0	278	104436.66-594621.8	10:44:36.66	-59:46:21.8	17.78	1.36	1.93
2669	104437.81-594331.0	297	...	10:44:37.82	-59:43:31.0	18.45	0.98	1.82
2674	104438.08-594434.8	301	104438.08-594434.9	10:44:38.08	-59:44:35.0	16.64	1.33	1.72
2675	104438.10-594131.3	304	...	10:44:38.09	-59:41:31.4	17.29	1.46	1.90
2677	104438.17-594311.2	307	104438.16-594311.3	10:44:38.17	-59:43:11.4	16.52	1.48	1.82
2680	104438.22-594333.7	308	...	10:44:38.22	-59:43:34.0	18.02	1.40	1.88
2692	104438.66-593007.8	10:44:38.64	-59:30:07.6	18.29	0.97	1.80
2708	10:44:39.15	-59:29:58.7	15.94	0.96	1.24
2726	104439.91-594358.1	325	...	10:44:39.90	-59:43:58.3	16.17	1.15	1.50
2755	104440.91-594524.7	334	...	10:44:40.87	-59:45:24.7	14.43	0.62	0.71
2760	104441.11-594422.9	339	104441.08-594422.9	10:44:41.09	-59:44:22.9	18.34	1.30	1.98
2761	104441.17-593819.4	342	...	10:44:41.14	-59:38:19.5	16.60	1.34	1.81
2763	104441.32-594408.6	345	...	10:44:41.31	-59:44:08.8	17.04	1.18	1.68
2769	104441.43-593841.5	10:44:41.60	-59:38:41.7	18.35	...	2.02
2774	104441.76-594047.7	351	...	10:44:41.76	-59:40:47.8	16.20	1.29	1.74
2779	104441.98-594215.8	354	...	10:44:41.97	-59:42:16.0	16.95	1.18	1.58
2782	104442.16-594243.1	357	...	10:44:42.16	-59:42:43.2	18.36	...	2.00
2812	104443.54-594718.1	376	...	10:44:43.54	-59:47:17.9	17.02	1.42	1.85
2818	104443.94-593955.7	379	...	10:44:43.95	-59:39:55.7	17.94	...	1.89
2833	104444.63-593154.8	10:44:44.61	-59:31:55.1	17.24	1.50	1.79
2846	104445.30-593919.1	392	...	10:44:45.28	-59:39:19.3	15.78	1.15	1.71
2866	104446.20-594449.2	400	...	10:44:46.21	-59:44:49.4	17.56	1.23	1.77
2872	104446.53-593413.3	10:44:46.50	-59:34:13.4	13.22	0.44	0.76
2887	104447.43-593508.3	408	...	10:44:47.43	-59:35:08.1	17.52	1.32	2.43

Table 1. continued.

HSB2012	CXOGNC	ADM2008	YSO	RA (J2000)	Dec (J2000)	V	B - V	V - I
2890	104447.62-594326.0	10:44:47.58	-59:43:26.0	15.18	0.99	1.31
2898	104447.78-594606.7	413	104447.77-594606.7	10:44:47.78	-59:46:06.7	17.69	1.44	1.98
2902	104447.97-594309.2	416	...	10:44:47.97	-59:43:09.5	17.93	1.37	1.78
2908	104448.39-593143.6	10:44:48.38	-59:31:43.6	16.21	1.11	1.45
2909	104448.37-594113.9	417	...	10:44:48.40	-59:41:14.0	16.06	1.51	2.12
2923	104448.97-594343.6	419	104448.98-594343.5	10:44:48.99	-59:43:43.5	16.73	1.43	1.88
2926	104449.00-594044.8	420	...	10:44:49.03	-59:40:44.6	16.44	1.65	2.19
2946	104449.66-594503.3	429	...	10:44:49.69	-59:45:03.3	17.94	1.11	1.70
2947	104449.75-594208.1	431	104449.75-594208.3	10:44:49.76	-59:42:08.1	17.88	1.46	2.10
2949	104449.77-594727.4	432	104449.78-594727.3	10:44:49.79	-59:47:27.3	18.02	1.82	2.28
2948	...	434	...	10:44:49.81	-59:43:57.5	17.50	1.19	1.59
2950	104449.84-593211.3	10:44:49.82	-59:32:11.4	15.45	1.03	1.33
2966	104450.13-594523.6	441	104450.13-594523.6	10:44:50.12	-59:45:23.6	17.68	1.31	1.75
2967	104450.12-594738.7	440	...	10:44:50.14	-59:47:38.7	17.44	1.51	1.93
2970	104450.34-594017.4	446	...	10:44:50.37	-59:40:17.4	17.14	...	2.04
2972	104450.44-594540.9	447	...	10:44:50.43	-59:45:40.8	15.32	1.13	1.46
2985	104450.78-593410.3	...	104450.82-593410.2	10:44:50.82	-59:34:10.2	18.50	...	2.15
2987	104450.90-594435.4	451	104450.91-594435.5	10:44:50.91	-59:44:35.7	17.86	1.37	1.93
3019	104452.18-594515.1	467	104452.16-594515.2	10:44:52.12	-59:45:15.4	18.15	...	2.25
3021	104452.23-594155.1	468	...	10:44:52.24	-59:41:55.2	15.77	1.17	1.52
3032	104452.51-594159.9	470	...	10:44:52.53	-59:42:00.1	16.36	1.42	1.91
3041	104452.76-594319.0	473	...	10:44:52.75	-59:43:19.0	17.51	1.45	1.91
3044	10:44:52.85	-59:33:04.5	16.91	0.91	1.33
3051	104453.39-594353.0	479	...	10:44:53.40	-59:43:53.2	18.18	1.46	1.94
3065	104453.70-593309.1	10:44:53.68	-59:33:09.2	16.49	1.04	1.30
3067	104453.71-594324.1	482	...	10:44:53.72	-59:43:24.5	16.13	1.14	1.70
3073	104453.87-594314.0	485	...	10:44:53.86	-59:43:14.1	15.82	1.08	1.43
3089	10:44:54.38	-59:40:00.5	14.19	0.48	0.77
3094	104454.48-594243.1	497	...	10:44:54.49	-59:42:43.2	17.96	1.37	2.05
3102	104454.76-593600.1	501	...	10:44:54.76	-59:36:00.6	17.39	1.09	1.37
3104	104454.82-594351.6	503	...	10:44:54.83	-59:43:51.7	16.95	1.31	1.73
3112	104455.10-594824.4	507	...	10:44:55.07	-59:48:24.4	18.13	1.58	2.26
3116	104455.27-594648.5	509	...	10:44:55.27	-59:46:48.7	18.21	1.22	1.70
3120	104455.42-594453.4	513	...	10:44:55.43	-59:44:53.5	17.19	1.61	2.11
3134	104456.11-593657.3	10:44:56.08	-59:36:57.6	15.73	1.05	1.38
3136	104456.14-594538.1	521	...	10:44:56.14	-59:45:38.1	17.64	1.40	1.83
3158	10:44:56.90	-59:39:46.2	16.55	1.40	1.44
3161	104456.87-594145.3	531	...	10:44:56.90	-59:41:45.3	18.10	...	2.15
3198	104458.02-594224.4	553	104458.03-594224.4	10:44:58.00	-59:42:24.5	17.04	1.53	1.94
3196	104458.02-594709.4	552	...	10:44:58.00	-59:47:09.6	16.85	1.37	1.91
3200	104458.07-594628.1	554	...	10:44:58.10	-59:46:28.3	16.70	1.34	1.75
3217	104458.59-594246.0	562	104458.60-594246.1	10:44:58.62	-59:42:46.1	18.45	...	2.11
3219	104458.62-594039.0	563	...	10:44:58.70	-59:40:39.1	16.92	1.21	1.62
3244	104459.72-593406.9	...	104459.54-593407.3	10:44:59.53	-59:34:07.3	18.11	1.54	2.16
3271	104500.47-593937.5	589	...	10:45:00.50	-59:39:37.5	17.32	1.31	1.81
3287	104501.04-593235.5	10:45:00.97	-59:32:36.3	15.94	0.90	1.00
3294	104501.07-593917.6	603	...	10:45:01.12	-59:39:17.7	17.37	1.39	1.79
3319	104501.98-594023.7	620	...	10:45:02.00	-59:40:23.8	16.22	1.36	1.73
3326	104502.25-594536.4	631	...	10:45:02.26	-59:45:36.4	18.40	...	2.15
3338	104502.90-594225.8	638	...	10:45:02.90	-59:42:26.0	18.07	1.69	2.16
3358	104503.62-594320.8	650	...	10:45:03.60	-59:43:20.9	16.39	1.23	1.52
3359	104503.67-594348.4	651	...	10:45:03.70	-59:43:48.6	18.33	...	2.05
3367	104503.91-593819.8	656	...	10:45:03.90	-59:38:20.1	16.42	1.17	1.77
3374	104504.23-594010.9	658	...	10:45:04.20	-59:40:10.9	16.67	...	1.62
3395	104505.07-593733.5	670	...	10:45:05.07	-59:37:33.6	15.77	1.13	1.47
3399	104505.11-593345.7	10:45:05.18	-59:33:45.8	16.65	1.37	1.82
3409	104505.43-594358.6	679	...	10:45:05.40	-59:43:58.8	18.13	1.27	1.76
3412	104505.59-594530.7	680	...	10:45:05.60	-59:45:30.7	17.50	...	1.91
3415	104505.70-594343.7	682	...	10:45:05.71	-59:43:43.6	15.18	1.32	1.68
3425	104505.91-594023.9	691	...	10:45:05.90	-59:40:24.2	17.25	...	1.50

Table 1. continued.

HSB2012	CXOGNC	ADM2008	YSO	RA (J2000)	Dec (J2000)	V	B - V	V - I
3427	104505.97-594341.1	692	...	10:45:05.93	-59:43:41.4	16.18	1.55	1.90
3435	10:45:06.15	-59:37:34.4	17.69	1.38	1.79
3438	104506.22-593940.1	698	...	10:45:06.20	-59:39:40.4	17.56	1.29	1.72
3443	10:45:06.28	-59:37:41.6	18.24	...	1.98
3442	10:45:06.30	-59:41:18.2	15.66	0.85	0.97
3454	104506.80-594446.2	709	...	10:45:06.81	-59:44:46.1	15.53	1.11	1.52
3480	104507.78-594026.3	721	...	10:45:07.80	-59:40:26.4	18.23	...	1.86
3485	104507.96-593725.3	726	...	10:45:07.95	-59:37:25.3	18.21	...	2.02
3488	...	727	...	10:45:08.20	-59:40:06.0	17.87	...	1.80
3505	104508.59-594017.0	734	...	10:45:08.60	-59:40:17.2	15.62	1.15	1.44
3508	104508.63-594134.5	736	...	10:45:08.70	-59:41:34.7	16.60	1.44	1.80
3524	104509.20-593851.6	748	...	10:45:09.23	-59:38:52.0	18.30	1.11	2.07
3531	104509.56-594043.5	753	...	10:45:09.60	-59:40:43.3	16.30	1.11	1.44
3541	10:45:09.70	-59:40:23.3	18.45	...	1.79
3536	104509.71-594245.6	756	...	10:45:09.72	-59:42:45.5	16.67	1.20	1.75
3549	104509.92-594121.4	760	...	10:45:09.90	-59:41:21.3	18.29	...	1.93
3554	104510.12-594352.9	763	...	10:45:10.08	-59:43:53.4	18.19	1.21	2.04
3557	104510.26-594229.6	767	...	10:45:10.30	-59:42:29.9	17.96	1.63	1.99
3558	104510.34-594028.8	769	...	10:45:10.40	-59:40:28.9	16.88	1.34	1.56
3578	104511.06-594457.2	786	...	10:45:11.08	-59:44:57.2	17.12	...	1.76
3577	104511.09-594533.5	787	104511.08-594533.5	10:45:11.08	-59:45:33.5	17.89	1.55	2.12
3617	104512.89-594504.4	814	...	10:45:12.84	-59:45:04.0	16.27	...	1.69
3628	104513.29-593521.0	816	...	10:45:13.28	-59:35:21.2	17.98	1.58	2.08
3633	104513.36-594005.7	819	...	10:45:13.40	-59:40:06.0	18.10	...	1.89
3636	104513.55-594404.3	822	...	10:45:13.55	-59:44:04.3	17.58	1.56	2.06
3644	10:45:13.68	-59:39:56.7	17.70	1.37	1.58
3650	104514.08-594315.5	830	...	10:45:14.06	-59:43:15.5	17.97	1.54	1.97
3660	104514.51-594246.9	834	...	10:45:14.52	-59:42:47.1	17.85	1.56	2.16
3668	104514.90-594441.6	839	...	10:45:14.90	-59:44:41.6	18.23	...	1.81
3683	10:45:15.29	-59:37:53.7	16.25	2.23	3.22
3692	104515.50-594012.8	845	...	10:45:15.51	-59:40:12.9	17.04	1.41	1.65
3716	104516.52-594214.9	853	...	10:45:16.60	-59:42:14.9	18.21	1.56	2.11
3722	104516.74-594007.7	857	...	10:45:16.76	-59:40:08.0	17.95	...	1.82
3732	10:45:17.26	-59:31:11.9	18.32	1.66	2.12
3749	104517.86-593709.9	871	...	10:45:17.89	-59:37:09.6	18.06	1.43	2.05
3808	104520.16-593919.3	886	...	10:45:20.14	-59:39:19.6	18.31	1.34	1.85
3830	104520.84-594012.7	892	...	10:45:20.88	-59:40:13.0	14.59	0.97	1.29
3834	104520.95-594548.7	894	...	10:45:20.97	-59:45:48.9	17.37	1.57	2.34
3846	104521.32-593546.3	10:45:21.27	-59:35:46.4	18.13	1.29	1.74
3847	104521.36-594134.4	896	104521.36-594134.6	10:45:21.36	-59:41:34.6	18.02	1.47	2.07
3849	10:45:21.40	-59:39:28.5	18.27	1.34	1.93
3860	104521.73-594302.5	10:45:21.73	-59:43:02.4	17.07	1.05	1.44
3873	104521.99-594052.6	903	104522.00-594052.7	10:45:22.00	-59:40:52.7	17.07	1.88	2.05
3875	104522.05-594145.7	905	...	10:45:22.06	-59:41:45.8	15.77	1.27	1.64
3879	104522.11-593755.0	906	...	10:45:22.14	-59:37:55.4	17.51	1.55	1.86
3909	104523.55-593914.0	913	...	10:45:23.56	-59:39:14.1	14.51	0.53	0.70
3916	104523.69-594144.6	916	...	10:45:23.70	-59:41:44.6	18.24	1.54	2.10
3954	10:45:24.83	-59:41:26.0	17.20	1.46	1.75
3956	10:45:24.97	-59:42:45.4	17.83	1.42	1.89
3970	104525.58-594350.9	928	...	10:45:25.58	-59:43:50.9	16.67	1.36	1.86
4049	104528.89-594347.9	958	...	10:45:28.87	-59:43:47.9	18.18	1.60	2.28
4187	104535.42-594544.9	987	...	10:45:35.42	-59:45:44.8	17.27	1.09	2.08
4218	104536.96-593320.4	10:45:36.94	-59:33:20.5	15.98	1.15	1.32
4244	104538.35-594207.5	1002	...	10:45:38.34	-59:42:07.9	13.55	0.60	1.16
4274	10:45:39.70	-59:40:08.2	18.45	...	3.07
4282	104540.44-594830.6	1009	104540.30-594829.7	10:45:40.30	-59:48:29.7	16.43	1.52	2.38
4338	104543.71-594147.7	1020	104543.66-594148.1	10:45:43.67	-59:41:48.2	17.99	...	2.62
4366	104544.68-594134.1	10:45:44.94	-59:41:34.6	14.15	0.52	0.64
4392	104546.27-594637.4	1027	...	10:45:46.07	-59:46:38.5	13.92	0.47	0.57
4415	104547.10-593419.8	10:45:47.09	-59:34:19.9	17.52	1.26	1.65

Table 2. Parameters of late-type Carina members. Column HSB2012 reports the identifier in Hur et al. (2012). SNR is the spectrum median signal/noise ratio. RV is the heliocentric radial velocity. Errors on T_{eff} are statistical only. The gravity index γ is defined in Damiani et al. (2014). Column “log age” is the photometric age. Column $H\alpha$ reports “Y” if an excess $H\alpha$ emission is detected, either from accretion (CTTS) or chromospheric, distinct from the nebular $H\alpha$ emission. Column “SB2” is “Y” for SB2 binaries.

HSB2012	SNR	RV (km/s)	$v \sin i$ (km/s)	T_{eff} (K)	A_V	Li EW (mÅ)	γ	log age (yr)	$H\alpha$	SB2
796	17.0	2.5± 2.5	20.3± 3.3	5694± 218	0.75	137.8±12.0	1.01±0.015	...	Y	N
800	43.1	-0.7± 6.2	74.2± 8.1	5978± 95	0.81	105.3± 6.4	1.009±0.006	...	Y	N
908	62.5	-11.5± 7.4	30.0±12.7	7541± 92	1.77	89.7± 3.9	0.999±0.004	...	N	N
907	28.5	-4.9± 0.6	13.6± 1.7	4869± 95	0.31	202.0± 6.6	0.969±0.009	6.98	N	N
954	49.6	-6.5± 8.0	69.0± 2.7	5727± 67	1.52	160.3± 6.3	1.01±0.005	...	N	N
953	25.9	-3.6± 1.4	24.8± 1.5	4865± 104	2.78	371.0± 8.3	1.022± 0.01	6.30	N	N
995	16.6	-6.8± 2.0	13.0± 1.6	5019± 172	2.44	373.8±11.0	0.999±0.016	...	Y	N
998	47.0	-9.3± 7.0	92.4± 1.4	4942± 60	2.44	349.6± 7.4	1.011±0.006	6.12	Y	N
1035	130.4	-0.7±15.1	99.4± 9.6	7498± 43	1.67	38.6± 2.3	0.998±0.002	...	N	N
1051	18.2	-5.2± 2.0	15.0± 0.5	5177± 159	2.04	371.1± 7.9	1.028±0.015	6.89	Y	N
1069	21.1	-4.2± 1.3	15.0± 0.5	4453± 101	1.86	435.1± 8.6	0.995±0.012	...	Y	N
1072	17.8	-0.5± 8.2	63.0± 0.5	4676± 125	1.80	396.3±18.0	0.982±0.015	6.62	Y	N
1095	30.2	-29.5±17.5	87.7± 9.3	6099± 126	2.39	395.3±16.0	1.03±0.009	...	N	N
1102	18.6	-11.3± 2.0	24.0± 0.5	5601± 206	2.46	388.3±11.0	1.004±0.014	...	N	N
1114	102.1	15.7±12.1	185.3± 2.6	6158± 45	1.61	...± ...	1.009±0.003	...	Y	N
1135	38.2	-2.3± 1.3	33.7± 1.5	4639± 68	2.07	418.0± 7.7	1.007±0.007	5.95	Y	N
1157	35.7	-6.6± 3.5	30.0± 0.5	5833± 114	1.33	175.7± 6.9	0.998±0.007	...	Y	N
1158	37.1	-48.0±31.4	145.3± 7.5	4888± 68	1.98	407.7±12.0	1.015±0.007	6.22	Y	N
1159	53.2	-15.7±25.3	132.0±20.5	6392± 89	1.81	...± ...	1.009±0.005	...	N	N
1160	29.5	-8.7± 1.7	30.0± 0.5	5299± 114	2.09	293.4± 8.0	1.006±0.009	6.88	N	N
1168	83.1	-18.6±29.6	171.3± 3.2	6099± 49	2.62	201.8± 6.4	1.012±0.003	...	Y	N
1167	45.5	-20.1±32.9	20.8±10.0	7659± 126	1.76	...± ...	0.992±0.006	...	N	N
1170	15.3	-5.2± 3.1	24.0± 0.5	4652± 142	0.97	470.0±14.0	0.971±0.017	...	Y	N
1183	163.0	...± ...	63.4±10.0	... ±	27.6± 1.9	1.001±0.002	...	Y	N
1199	21.1	-31.6± 9.8	89.4±14.1	4838± 116	2.05	524.7±19.0	1.037±0.012	6.46	N	N
1204	35.4	-8.3± 2.0	27.0± 0.5	5092± 84	2.26	363.3± 5.8	1.011±0.007	6.24	Y	N
1268	20.2	-5.9± 1.2	28.1± 2.3	4798± 124	1.62	423.2±10.0	1.021±0.013	6.55	Y	N
1282	28.2	-4.9± 2.7	37.9± 1.6	4808± 99	1.78	427.4± 8.7	1.02±0.009	6.37	N	N
1286	17.2	-7.3± 1.6	24.0± 0.5	4858± 152	2.96	481.8±12.0	1.002±0.015	6.33	Y	N
1316	28.3	-7.4± 1.9	21.0± 0.5	5227± 118	2.73	412.2± 7.2	1.006±0.009	...	N	N
1325	36.0	-4.7± 1.9	33.0± 0.5	5081± 84	2.10	302.2± 7.5	1.017±0.007	6.69	Y	N
1370	20.2	-8.7± 1.1	18.0± 0.5	5243± 151	2.44	319.3± 9.6	0.99±0.013	6.93	Y	N
1389	46.7	-9.5± 1.1	24.0± 0.5	5126± 68	3.06	354.1± 6.3	1.01±0.006	6.25	Y	N
1405	53.2	-4.3± 1.8	38.6± 2.6	4621± 48	1.85	409.2± 5.0	1.01±0.005	5.63	Y	N
1429	27.9	-7.3± 5.0	54.4± 1.2	4884± 95	1.58	338.8± 8.7	1.009±0.009	6.50	N	N
1455	45.5	-4.3± 3.8	41.5± 3.0	5785± 85	1.72	184.3± 6.2	1.011±0.006	5.95	N	N
1470	49.6	-7.4± 1.9	40.1± 1.6	4998± 61	1.82	346.7± 5.4	1.008±0.005	6.23	N	N
1477	46.3	-5.3± 1.0	15.0± 0.5	4994± 66	1.85	370.4± 4.8	1.009±0.006	6.24	Y	N
1483	18.6	-6.6± 3.4	33.0± 0.5	4773± 126	2.16	523.6±12.0	0.98±0.014	6.45	Y	N
1493	24.6	-8.1± 1.8	27.0± 0.5	4906± 116	2.14	449.6± 8.6	1.004±0.011	6.53	N	N
1501	31.8	-11.2± 5.4	80.0± 1.8	4813± 87	1.52	432.4±10.0	1.015±0.008	6.38	N	N
1503	32.3	-3.0± 6.7	70.3± 5.5	6643± 141	3.38	...± ...	1.007±0.008	...	Y	N
1511	21.2	-3.5± 6.6	47.0± 1.6	5747± 170	2.58	285.7±11.0	1.022±0.012	...	N	N
1528	121.5	-20.4± 0.2	11.3± 1.4	5708± 32	0.65	...± ...	1.006±0.002	6.26	N	N
1531	41.3	-15.0± 4.8	77.3± 4.5	4478± 59	1.56	387.7± 7.4	0.995±0.006	5.70	Y	N
1539	20.0	-4.6± 4.2	48.0± 0.5	4610± 128	1.44	419.5±12.0	0.996±0.013	6.55	N	N
1553	26.6	-2.5±17.8	116.1± 9.3	4974± 115	1.23	341.6±16.0	0.996± 0.01	6.63	N	N
1569	76.4	-1.2±10.3	77.1±11.8	6401± 61	1.27	...± ...	1.009±0.003	...	N	N
1580	31.8	15.7± 3.0	28.5±10.0	5127± 102	2.50	...± ...	1.003±0.008	...	Y	Y
1620	19.5	1.9± 1.3	9.4± 2.0	6241± 191	4.19	322.4± 8.2	1.027±0.013	...	Y	N
1627	28.4	-7.4± 3.9	50.3± 3.9	4501± 68	1.19	302.7± 8.6	0.979±0.009	6.19	Y	N
1646	34.3	-3.6± 1.4	21.0± 0.5	4751± 73	1.62	411.6± 7.0	1.006±0.008	6.30	Y	N
1661	59.6	-9.3± 2.9	31.0± 1.6	6250± 73	1.82	150.1± 4.5	1.004±0.004	...	N	N
1665	51.8	-3.5± 5.0	77.6± 3.4	5088± 59	2.23	354.1± 6.8	1.008±0.005	6.21	Y	Y
1668	32.2	-5.1±15.1	113.1± 5.1	4323± 62	1.70	526.5±13.0	0.999±0.008	5.83	Y	N
1676	54.6	-0.3± 8.4	25.3±10.0	7728± 108	1.78	58.0± 4.9	0.994±0.005	...	Y	N
1686	61.2	-6.2± 2.5	54.8± 1.5	5057± 50	1.71	346.0± 4.9	1.006±0.004	6.26	N	N

Table 2. continued.

HSB2012	SNR	RV (km/s)	$v \sin i$ (km/s)	T_{eff} (K)	A_V	Li EW (mÅ)	γ	log age (yr)	H α	SB2
1690	37.0	-7.8± 1.1	15.7± 1.5	4887± 77	2.33	432.9± 5.8	0.994±0.007	6.19	Y	N
1689	58.2	-3.8±12.0	105.0± 8.8	5711± 65	1.49	234.3± 7.0	1.006±0.004	...	N	N
1693	21.7	-6.0± 2.8	37.0± 1.6	4677± 119	1.04	420.6±10.0	0.992±0.012	6.35	N	N
1699	95.2	-3.8± 4.6	75.0± 0.5	6157± 40	1.78	141.0± 5.1	1.005±0.003	...	Y	N
1725	67.0	-13.2± 2.6	66.5± 5.8	5367± 53	1.50	204.8± 5.0	1.004±0.004	6.44	N	N
1734	63.5	-7.9± 3.7	62.0± 3.1	4966± 46	1.54	360.9± 5.0	1.008±0.004	6.10	N	N
1772	28.5	-2.9± 2.2	10.2± 1.7	5726± 138	0.88	112.1± 6.4	0.983±0.009	...	N	N
1783	24.0	12.8± 2.2	25.4±10.0	4364± 89	1.16	...± ...	0.997±0.011	5.94	N	Y
1784	48.7	5.5±26.8	167.1± 4.2	5413± 67	1.75	341.9±13.0	1.009±0.005	...	Y	N
1805	25.0	-8.3± 7.9	93.0± 0.5	4585± 94	1.53	421.5±13.0	1.012±0.011	6.37	N	N
1816	21.5	-0.7± 4.9	73.7± 4.7	3882± 30	1.35	427.5±12.0	0.991±0.012	5.65	Y	N
1822	25.1	-11.2± 1.4	27.0± 0.5	4301± 66	1.73	562.5± 8.9	0.976± 0.01	5.91	N	N
1828	34.0	-12.1± 3.5	83.0± 4.6	4446± 61	1.67	459.4±12.0	1.014±0.008	5.85	Y	N
1832	24.8	0.9± 3.6	49.3± 3.7	4398± 75	1.41	284.0±10.0	0.993±0.011	...	N	N
1834	25.9	-4.7± 0.7	18.0± 0.5	4453± 90	1.76	492.5± 8.4	0.99± 0.01	...	Y	N
1848	30.3	-16.1±46.9	72.1±10.0	... ±± ...	0.996±0.009	...	Y	N
1859	46.1	5.2± 1.8	19.6±10.0	4871± 62	1.41	...± ...	1.001±0.006	6.26	N	Y
1874	74.1	-9.3±15.1	128.9± 6.0	5830± 52	1.39	193.5± 6.4	1.002±0.004	...	N	N
1885	98.6	1.1±11.0	40.0±15.7	6033± 44	0.89	71.9± 4.3	1.01±0.003	...	N	N
1904	57.6	-12.3± 5.0	67.0± 2.5	5463± 63	1.16	208.7± 5.0	1.007±0.005	...	N	N
1916	18.3	-27.8±12.7	96.0± 0.5	3968± 105	0.71	493.9±20.0	1.006±0.014	...	N	N
1933	24.1	5.2± 1.0	13.7± 1.7	4582± 113	2.09	507.8± 8.0	1.008±0.011	6.40	Y	N
1935	17.4	12.9±33.3	1.2±10.0	4885± 154	1.71	...± ...	1.007±0.015	6.92	N	N
1938	19.3	0.3± 1.1	15.7± 2.1	4783± 148	1.20	393.4± 7.5	1.014±0.014	6.69	N	N
1954	23.4	-8.5± 2.3	35.1± 1.5	4611± 112	1.71	482.6± 9.3	1.009±0.011	6.45	N	N
1962	21.0	-3.3± 2.8	27.0± 0.5	4796± 125	1.80	365.8±11.0	0.981±0.013	6.45	Y	N
1992	26.9	-10.3± 1.4	25.0± 1.6	4800± 104	1.60	387.4± 7.8	0.996± 0.01	6.35	Y	N
1999	18.1	-6.8± 3.9	75.5± 4.0	4284± 114	1.92	251.8±12.0	1.015±0.015	6.03	Y	N
2002	55.9	-24.0±22.8	1.2±10.0	8268± 116	1.08	...± ...	0.999±0.005	...	N	N
2007	79.6	-7.0±24.7	175.6±17.6	6457± 53	1.62	...± ...	1.005±0.003	...	Y	N
2016	24.4	-4.5± 0.9	18.0± 0.5	4271± 66	1.19	481.9± 7.5	0.968±0.011	6.27	N	N
2036	25.4	-3.3± 5.4	47.3± 3.1	4472± 81	1.10	301.9±11.0	0.992± 0.01	...	Y	N
2037	30.8	-12.8± 1.7	15.0± 0.5	3917± 25	0.36	...± ...	0.935±0.008	5.90	Y	N
2057	26.5	-13.3± 1.4	21.0± 0.5	4985± 109	1.71	380.1± 8.4	0.984± 0.01	6.95	Y	N
2062	19.6	-10.7± 1.5	24.0± 0.5	5087± 149	2.15	476.9±12.0	0.995±0.014	6.96	N	N
2105	18.3	2.4± 2.9	33.0± 0.5	4633± 112	1.44	341.3±11.0	1.018±0.014	6.46	N	N
2124	36.3	-8.7± 3.3	57.7± 1.6	5033± 84	1.34	297.4± 8.0	0.996±0.007	6.65	Y	N
2123	38.6	-10.1± 1.2	24.0± 0.5	4275± 42	1.42	516.0± 6.5	0.971±0.007	5.86	N	N
2142	21.8	-6.2± 1.6	16.0± 1.6	4799± 135	1.67	463.6± 8.3	0.995±0.012	6.81	Y	N
2145	23.1	-53.1±31.0	149.0±14.9	5158± 141	2.55	435.5±19.0	0.997±0.011	...	Y	N
2148	17.2	-7.6± 1.9	23.5±10.0	4732± 155	1.59	513.7±13.0	0.981±0.015	6.86	N	N
2157	20.3	-1.2± 0.9	15.3± 1.9	4623± 115	1.76	402.4± 9.2	0.966±0.013	6.63	N	N
2184	19.6	-10.0± 1.2	14.3± 1.6	4225± 80	1.43	567.2± 9.5	0.981±0.014	6.15	N	N
2195	17.2	-13.5± 2.3	13.5± 2.8	4790± 162	2.01	495.4±12.0	0.992±0.015	6.66	N	N
2207	20.4	-1.0± 2.9	27.0± 0.5	5147± 167	2.02	474.0±10.0	1.003±0.013	...	Y	N
2208	30.9	-6.7± 5.1	80.4± 1.4	4892± 92	1.74	287.6± 9.2	0.994±0.009	6.46	N	N
2210	24.7	-10.6±19.5	90.7± 8.6	4978± 103	1.94	223.4±16.0	1±0.011	6.93	N	N
2230	28.6	11.9± 1.5	18.0± 0.5	5122± 114	1.52	312.6± 8.4	1.014±0.009	6.96	N	N
2288	22.2	-9.0± 1.4	16.7± 1.7	4672± 109	1.60	383.8± 8.4	0.996±0.012	6.26	Y	N
2290	20.1	-3.4± 2.4	18.5±10.0	4451± 94	0.51	...± ...	0.986±0.013	7.15	Y	N
2300	29.2	-4.4± 4.0	36.0± 0.5	5218± 120	1.77	290.0± 8.3	0.995±0.009	6.63	N	N
2299	57.4	-20.2±11.0	108.0± 0.5	5417± 59	1.52	320.3± 7.0	1.015±0.005	...	N	N
2305	54.6	-5.3± 6.3	84.0± 3.0	5248± 59	1.32	181.8± 6.2	1.002±0.005	6.67	N	N
2331	29.4	-6.7± 0.9	16.5± 1.7	4572± 81	1.91	420.4± 7.1	1±0.009	6.45	Y	N
2335	38.1	-2.5± 3.3	66.8± 3.8	4651± 66	1.52	439.6± 9.4	0.999±0.007	6.30	Y	N
2337	26.0	-5.8± 4.2	42.0± 0.5	4565± 95	1.23	470.6±11.0	1.001± 0.01	6.56	Y	N
2348	16.6	-4.8±20.9	70.1±10.0	4785± 153	1.42	467.2±19.0	0.985±0.016	6.71	Y	N
2359	25.4	-7.9± 1.1	18.0± 0.5	4741± 110	1.71	492.3±10.0	0.984± 0.01	6.46	N	N
2363	20.1	-8.3± 1.3	24.0± 0.5	5152± 154	1.98	413.4±12.0	1.019±0.013	...	N	N
2371	27.8	-9.2± 5.1	51.0± 3.0	4909± 110	1.60	397.9± 9.6	1.006±0.009	6.54	Y	N

Table 2. continued.

HSB2012	SNR	RV (km/s)	$v \sin i$ (km/s)	T_{eff} (K)	A_V	Li EW (mÅ)	γ	log age (yr)	H α	SB2
2381	26.0	-2.0± 4.1	59.1± 2.3	4277± 79	1.25	455.7±10.0	1.005± 0.01	6.10	Y	N
2399	20.8	-9.0± 2.5	24.0± 0.5	4684± 133	1.41	459.6± 9.4	1.003±0.013	6.76	N	N
2405	27.2	-14.4± 2.6	47.6± 3.7	4838± 106	1.45	361.4±11.0	1.001± 0.01	...	N	N
2421	70.0	6.3±25.0	183.4± 9.0	5794± 51	1.78	...± ...	1.015±0.004	...	Y	N
2433	64.6	-30.9±26.6	148.2± 7.5	5325± 48	1.37	281.5± 9.6	1.013±0.004	6.65	Y	N
2439	46.6	-7.9± 1.0	21.0± 0.5	5286± 74	1.62	347.9± 5.2	1.014±0.006	...	Y	N
2460	56.8	-5.1±14.9	122.1± 4.8	5769± 68	1.41	261.8± 7.4	1.006±0.005	...	Y	N
2477	36.3	-17.7± 3.9	64.7± 2.4	4777± 74	1.59	431.9± 8.3	1.006±0.007	6.41	N	N
2479	40.7	-14.7± 1.3	27.0± 0.5	5213± 81	1.72	314.0± 5.7	0.998±0.006	6.66	N	N
2482	25.7	-8.3± 8.1	84.4± 3.0	4515± 83	1.84	503.0±15.0	1.019± 0.01	6.25	N	N
2495	75.2	-8.4± 6.9	79.0± 1.8	6069± 55	1.51	158.4± 5.5	1.014±0.003	...	N	N
2504	32.7	13.6±20.0	48.3±10.0	7554± 164	2.62	...± ...	0.997±0.008	...	Y	N
2506	133.9	-5.0±21.7	1.5±10.0	7900± 45	1.59	...± ...	1±0.002	...	N	N
2513	21.8	24.6±15.6	57.0± 4.3	4755± 125	1.49	345.7±19.0	1.01±0.012	6.48	N	N
2517	25.5	-8.7± 2.4	24.0± 0.5	4455± 88	1.29	411.0±11.0	0.997± 0.01	...	N	N
2519	22.9	-11.9± 1.7	18.0± 0.5	4897± 123	1.92	413.6± 7.9	1±0.012	6.78	N	N
2531	28.8	9.2± 7.1	54.9± 3.8	4432± 70	1.07	442.6±15.0	1.018±0.009	6.41	Y	N
2540	54.2	-8.2± 2.5	42.0± 0.5	5294± 63	1.47	316.2± 5.3	1.012±0.005	...	N	N
2551	46.8	-6.5± 1.5	27.0± 0.5	4986± 63	1.18	390.8± 5.9	0.999±0.006	6.58	N	N
2553	129.9	19.8± 9.3	81.8±10.0	8100± 48	1.41	...± ...	0.998±0.002	...	Y	N
2554	86.3	-16.4± 7.9	35.1±10.0	7990± 72	0.88	37.5± 3.7	1.006±0.003	...	N	N
2555	25.8	-2.6± 1.1	15.0± 0.5	4953± 109	1.73	366.0± 8.8	0.995± 0.01	6.91	Y	N
2565	29.7	-6.6±14.7	45.0± 0.5	4795± 87	2.12	399.9±14.0	1.018±0.009	6.43	Y	N
2569	25.6	-7.5± 2.0	40.9± 1.6	4729± 98	1.67	459.6±12.0	1.013± 0.01	6.54	N	N
2568	31.5	-3.0±10.0	74.0±10.0	6374± 154	3.48	...± ...	1.01±0.008	...	Y	Y
2570	29.8	19.8± 5.1	67.8±10.0	5287± 103	2.86	...± ...	0.997±0.009	...	Y	N
2584	36.6	-4.2± 3.6	33.8± 1.5	5205± 85	2.36	301.8± 7.3	1.004±0.007	6.69	Y	N
2585	47.1	-3.0± 1.5	21.0± 0.5	5060± 64	1.77	372.9± 5.0	1.003±0.006	6.29	Y	N
2597	16.1	0.9± 2.4	15.0± 0.5	3900± 45	0.75	236.3± 9.8	0.877±0.016	5.91	N	N
2598	87.7	-22.3±19.7	174.8± 4.8	5743± 41	2.43	230.1± 6.7	1.005±0.003	...	Y	N
2602	26.2	-3.0± 6.2	46.0± 4.3	4444± 84	1.10	484.5±10.0	0.999± 0.01	...	Y	N
2606	20.1	-8.8± 2.5	15.0± 0.5	4841± 143	2.10	365.4± 8.2	1.001±0.013	6.73	N	N
2609	30.4	13.5± 2.1	9.5± 2.3	4848± 88	3.38	...± ...	1.025±0.009	6.04	Y	N
2618	31.5	-9.1± 9.2	72.0± 0.5	4820± 91	1.70	457.4±10.0	1.002±0.008	6.37	Y	Y
2624	29.9	-7.0± 1.7	27.0± 0.5	4899± 96	1.16	452.3± 8.1	0.991±0.009	6.68	N	N
2636	31.9	-7.1±15.9	83.6± 3.0	4960± 89	1.58	355.7±11.0	0.988±0.008	6.59	N	N
2635	22.8	-55.1± 3.8	18.1±10.0	... ±± ...	1.04±0.011	...	Y	Y
2643	21.0	-3.0± 3.3	35.3± 1.5	5188± 156	2.21	442.9±10.0	1.008±0.012	...	Y	N
2669	21.2	-9.2±14.6	61.7± 3.4	4568± 97	1.25	525.6±16.0	1.012±0.012	6.87	Y	N
2674	53.7	-7.4± 0.9	15.7± 1.5	5082± 59	1.65	409.2± 4.3	1.001±0.005	6.42	Y	N
2675	47.7	-3.7± 8.7	83.1± 4.8	4804± 56	1.76	341.5± 9.2	1.005±0.006	6.27	Y	N
2677	68.8	-1.0± 3.3	68.0± 1.6	5032± 45	1.84	256.2± 5.8	0.99±0.004	6.26	Y	N
2680	19.6	-7.4± 2.6	21.0± 0.5	4472± 115	1.23	444.0± 9.0	0.997±0.014	...	Y	N
2692	18.8	5.5± 5.4	18.0± 0.5	6287± 165	2.55	420.1±13.0	1.004±0.014	...	Y	N
2708	58.1	-3.6± 2.7	33.0± 0.5	6166± 74	1.20	160.5± 4.4	1.007±0.005	...	N	N
2726	52.9	-9.4±13.1	103.8± 1.7	5086± 58	1.15	294.5± 8.1	1.012±0.005	6.44	Y	N
2755	60.3	-9.2± 1.1	18.3± 1.2	6184± 72	0.12	105.9± 3.7	0.996±0.004	...	N	N
2760	17.4	-6.5± 1.6	16.7± 1.7	4650± 134	1.74	517.5±11.0	0.967±0.015	6.63	Y	N
2761	64.2	-6.5± 1.4	21.0± 0.5	5423± 51	2.10	294.9± 4.1	1.004±0.004	...	Y	N
2763	37.2	-7.0± 6.1	69.5± 2.3	4814± 71	1.26	277.0±10.0	1.006±0.007	6.39	Y	N
2769	19.5	6.2± 4.8	96.0± 0.5	4494± 135	1.58	409.2±17.0	1.007±0.013	6.49	N	N
2774	66.9	-14.6±12.3	87.0± 7.4	5805± 59	2.11	176.3± 6.4	1.009±0.004	...	Y	N
2779	45.8	-8.5± 1.2	25.0± 1.6	5617± 83	1.67	369.3± 5.6	1.017±0.006	6.97	N	N
2782	24.8	-15.5± 3.6	22.3± 1.7	4587± 92	1.69	397.4± 9.1	0.997±0.011	6.59	N	N
2812	37.8	-24.1±39.2	188.6± 6.6	5426± 91	2.18	490.0±15.0	1.015±0.007	6.70	N	N
2818	29.9	1.3±23.1	48.7± 6.2	5125± 101	2.07	278.2±12.0	1.016±0.009	6.86	Y	N
2833	36.8	-8.3± 2.5	81.0± 0.5	4810± 70	1.51	375.2± 9.5	1.004±0.007	6.36	N	N
2846	77.6	-13.9±10.0	76.8± 1.7	5763± 47	2.02	184.4± 4.9	1.002±0.003	...	Y	N
2866	30.8	-2.5± 2.6	45.0± 0.5	4814± 93	1.47	446.3±10.0	1.002±0.009	6.55	Y	N
2872	115.5	3.5±13.4	97.3±10.0	7892± 53	1.01	71.3± 3.1	1.002±0.002	...	N	N

Table 2. continued.

HSB2012	SNR	RV (km/s)	$v \sin i$ (km/s)	T_{eff} (K)	A_V	Li EW (mÅ)	γ	log age (yr)	H α	SB2
2887	38.0	12.4± 5.6	82.0±11.4	3543±1476	0.29	...± ...	0.913±0.007	...	Y	N
2890	48.9	-23.8± 2.1	23.5± 3.0	6215± 89	1.39	192.8± 5.3	1.015±0.005	...	N	N
2898	31.8	-9.4± 4.1	71.6± 2.7	4648± 82	1.73	547.8±13.0	0.995±0.008	6.30	Y	N
2902	21.3	-5.2± 3.7	40.8± 1.7	4845± 136	1.52	393.3±11.0	0.99±0.012	6.75	N	N
2908	50.5	-12.2± 4.0	60.0± 2.2	5291± 68	1.20	213.8± 5.3	0.998±0.005	6.65	N	N
2909	81.0	-2.1±13.8	127.8±13.4	5392± 38	2.77	203.4± 6.4	1.014±0.003	...	Y	N
2923	38.8	1.4± 9.6	109.4± 9.0	4585± 55	1.42	286.0± 9.7	1.015±0.007	5.94	Y	N
2926	68.1	11.9±29.3	124.3±21.5	5283± 46	2.86	...± ...	1.011±0.004	...	Y	N
2946	15.4	5.1±10.9	37.7± 4.2	5063± 185	1.59	408.6±17.0	1.004±0.017	6.97	N	N
2947	24.8	-7.5± 4.7	49.0± 1.6	5769± 148	2.91	279.7± 8.5	0.993±0.011	...	N	N
2949	22.2	-4.6± 1.4	18.0± 0.5	4648± 116	2.41	482.3± 8.4	0.996±0.012	6.15	Y	N
2948	15.4	-2.0± 2.5	21.5±10.0	5348± 212	1.56	157.9±14.0	1.025±0.017	...	N	N
2950	54.5	-1.0± 9.3	109.0± 6.2	5659± 66	1.11	142.3± 7.1	1.005±0.005	...	N	N
2966	24.5	-10.5± 3.1	30.0± 0.5	5653± 156	2.06	401.8± 9.2	0.994±0.011	...	N	N
2967	26.8	-3.0± 1.5	24.7± 1.5	5029± 110	2.07	417.3± 8.1	0.998± 0.01	6.52	N	N
2970	47.3	-39.9± 8.1	40.7± 4.6	5672± 71	2.72	266.9± 6.9	1.001±0.006	...	Y	N
2972	50.0	-3.0±30.3	166.5± 7.5	5788± 74	1.47	231.6± 9.9	1.013±0.005	...	Y	N
2985	19.4	-5.2± 2.0	27.0± 0.5	4309± 81	1.58	529.2±12.0	0.994±0.014	6.27	Y	N
2987	20.9	-18.9±11.9	77.6± 3.2	4548± 104	1.48	357.6±16.0	0.988±0.013	6.37	N	N
3019	16.1	-10.0± 4.5	32.0± 1.6	4619± 129	2.30	569.0±13.0	0.982±0.016	6.23	Y	N
3021	84.1	-11.6±10.9	108.2± 8.3	5870± 46	1.65	145.8± 6.0	1.01±0.003	...	N	N
3032	70.4	-7.2± 3.6	71.7± 4.7	5981± 57	2.59	181.3± 5.5	1.006±0.004	...	N	N
3041	25.1	-10.3±13.7	78.9± 3.8	4727± 99	1.68	508.2±14.0	1.01± 0.01	6.31	Y	N
3044	23.6	-17.7± 2.3	30.0± 3.0	5101± 142	0.81	200.1± 9.7	1.004±0.011	6.84	N	N
3051	25.1	0.2± 8.9	52.3± 2.4	4311± 68	1.10	374.5±13.0	0.986±0.011	6.36	Y	N
3065	46.2	-10.8± 1.2	19.2± 1.7	5585± 78	1.02	172.2± 5.2	0.99±0.006	...	N	N
3067	52.7	-5.8± 3.6	60.0±30.0	7288± 102	2.84	72.6± 4.1	1.002±0.005	...	N	N
3073	76.4	-5.6± 1.8	37.5± 1.7	5676± 50	1.34	222.5± 4.1	1.011±0.003	...	N	N
3089	77.4	-15.0±20.0	...± ±± ...	1±0.003	...	Y	N
3094	18.3	-3.5± 6.9	50.6± 2.0	4284± 92	1.31	525.3±12.0	0.979±0.015	6.11	N	N
3102	20.5	2.0± 8.7	43.8± 3.5	4788± 125	0.58	...± ...	0.982±0.013	6.91	N	N
3104	34.3	0.7± 5.5	65.0± 2.2	4768± 84	1.31	393.4± 8.3	0.997±0.008	6.27	N	N
3112	18.2	-6.2± 4.5	29.4± 3.3	5962± 217	3.36	282.6±12.0	1.023±0.015	...	N	N
3116	18.0	-6.2± 1.4	15.0± 0.5	4474± 138	0.86	438.5±11.0	0.987±0.015	6.81	N	N
3120	33.9	-21.2± 1.6	22.7± 2.4	4505± 66	1.80	486.5± 6.7	1.009±0.008	5.86	Y	N
3134	72.7	-14.1± 2.3	27.0± 1.7	6110± 58	1.47	166.4± 3.9	1.005±0.004	...	N	N
3136	28.4	-7.8± 3.4	47.6± 3.0	5141± 111	1.95	331.1± 9.2	0.994±0.009	...	N	N
3158	60.5	-2.8± 0.9	12.0± 0.5	4430± 29	0.27	...± ...	0.927±0.004	...	Y	N
3161	25.0	-6.6±10.8	86.3± 1.6	... ±	373.2±15.0	1.001±0.011	...	N	N
3198	44.0	-11.7± 1.6	31.8± 1.7	4754± 60	1.78	451.2± 6.9	1.017±0.006	6.10	Y	N
3196	40.1	-4.7±17.6	130.1±10.3	5547± 95	2.36	222.6±10.0	1.016±0.006	...	N	N
3200	48.8	-5.1±26.0	164.0± 1.6	5375± 63	1.94	275.6±10.0	1.007±0.005	...	Y	N
3217	18.0	-7.8± 2.2	14.3± 1.4	4981± 152	2.43	454.5± 9.4	0.984±0.015	6.77	N	N
3219	36.7	-8.7± 1.9	16.3± 1.7	5015± 77	1.37	357.4± 6.1	1.003±0.007	6.58	N	N
3244	27.0	-9.6± 0.9	18.0± 0.5	4613± 87	2.09	495.3± 8.8	0.986± 0.01	6.29	Y	N
3271	43.0	5.3± 5.6	34.2± 2.7	4961± 72	1.73	358.5± 7.3	1.006±0.006	6.52	Y	N
3287	51.5	0.7± 0.8	18.0± 0.5	5004± 58	0.09	190.3± 4.2	0.987±0.005	6.69	N	N
3294	37.7	-62.0± 1.1	75.9±10.0	5032± 78	1.76	311.9±10.0	0.991±0.007	6.62	N	N
3319	56.0	-11.3±11.5	81.0± 3.5	5044± 51	1.63	393.1± 6.4	1.006±0.005	6.24	Y	N
3326	17.3	-4.1± 6.3	48.8± 2.7	4396± 107	1.72	450.8±15.0	0.997±0.015	...	N	N
3338	24.4	-7.1± 3.8	30.0± 0.5	4706± 105	2.21	470.7± 9.4	1.01±0.011	6.31	Y	N
3358	65.0	-7.2± 6.4	82.3± 1.7	5392± 53	1.42	301.1± 6.7	0.997±0.004	...	N	N
3359	16.3	-15.2±35.8	108.0± 0.5	5009± 168	2.34	496.8±24.0	1.017±0.016	6.80	Y	N
3367	67.2	-7.7± 7.6	67.5± 1.7	5316± 51	1.94	220.0± 5.8	1.007±0.004	...	N	N
3374	59.5	-22.2± 2.0	22.1± 1.6	5227± 56	1.52	285.4± 4.4	1.003±0.004	6.63	N	N
3395	81.0	-5.4±13.0	119.5± 5.6	5773± 45	1.47	206.4± 6.3	1.009±0.003	...	N	N
3399	48.2	53.0± 1.1	15.0± 0.5	4263± 33	0.80	...± ...	0.978±0.005	5.75	Y	Y
3409	15.9	6.7± 2.1	7.0± ...	4811± 181	1.43	298.0±11.0	0.986±0.017	6.88	N	N
3412	41.0	-7.7± 3.6	73.3± 2.4	5016± 74	2.04	316.2±10.0	1.005±0.006	6.55	N	N
3415	65.9	-0.2±12.6	141.0± 0.5	5508± 48	1.82	247.1± 8.7	1.011±0.004	6.22	Y	N

Table 2. continued.

HSB2012	SNR	RV (km/s)	$v \sin i$ (km/s)	T_{eff} (K)	A_V	Li EW (mÅ)	γ	log age (yr)	H α	SB2
3425	26.7	-2.3±27.9	83.0± 3.5	4940± 102	1.03	397.6±11.0	0.995± 0.01	6.81	Y	N
3427	54.9	-9.4± 1.5	18.6± 2.1	5846± 73	2.49	220.3± 4.1	1.007±0.005	...	Y	N
3435	35.5	-5.5± 1.9	24.0± 0.5	5085± 85	1.81	419.7± 7.0	0.991±0.007	6.82	Y	N
3438	39.8	-9.8± 2.2	18.8± 1.5	5204± 83	1.73	353.9± 6.2	1.002±0.007	6.91	Y	N
3443	21.6	-11.4±11.5	38.0± 3.7	4729± 128	1.83	239.7±13.0	0.987±0.012	6.62	N	N
3442	68.7	-21.0± 2.2	17.2± 2.9	6431± 58	0.82	100.0± 3.3	1±0.004	...	Y	N
3454	64.4	-8.0±23.8	158.0± 1.8	5840± 60	1.63	180.0± 7.3	1.022±0.004	...	N	N
3480	22.7	0.0± 4.4	77.4± 4.5	3985± 38	0.36	418.8±14.0	0.979±0.011	6.30	N	N
3485	18.9	-8.0± 2.3	14.0± 1.6	5342± 187	2.53	469.2±11.0	0.995±0.014	6.96	N	N
3488	23.6	11.3± 2.1	22.9±10.0	4911± 116	1.66	...± ...	1.004±0.011	6.75	N	N
3505	70.1	-7.5± 3.0	42.0± 2.5	5531± 49	1.31	265.9± 3.9	1.002±0.004	...	Y	N
3508	48.6	5.5±17.8	91.2± 8.7	5164± 61	1.89	321.0±10.0	1.005±0.005	6.40	N	N
3524	21.1	-9.7± 5.6	27.0± 0.5	4443± 91	1.61	397.3±11.0	0.984±0.012	...	N	N
3531	39.2	-8.3± 2.6	27.0± 0.5	5538± 96	1.30	299.2± 5.6	1.008±0.007	...	N	N
3541	15.3	-4.2± 6.3	76.5± 4.8	5036± 176	1.78	355.5±16.0	0.978±0.017	...	N	N
3536	37.5	-2.8± 8.9	72.9± 1.5	4915± 79	1.55	327.4± 8.6	1.001±0.007	6.27	Y	N
3549	21.0	-11.3± 3.6	18.0± 0.5	4297± 73	1.06	529.1± 9.4	0.978±0.013	6.43	N	N
3554	22.2	-10.0± 1.5	15.0± 0.5	4461± 90	1.59	518.7± 8.4	0.982±0.012	...	N	N
3557	21.0	-8.7± 3.4	27.0± 0.5	4907± 123	2.08	467.6±11.0	0.995±0.013	6.57	N	N
3558	39.3	-8.8±13.7	88.5± 1.7	4880± 66	1.09	327.6± 9.4	1.002±0.007	6.48	N	N
3578	32.2	-7.0± 1.6	24.0± 0.5	5524± 112	2.01	427.4± 6.9	0.997±0.008	...	N	N
3577	18.2	-7.1± 1.3	14.4± 1.4	5115± 175	2.59	382.7±10.0	1.009±0.014	6.58	Y	N
3617	31.2	-22.3± 3.3	32.6± 2.8	6163± 137	2.20	207.7± 7.0	1±0.008	...	N	N
3628	27.3	-6.8± 1.4	24.0± 0.5	5165± 117	2.53	495.2± 8.1	0.976± 0.01	6.67	Y	N
3633	18.5	-89.7± 0.9	99.0± 0.5	4812± 141	1.73	556.6±20.0	1.002±0.014	6.68	Y	N
3636	26.0	-8.7± 5.9	49.3± 1.7	5515± 141	2.69	358.3± 8.9	0.999± 0.01	...	N	N
3644	33.9	-12.2± 1.5	12.0± 0.5	4591± 60	0.78	...± ...	0.897±0.008	6.74	Y	N
3650	18.0	18.0± 2.0	9.9± 2.9	5144± 173	2.25	274.1± 9.4	1.027±0.015	6.79	N	N
3660	30.3	-1.4±11.5	96.0± 5.5	4655± 76	2.15	377.2±16.0	1.031±0.009	6.21	Y	N
3668	15.2	-3.3± 1.6	17.0± 1.6	4478± 136	1.08	367.0± 9.9	0.982±0.017	...	N	N
3683	101.4	12.0± 0.3	7.4± 1.7	4439± 21	4.20	150.4± 2.4	1.056±0.003	...	N	N
3692	36.4	-3.3± 8.0	51.0± 0.5	5649± 92	1.82	355.8± 7.7	0.988±0.007	6.96	N	N
3716	16.8	0.6± 8.3	45.0± 0.5	4003± 54	0.90	354.5±14.0	0.988±0.016	6.10	N	N
3722	22.8	-7.8± 2.4	15.0± 0.5	5075± 127	1.88	404.0± 7.9	1.003±0.012	...	Y	N
3732	19.0	-14.3± 5.8	72.0± 0.5	4906± 157	2.36	506.1±15.0	1.006±0.014	6.61	Y	N
3749	24.9	-5.5±16.5	81.0± 5.7	4598± 91	1.83	357.7±17.0	0.984± 0.01	6.38	N	N
3808	23.5	-8.3± 1.6	12.0± 0.5	4644± 99	1.44	455.7± 9.7	0.986±0.011	6.79	N	N
3830	71.6	-0.5±18.3	106.0±13.7	6051± 59	1.24	120.4± 6.4	1.011±0.004	...	N	N
3834	26.1	8.5±15.0	112.4±29.9	5291± 117	3.20	...± ...	1.007± 0.01	...	Y	N
3846	18.6	-11.6± 2.6	21.0± 0.5	5338± 195	1.90	370.2±10.0	0.98±0.014	...	N	N
3847	21.7	-7.0±18.3	93.5± 3.0	4716± 104	2.03	472.4±15.0	0.992±0.012	6.38	Y	N
3849	19.7	-8.5±20.6	78.8± 5.5	4551± 114	1.47	466.3±15.0	1.009±0.014	6.61	N	N
3860	24.3	2.2± 3.7	42.0± 0.5	4914± 125	0.87	276.8±12.0	0.996±0.011	6.75	Y	N
3873	48.1	5.0±13.9	130.1± 6.2	5488± 73	2.66	343.9±11.0	1.003±0.005	...	N	N
3875	70.7	-11.5±33.3	179.6± 3.7	5299± 43	1.63	213.0± 7.9	1.015±0.004	...	Y	N
3879	29.9	-6.8± 3.4	43.7± 1.7	5421± 123	2.19	334.9± 7.9	1.018±0.009	...	N	N
3909	56.4	2.3± 5.6	61.7±12.7	7287± 96	0.62	45.6± 4.1	1.006±0.005	...	N	N
3916	18.3	-6.2± 3.6	26.1± 1.5	4860± 173	2.26	335.1±11.0	0.971±0.014	6.56	N	N
3954	35.5	-15.6±13.4	140.0± 4.5	5485± 98	1.99	288.1±11.0	1.027±0.007	...	N	N
3956	29.8	-8.2± 1.1	21.0± 0.5	4919± 100	1.86	408.8± 8.1	1±0.009	6.63	N	N
3970	41.1	-7.2± 3.9	57.0± 0.5	5330± 83	2.16	258.1± 7.0	1.003±0.006	...	N	N
4049	15.4	-5.3± 2.1	24.9± 2.3	4361± 117	1.95	513.4±12.0	0.986±0.017	5.98	N	N
4187	30.6	-3.2± 9.8	58.7± 7.7	7190± 172	3.65	...± ...	1.008±0.009	...	N	N
4218	57.2	-5.5± 0.6	15.0± 0.5	4514± 37	0.15	110.8± 3.7	0.948±0.005	6.03	N	N
4244	114.3	-2.2± 6.0	94.3± 1.7	8318± 54	2.12	60.8± 2.3	1.005±0.002	...	Y	N
4274	19.0	14.5± 1.2	15.1±10.0	4921± 164	4.54	359.0± 8.6	1.048±0.014	5.86	N	N
4282	45.7	-41.8±43.3	76.4±10.0	7901± 134	4.66	...± ...	1.014±0.006	...	Y	N
4338	23.3	-11.3± 2.9	36.0± 3.3	4343± 82	2.68	554.9± 8.4	1.004±0.011	5.63	Y	N
4366	28.6	-20.6±16.5	4.7±10.0	7298± 191	0.51	...± ...	1.015±0.009	...	N	N
4392	69.9	-2.6± 5.0	48.2±15.7	6834± 78	0.21	...± ...	1.001±0.004	...	N	N

Table 2. continued.

HSB2012	SNR	RV (km/s)	$v \sin i$ (km/s)	T_{eff} (K)	A_V	Li EW (mÅ)	γ	log age (yr)	H α	SB2
4415	20.0	-0.8±11.7	89.3±10.0	5867± 198	1.93	191.2±14.0	1.011±0.013	...	N	N

Table 7. Early-type stars. Column “SpT” reports the spectral type listed in SIMBAD. Column “Notes” reports our classification, in particular: “B SG” indicates candidate B supergiants; “HAeBe” indicates Herbig Ae/Be stars; “near A0” indicates stars of late-B/early-A type.

2MASS Id	SIMBAD Id	RA	Dec	<i>V</i>	<i>B</i> – <i>V</i>	<i>V</i> – <i>I</i>	SpT	Notes
10430716-5931209	[HSB2012] 230	10:43:07.16	-59:31:20.9	15.06	1.08	1.76	...	B type
10432086-5929595	[HSB2012] 538	10:43:20.86	-59:29:59.6	14.43	0.39	0.72	...	B type
10433865-5934444	Cl Trumpler 14 43	10:43:38.66	-59:34:44.5	12.17	0.42	0.71	...	B type
10434798-5933590	Cl Trumpler 14 45	10:43:47.98	-59:33:59.1	13.2	0.44	0.73	...	B type
10435224-5936585	[HSB2012] 1385	10:43:52.24	-59:36:58.5	12.24	0.4	0.7	...	B type
10435250-5942503	[HSB2012] 1395	10:43:52.50	-59:42:50.4	16.47	1.1	1.8	...	B type
10435723-5932411	Cl* Trumpler 14 VBF 65	10:43:57.24	-59:32:41.2	12.85	0.31	0.55	...	B type
...	[HSB2012] 1618	10:43:59.20	-59:33:21.5	13.44	0.39	0.67	...	B type
10440320-5937380	Cl* Trumpler 14 Y 461	10:44:03.20	-59:37:38.1	12.67	0.3	0.54	...	B type
10440384-5933099	Cl Trumpler 14 38	10:44:03.84	-59:33:10.0	13.23	0.34	0.55	...	B type
10440590-5944277	Cl* Trumpler 14 Y 339	10:44:05.91	-59:44:27.7	15.34	0.78	1.36	...	B type
10440976-5944480	[HSB2012] 1913	10:44:09.76	-59:44:48.0	15.2	0.74	1.35	...	B type
10441215-5933511	Cl Trumpler 16 130	10:44:12.15	-59:33:51.2	12.92	0.35	0.55	...	B type
10441249-5943276	Cl* Trumpler 14 MJ 251	10:44:12.50	-59:43:27.6	14.4	0.57	1.13	...	B type
10441282-5933321	Cl Trumpler 16 131	10:44:12.83	-59:33:32.2	13.56	0.37	0.59	...	B type
10441380-5942571	Cl Trumpler 16 245	10:44:13.80	-59:42:57.1	12.33	0.5	1.2	B0V	B type
10441535-5936042	Cl* Trumpler 14 Y 467	10:44:15.36	-59:36:04.3	13.22	0.44	0.67	...	B type
10441968-5943078	Cl Trumpler 16 247	10:44:19.69	-59:43:07.9	13.54	0.29	0.52	...	B type
10442048-5930470	Cl* Trumpler 14 Y 11	10:44:20.48	-59:30:47.0	13.49	0.35	0.52	...	B type
10442451-5945441	Cl* Trumpler 14 Y 300	10:44:24.52	-59:45:44.1	15.18	0.67	1.13	...	B type
10442909-5948207	Cl* Trumpler 14 MJ 328	10:44:29.10	-59:48:20.7	12.66	0.88	1.45	...	B type
10442945-5933437	Cl* Trumpler 14 Y 50	10:44:29.46	-59:33:43.8	13.25	0.37	0.59	...	B type
10443132-5930376	Cl* Trumpler 14 Y 30	10:44:31.33	-59:30:37.7	12.3	0.33	0.55	...	B type
10443341-5933189	2MASS J10443341-5933189	10:44:33.42	-59:33:19.0	16.27	0.46	1.38	...	B type
10444710-5939201	Cl Trumpler 16 44	10:44:47.11	-59:39:20.2	13.49	0.61	1.02	B3:	B type
10444848-5947493	[HSB2012] 2913	10:44:48.49	-59:47:49.4	16.2	1.5	2.23	...	B type
10445036-5934468	Cl* Trumpler 14 Y 60	10:44:50.36	-59:34:46.9	13.6	0.44	0.72	...	B type
10445160-5943136	Cl Trumpler 16 47	10:44:51.60	-59:43:13.6	12.85	0.38	0.64	B3:	B type
10445201-5939322	[HSB2012] 3017	10:44:52.02	-59:39:32.2	14.78	1.01	1.58	...	B type
10445602-5938530	Cl Trumpler 16 215	10:44:56.02	-59:38:53.0	13.33	0.6	1.14	...	B type
...	[HSB2012] 3150	10:44:56.80	-59:40:02.5	13.19	0.39	0.62	...	B type
10445837-5932062	Cl* Trumpler 14 MJ 451	10:44:58.38	-59:32:06.3	13.24	0.44	0.7	...	B type
...	Cl Trumpler 16 38	10:45:00.20	-59:40:05.2	13.28	0.34	0.55	B5:	B type
10450198-5934058	Cl* Trumpler 14 Y 89	10:45:01.99	-59:34:05.9	15.11	0.75	1.27	...	B type
...	Cl Trumpler 16 69	10:45:07.90	-59:41:34.1	12.96	0.41	0.69	...	B type
10450792-5939011	Cl Trumpler 16 51	10:45:07.93	-59:39:01.2	12.8	0.33	0.55	B	B type
10450836-5938475	Cl Trumpler 16 52	10:45:08.37	-59:38:47.5	12.62	0.38	0.68	B3:	B type
...	[HSB2012] 3545	10:45:09.90	-59:42:13.9	12.39	0.36	0.58	...	B type
10451271-5939066	Cl Trumpler 16 54	10:45:12.72	-59:39:06.6	12.83	0.39	0.6	B3:	B type
10451355-5943318	Cl* Trumpler 14 Y 206	10:45:13.55	-59:43:31.8	14.17	0.47	0.83	B	B type
10451588-5929563	Cl* Trumpler 14 MJ 525	10:45:15.89	-59:29:56.4	12.06	0.36	0.59	...	B type
10451622-5941411	Cl Trumpler 16 238	10:45:16.22	-59:41:41.2	13.55	0.47	0.84	B	B type
10451717-5947013	[HSB2012] 3729	10:45:17.18	-59:47:01.4	17.5	1.68	2.94	...	B type

Table 7. continued.

2MASS Id	SIMBAD Id	RA	Dec	V	B - V	V - I	SpT	Notes
10451730-5941204	Cl Trumpler 16 239	10:45:17.30	-59:41:20.4	13.6	0.41	0.66	...	B type
10451798-5941095	Cl Trumpler 16 240	10:45:17.99	-59:41:09.5	13.85	0.42	0.68	...	B type
10451809-5938223	[HSB2012] 3755	10:45:18.09	-59:38:22.4	16.27	0.9	1.45	...	B type
10451899-5941427	Cl Trumpler 16 241	10:45:18.99	-59:41:42.7	14.06	0.42	0.73	...	B type
10452216-5942436	[HSB2012] 3880	10:45:22.17	-59:42:43.7	17.13	1.83	2.68	...	B type
10452310-5944458	Cl* Trumpler 14 Y 256	10:45:23.11	-59:44:45.8	13.6	0.51	0.88	...	B type
10452415-5942313	Cl* Trumpler 14 Y 193	10:45:24.16	-59:42:31.4	13.38	0.4	0.68	B	B type
10453134-5941133	Cl* Trumpler 16 MJ 585	10:45:31.34	-59:41:13.3	12.67	0.37	0.64	...	B type
10453254-5942359	Cl* Trumpler 14 Y 151	10:45:32.55	-59:42:35.9	13.07	0.53	0.9	...	B type
10453607-5945295	2MASS J10453607-5945295	10:45:36.07	-59:45:29.6	16.79	0.93	1.8	...	B type
10453660-5944110	[S87b] IRS 41	10:45:36.61	-59:44:11.1	13.62	1.07	2.02	...	B type
10453807-5944095	Cl* Trumpler 16 MJ 599	10:45:38.08	-59:44:09.5	13.05	0.77	1.51	...	B type
10453819-5942157	Cl* Trumpler 14 Y 150	10:45:38.20	-59:42:15.7	13.8	0.51	0.92	...	B type
10454060-5937041	Cl* Trumpler 16 MJ 602	10:45:40.61	-59:37:04.2	13.24	0.43	0.75	...	B type
10454118-5936392	Cl* Trumpler 16 MJ 603	10:45:41.18	-59:36:39.2	13.02	0.56	0.85	...	B type
10433663-5934509	Cl Trumpler 14 53	10:43:36.64	-59:34:51.0	13.58	0.56	0.98	...	B SG
10434355-5935450	Cl Trumpler 14 61	10:43:43.56	-59:35:45.1	13.53	0.55	1.03	...	B SG
10440384-5934344	Cl* Trumpler 14 Y 519	10:44:03.84	-59:34:34.4	13.07	0.33	0.54	...	B SG
10440992-5946185	[HSB2012] 1920	10:44:09.93	-59:46:18.6	15.81	1.91	3.04	...	B SG
10445393-5945240	Cl* Trumpler 14 Y 226	10:44:53.94	-59:45:24.0	13.59	0.36	0.62	...	B SG
10451925-5929522	Cl* Trumpler 14 MJ 540	10:45:19.25	-59:29:52.2	12.49	0.5	0.95	...	B SG
10452648-5946188	[HSB2012] 3994	10:45:26.49	-59:46:18.9	16.13	1.04	1.93	...	B SG
10452875-5930037	[HSB2012] 4044	10:45:28.76	-59:30:03.8	13.66	0.91	1.52	...	B SG
10454365-5939540	Cl* Trumpler 14 Y 142	10:45:43.65	-59:39:54.0	12.95	0.34	0.59	...	B SG
10453674-5947020	[S87b] IRS 42	10:45:36.75	-59:47:02.0	15.08	1.64	2.89	...	O type
10453024-5948206	[S87b] IRS 38	10:45:30.25	-59:48:20.6	17.64	2.27	4.09	...	O type?
10433352-5934383	Cl* Trumpler 14 Y 501	10:43:33.53	-59:34:38.3	14.5	0.48	0.78	...	near A0
10433948-5931460	Cl* Trumpler 14 VBF 149	10:43:39.49	-59:31:46.0	14.61	0.52	0.86	...	near A0
10434041-5932584	Cl* Trumpler 14 Y 598	10:43:40.42	-59:32:58.4	13.63	0.62	1.01	...	near A0
10434176-5932588	Cl* Trumpler 14 Y 599	10:43:41.76	-59:32:58.8	14.4	0.56	1.01	...	near A0
10434269-5934435	Cl* Trumpler 14 MJ 96	10:43:42.70	-59:34:43.6	14.32	0.54	0.89	...	near A0
10434766-5942391	[HSB2012] 1231	10:43:47.67	-59:42:39.2	17.88	1.31	2.11	...	near A0
10435515-5933344	[HSB2012] 1476	10:43:55.16	-59:33:34.4	14.08	0.44	0.79	...	near A0
10435886-5943036	Cl* Trumpler 14 Y 402	10:43:58.86	-59:43:03.7	15.43	0.65	1.14	...	near A0
10440976-5943383	Cl* Trumpler 14 Y 400	10:44:09.76	-59:43:38.4	14.85	0.53	0.97	...	near A0
...	[HSB2012] 1950	10:44:10.70	-59:42:51.2	15.45	0.57	1.08	...	near A0
10444195-5942472	Cl Trumpler 16 228	10:44:41.96	-59:42:47.3	13.72	0.32	0.5	...	near A0
10445290-5939245	DETC Tr 16 J104452.9-593924	10:44:52.90	-59:39:24.6	16.55	1.19	1.78	...	near A0
10450403-5946292	Cl* Trumpler 14 Y 268	10:45:04.03	-59:46:29.3	14.73	0.54	0.94	...	near A0
...	[HSB2012] 3378	10:45:04.40	-59:41:47.5	13.47	0.45	0.66	...	near A0
10450477-5933198	Cl* Trumpler 14 Y 80	10:45:04.77	-59:33:19.9	13.64	0.49	0.77	...	near A0
...	[HSB2012] 3593	10:45:11.70	-59:41:16.3	13.64	0.35	0.55	...	near A0
...	[HSB2012] 3648	10:45:14.00	-59:41:42.0	13.02	0.4	0.63	...	near A0
10451484-5943341	2MASS J10451484-5943341	10:45:14.85	-59:43:34.1	13.85	0.7	1.14	...	near A0

Table 7. continued.

2MASS Id	SIMBAD Id	RA	Dec	<i>V</i>	<i>B - V</i>	<i>V - I</i>	SpT	Notes
10452008-5942084	CI* Trumpler 14 Y 190	10:45:20.09	-59:42:08.4	13.99	0.45	0.74	B	near A0
10452660-5943475	CI* Trumpler 14 Y 235	10:45:26.61	-59:43:47.5	14.72	0.56	0.91	...	near A0
10452732-5945187	2MASS J10452732-5945187	10:45:27.33	-59:45:18.7	17.05	1.04	2.01	...	near A0
10453920-5943105	2MASS J10453920-5943105	10:45:39.21	-59:43:10.6	15.65	0.57	1.09	...	near A0
10454039-5938374	[HSB2012] 4287	10:45:40.39	-59:38:37.4	15.75	0.72	1.25	...	near A0
10454449-5939258	CI* Trumpler 14 Y 135	10:45:44.50	-59:39:25.9	14.61	0.68	1.03	...	near A0
10452263-5930223	2MASS J10452263-5930223	10:45:22.64	-59:30:22.4	14.02	0.54	0.96	...	B type - HAeBe
10440993-5934360	CI* Trumpler 14 VBF 93	10:44:09.93	-59:34:36.0	13.56	0.24	0.68	...	near A0 - HAeBe
10443883-5933470	2MASS J10443883-5933470	10:44:38.84	-59:33:47.0	13.88	0.42	0.76	...	near A0 - HAeBe
10445220-5944212	2MASS J10445220-5944212	10:44:52.20	-59:44:21.3	12.66	0.4	0.74	...	near A0 - HAeBe
10450972-5945448	CI* Trumpler 14 Y 265	10:45:09.73	-59:45:44.9	15.23	0.7	1.19	...	near A0 - HAeBe
10453372-5949596	[HSB2012] 4157	10:45:33.72	-59:49:59.7	14.74	0.93	1.58	...	near A0 - HAeBe
10435015-5934068	CI* Trumpler 14 Y 555	10:43:50.16	-59:34:06.8	13.89	0.74	1.23	...	HAeBe
10440112-5935352	2MASS J10440112-5935352	10:44:01.12	-59:35:35.3	14.98	0.66	1.13	...	HAeBe
10442806-5948127	[HSB2012] 2420	10:44:28.07	-59:48:12.7	16.14	0.93	1.57	...	HAeBe
10443030-5937326	[HSB2012] 2494	10:44:30.30	-59:37:32.7	16.72	0.72	1.73	...	HAeBe
10443050-5937477	[HSB2012] 2504	10:44:30.50	-59:37:47.7	17.38	0.86	1.54	...	HAeBe
10450445-5937298	CI* Trumpler 14 Y 102	10:45:04.46	-59:37:29.8	13.89	0.56	0.95	...	HAeBe
10450994-5943492	DETC Tr 16 J104510.0-594349	10:45:09.94	-59:43:49.3	16.51	0.91	1.46	...	HAeBe
10452107-5941444	CI Trumpler 16 242	10:45:21.07	-59:41:44.5	12.85	0.47	0.83	B	HAeBe
10452605-5940025	2MASS J10452605-5940025	10:45:26.06	-59:40:02.5	13.52	0.49	0.84	...	HAeBe
10453834-5942078	[S87b] IRS 44	10:45:38.34	-59:42:07.9	13.55	0.6	1.16	...	HAeBe
10454029-5948297	[HSB2012] 4282	10:45:40.30	-59:48:29.7	16.43	1.52	2.38	...	HAeBe

Appendix A: Sky-subtraction procedure

The Gaia-ESO HR15n dataset on Tr 14/16 contains 185 pure-sky spectra from 137 distinct sky positions, taken simultaneously to the stellar spectra. We have identified the following components in these sky spectra:

1. Sky-glow emission lines from Earth atmosphere: nearly identical within spectra from the same Observing Block, variable with time (from an Observing Block to the next), narrow within instrumental resolution, at fixed wavelength in Earth frame.
2. Scattered solar light (typically moonlight): continuum with absorption lines, being essentially a solar spectrum at very low levels. Constant within the same Observing Block, but changing from one Observing Block to the next.
3. Nebular $H\alpha$, He I, [N II] and [S II] lines: they originate from physically large regions near the target stars, and do not vary with time, but have a strong spatial dependence in their strengths, line shapes, widths, and velocities (see Paper I).
4. Nebular continuum emission, from reflection nebosity: a non-negligible component in Tr 14/16, free of solar-like spectral features but with a rather flat spectrum (like massive stars in the nebula), time-constant but space-variable (Paper I).

The standard Gaia-ESO pipeline is able to remove components 1-2 (constant within the same Observing Block, variable in time), but not to deal with components 3-4. Conversely, an attempt to correct a star spectrum using only the sky spectrum nearest on the sky would have more success in dealing with components 3-4, but would perform badly on components 1-2, when these are significant. Clearly, in the complex case of Tr 14/16 a combined approach is needed.

Stellar parameter evaluation relies on the depth of stellar absorption lines/bands, so that an accurately determined stellar continuum is of the greatest importance. Contamination by sky-glow or nebular lines is in this context a minor problem, affecting very localized wavelength regions/lines, which may be usually ignored in deriving star parameters (except for the case of $H\alpha$). We therefore focus first on sky continuum determination and correction.

In the Tr 14/16 dataset we find that the sky continuum does not contain traces of scattered sunlight, using two methods. We computed the cross-correlation function (CCF) of the sky spectra (nebular lines excluded) with a solar spectrum, looking for any peak near $RV=0$, but no such peak was found for any Observing Block. A second method was to fit the sky spectrum with a constant, flat spectrum plus a scaled solar spectrum: again, the scaling factor for the solar spectrum was negligibly small with respect to the other, flat, component, for all Observing Blocks. Instead, within the same Observing Block the median sky continuum level is found to vary significantly, and with a clear spatial pattern, a clear indication of a nebular (reflection) origin for this sky spectrum component.

In Tr 14/16, the absence of scattered solar continuum enables us to eliminate all time-variable sky signatures by just subtracting out the sky-glow lines: this will leave a purely "star plus nebular" spectrum, and the nebular part will be later estimated from the whole set of (non-simultaneous) sky spectra in the same dataset. Sky-glow lines in the HR15n range, of sufficient intensity as to merit consideration in this context, are no more than 20 narrow lines. In principle, also some geocoronal $H\alpha$ emission is expected, but in practice it is not detected against the enormously brighter $H\alpha$ emission from the nebula. For each Observ-

ing Block, the sky-glow line spectrum, net of the adjacent continuum intensity, and averaged within the same Observing Block, was computed, and subtracted out from all spectra in the same Observing Block to obtain "star plus nebular" or "nebular-only" spectra, for stellar and sky spectra respectively.

Having eliminated terrestrial sky features in this way, the problem now reduces to estimate the most appropriate nebular spectrum to be used for correcting a given stellar spectrum. Since the spatial density of sky fibres (considering all Observing Blocks together) is much less than that of target star fibres, the correspondence between the nebular (and sky-continuum) emission in a stellar spectrum and in its nearest-neighbor sky spectrum is never found to be perfect. Distances between a given star and its nearest sky fibre are of order of 30" or more: the nebular morphology is here so complex that there is no guarantee that even the nearest sky is a good approximation to the sought nebular spectrum at the star position; one gets an idea of the range of variation of nebular spectrum in the vicinity of a given star by looking at more (say five) sky positions nearby. Therefore, we made subtraction of nebular spectra from stellar spectra five times per star, using its nearest five sky positions. Since the properties of nebular emission vary sometimes sharply, and definitely non-linearly in space, this is considered a robust method (within the limitations of the available data) to understand the uncertainties involved in the procedure.